"Laser Trapping Microchip for Biotechnological Applications – Design and Development"

By

MSc Eng Bolesław Andrzej Kołodziejczyk

School of Physical Sciences

Dublin City University

Supervised by

Prof Brian D MacCraith

Submitted in partial fulfilment of the requirement for the Degree of Doctor of Physical Sciences

Dublin, July 2005

Declaration

I hereby certify that this material, which I now submit for assessment on the programme of study leading to the award of Doctor of Physical Sciences is entirely my own work and has not been taken from the work of others save and to the extent that such work has been cited and acknowledged within the text of my work.

Signed: ____________________

ID No.: 51185792 Date: 23.01.2006

Abstract

"Laser Trapping Microchip for Biotechnological Applications – Design and Development"
by
Boleslaw Andrzej Kolodziejczyk

This work presents a novel approach towards integrated dual-beam optical trapping achieved using planar lightwave circuit (PLC) technology Three fabrication technologies sol-gel, photolithography and reactive ion etching were combined to fabricate a Laser Trapping Microchip (LTM) allowing one-dimensional manipulation of transparent micrometer-size spherical objects

Detailed steps of the LTM development are described, beginning with a theoretical approach and numerical simulations through the design and synthesis of a suitable photopatternable sol-gel material, culminating in the fabrication process and experimental confirmation of the trapping properties of the device

The proof of concept of this unique device was achieved by demonstrating its optical trapping abilities using micrometer size polystyrene beads with diameters in the range between 4 µm and 10 µm and the refractive index of 1 59

The LTM device possesses many advantages over currently existing dual-beam laser trapping systems such as small overall dimensions (~15 x 30 x 0 5 mm), low power optical power consumption (<15mW), improved stability of the optical trap due to precise alignment of the optical paths and a relatively easy fabrication process For these reasons there are many potential applications of the LTM device in biotechnology, microfluidics and other sciences making it an attractive device for commercial use

Table of Contents

1. Introduction **6**

2. Physical Principles of Optical Trapping **8**

2.1. Introduction 8

2.2. Dual-Beam Trapping Model Presentation 10

2.3. Conclusion 20

3. Numerical Calculations and Simulations **21**

3.1. Introduction 21

3.2. Numerical Calculations of Trapping Efficiency 26

3.3. Refractive Index Step Calculation for Single Mode Waveguides 32

3.4. Light Propagation Simulation 36

3.5. Conclusion 40

4. Properties of the Materials Used **42**

4.1. Introduction 42

4.2. Sol-gel Materials 45

4.3. Conclusion 51

5. Fabrication Process **52**

5.1. Introduction 52

5.2. Process Steps 55

5.3. Conclusion 61

6. Mask Design **62**

6.1. Introduction 62

6.2. Mask Details 63

6.3. Conclusion 65

7. Photolithography Process Optimisation **66**

7.1. Introduction 66

7.2. Light intensity Distribution 69

7.3. Exposure Dose Uniformity 70

7.4. Illumination Optics 70

7.5. Separation Distance Between the Mask and Material 71

7.6. Sample Baking Time and Temperature Before Exposure 71

7.7. Conclusion 74

8. Trap Housing Fabrication (Reactive Ion Etching) **75**

8 1 Introduction 75
8 2 Reactive Ion Etching Process Optimisation 83
8 2 1 Samples Preparation 83
8 2 2 Sample Characterisation 84
8 2 3 Influence of O_2 flow on etching properties 87
8 2 4 Influence of Argon Flow 89
8 2 5 Influence of SF_6 Flow 91
8 2 6 Influence of RF Power 92
8 2 7 RIE Process Parameters Selection 94
8 3 Conclusion 96
9. Estimation of the LTM Trapping Forces 97
9 1 Introduction 97
9 2 Optical Beam Intensity Profile 98
9 3 Optical Losses Measurement 99
9 4 Result of Force Calculations 103
9 5 Conclusion 108
10. Laser Trapping Observation 109
10 1 Introduction (Experimental Setup) 109
10 2 Testing Procedure 110
11. Conclusions and Suggestions for Further Work 114
12. References 117
13. Appendix 130

1. Introduction

The overall objective of the project was to build a new generation of dual-beam optical trapping microchip system for biotechnological and medical applications. Specific applications include: intercellular microsurgery, micro-organism and biopolymer manipulation, observation of mobility patterns of human spermatozoa, and the control of other objects etc [1-12]. The major contribution of this work towards miniaturisation of the laser trapping device is based on a unique concept that incorporates dual-beam optical trapping, sol-gel, UV-photopatterning and plasma technologies into a small microchip that is capable of trapping *micrometer* size objects such as polystyrene beads.

Parallel research on the development of sol-gel materials and sol-gel plasma etching created an opportunity to build a laser-trapping system, which possess several advantages over previously available optical tweezers and dual-beam trap solutions [13-16]. In comparison to optical tweezers, the proposed device does not require high numerical aperture objective lenses and it produces a stable optical trap with low power laser diodes. This allows direct well-focused observation of objects through an external microscope. Another feature is the exceptionally small size of the device so that it can fit as a bench top unit in a standard biotechnology laboratory. The early versions of dual-beam traps overcame the weaknesses of optical tweezers, but demanded complex positioning elements or devices allowing counter propagating light beams to propagate exactly along the same optical axis [3,17,18]. Since this is crucial for producing an efficient trapping equilibrium the dual-beam optical trap was considered as a suitable system to be simplified and miniaturised using planar lightwave circuits (PLC).

After examining several possibilities the most suitable techniques selected for accurate placing of optical elements on PLC devices are either laser writing or photolithography combined with plasma etching, both utilising sol-gel technology. The technologies mentioned above present comparable capabilities in terms of accuracy and repeatability of the optical structures. Photolithography is more suitable for mass production and has the potential for future commercial applications. On the other hand, laser writing is more flexible and requires fewer resources to produce single

units of the microchip. Nevertheless considering the industrial orientation of the microchip, its further development and possible future increased complexity, photolithography was chosen as the technology that best met the requirements of the proposed system. A PLC-based system also has disadvantages; for example when the system configuration changes or different trapping object sizes are used completely new and relatively expensive photo masks must be produced. This increases costs and manufacturing time. However, once a well-designed and properly set up system is introduced, millions of similar good quality devices can be produced within a short period of time. Effortless access using surgical scalpels and micro devices for manipulation of trapped objects was also considered while deciding on the method to be applied.

In summary, the primary objective of the work reported here was to combine two highly advanced technologies, photolithography and plasma etching, in order to create a unique device (Figure 1-1) capable of trapping micrometer size objects with a low laser power.

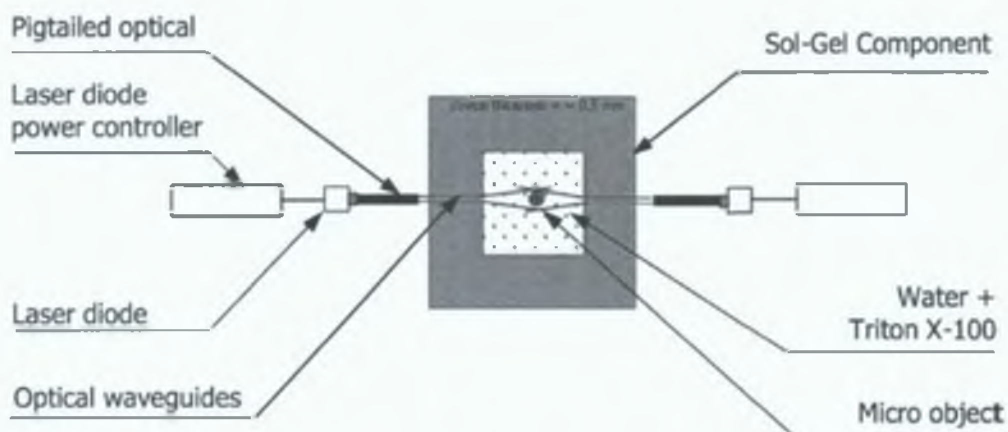

Figure 1-1. Laser Trapping Microchip system – example configuration

Other objectives included development of a suitable photopatternable sol-gel material and optimisation of technologies used for the device fabrication. It was also proposed to characterise this device and evaluate it against the performance criteria of existing devices. The upcoming chapters present a physical description of the optical trapping phenomena, numerical simulations, design and synthesis of a suitable photopatternable sol-gel material, culminating in the fabrication process and experimental confirmation of the trapping properties of the device.

2. Physical Principles of Optical Trapping

2.1. Introduction

The theoretical study of laser trapping has been conducted extensively for over twenty years and plays an important role in the numerical estimation of optical forces acting on a trapped object It also aids in understanding different types of laser trapping alignment configurations

In 1970, Ashkin and Dziedzic demonstrated for the first time that a spherical particle can be held in stable equilibrium by strongly focused laser beams [14] The combined force of photons reflecting and refracting from the boundary of a microsphere surrounded by a transparent medium was able to compensate for the influence of gravitational forces, dragging forces, and Brownian motion, and to provide full control over the trapped object Since then, scientific interest in the technique has grown, resulting in numerous publications developing both theoretical approximations and instruments for practical applications

The first report on a dual-beam trap was presented in 1985, opening a new field of investigation and extending the variety of potential applications and system configurations [14-21] Three different trapping configurations have been recognised with respect to their application and configuration These have been categorised by the particular types of forces acting on the trapped object

The first and the most basic type of laser-trapping systems is called the **levitation trap** [2] Optical lenses are placed under the bottom of a transparent sample and propagating light exerts a substantial scattering force acting against gravity on the object, which causes its displacement in the direction of light propagation

Optical tweezers are the most common optical traps encountered in the literature and are widely used for demonstrating laser-trapping phenomena [22-29] Objective lenses with high numerical aperture are placed over or under the sample focusing the light into a small spot (Figure 2-1 a, b) A microsphere positioned in the vicinity of the spot is subjected to the forces raising the microsphere from the bottom of the particle's

housing The optical force distribution enables three dimensional object manipulations, which gives a high degree of flexibility to the system Scattering forces are negligibly small thus gradient forces play the most important role in providing a stable equilibrium point

In contrast with single-beam optical traps, **dual-beam optical traps** are created by two laser beams emerging from two coaxially aligned optical paths (Figure 2-1 c) [13-16,19,20,30] They induce forces similar to those produced by levitation traps but in this case both gradient and scattering forces are doubled and both of them can be used simultaneously to manipulate the trapped object

Dual-beam optical traps offer more advantages than the two trapping techniques previously described One of them is the ability to move an object by changing the optical power of one of the beams The difference in power supplied, influences the force balance and causes the particle to move towards one of the beams until the equilibrium point is reached This process removes the need for additional mechanical elements in the system, thus making it less complicated

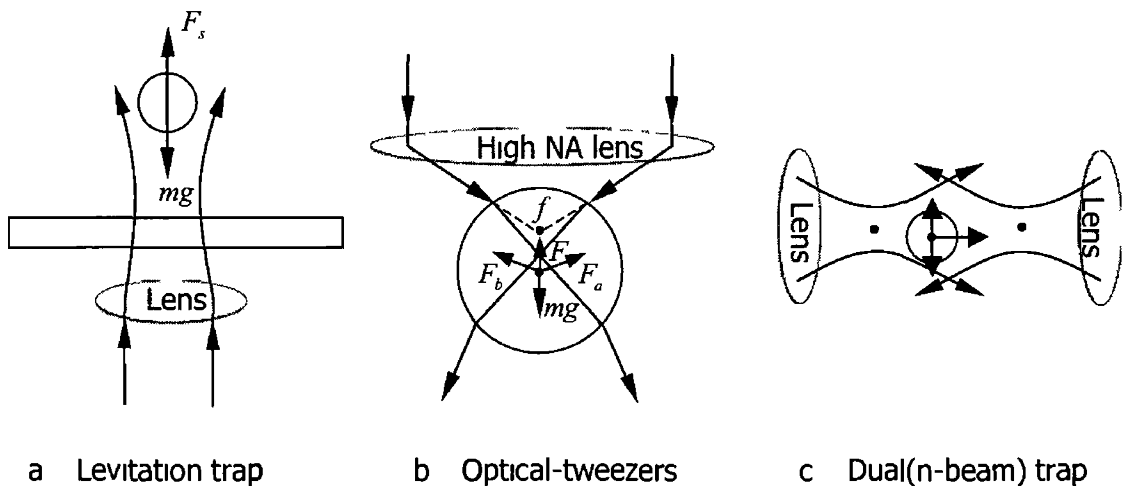

a Levitation trap b Optical-tweezers c Dual(n-beam) trap

Figure 2-1 Laser trapping systems configurations

Moreover, relatively lower laser intensity can be used for holding an object in a stable position avoiding damaging effects on a living object and therefore allowing it to be held for longer in the trap

Another advantage of dual-beam traps is that the operational design enables relatively easy access for object observation and external manipulation, which gives more flexibility for a series of biotechnological applications

With respect to potential future applications the dual-beam trap is the most suitable for biotechnological applications and therefore it was selected for the system to be developed here

Two theoretical approaches may be used to describe laser-trapping phenomena The first uses the Rayleigh theory model, which applies to particles satisfying the condition

$$2\pi r_0 / \lambda_0 \quad 1 \qquad \textit{Equation 2-1}$$

where

r_0 - radius of the microsphere,

λ_0 - laser light wavelength,

This theory has been compared to experimental data in K F Ren [31] and Y Harada [32] The second theoretical approach applies ray optics for particles confined in the Mie regime ($2\pi r_0 / \lambda_0$ '' 1) or at least the intermediate regime ($2r_0$ | λ_0) Although the ray optics model has some disadvantages, such as reduced accuracy, it is relatively easier to calculate and can be used for systems designed for trapping objects much bigger than the wavelength of light used [1,33-38]

2.2. Dual-Beam Trapping Model Presentation

In the laser trapping microchip device the chosen trapped objects were intended to be confined in the Mie regime So, when describing the phenomena, the ray optics approximation was chosen In this case, when a small ray of light acts on a dielectric (transparent) surface it becomes partially reflected and refracted according to Snell's law causing a change in momentum of the photons, which is transferred to the microsphere The change in momentum is then responsible for the forces acting on the microsphere in certain directions These forces can be decomposed into two perpendicular components called scattering (which arises by reflection on particles and

is proportional to the optical intensity) and the gradient force component (which arises by refraction on the particle due to the optical intensity gradient) (Figure 2-2)

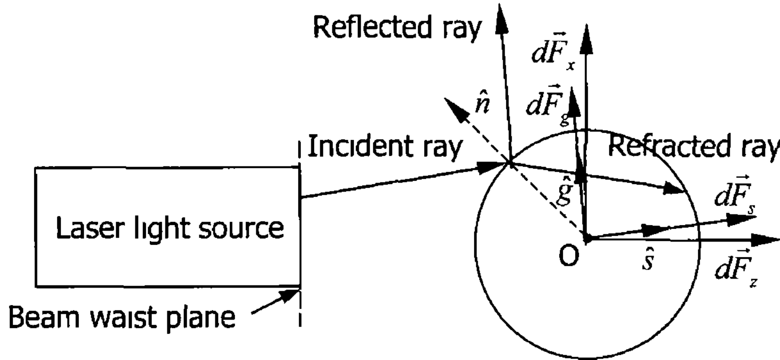

Figure 2-2 Trapping forces acting on a spherical object

Following Sidick and Collins [1] the forces can be described by two separate vector equations

$$d\vec{F}_s \quad \hat{s}\frac{n_1}{c}q_s dP$$ *Equation 2-2*

$$d\vec{F}_g \quad \hat{g}\frac{n_1}{c}q_g dP$$ *Equation 2-3*

where

$\hat{s}$, $\hat{g}$	unit vectors in directions of $\vec{F}_s$ and $\vec{F}_g$ respectively ($\vec{F}_s$ is parallel to the direction of the incident ray and $\vec{F}_g$ is perpendicular to $\vec{F}_s$)
n_1	refractive index of the medium surrounding the microsphere
c	free-space light speed
dP	differential power of the ray

q_g and q_s represent a fraction of momentum transferred to the microsphere in respective directions They are given by the formulae [1,14,15,19,32]

$$q_s \quad 1 \quad R\cos 2\alpha_i \quad T^2 \frac{\cos(2\alpha_i \quad 2\alpha_r) \quad R\cos 2\alpha_i}{1 \quad R^2 \quad 2R\cos 2\alpha_r}$$ *Equation 2-4*

$$q_g \quad R\sin 2\alpha_i \quad T^2 \frac{\sin(2\alpha_i \quad 2\alpha_r) \quad R\sin 2\alpha_i}{1 \quad R^2 \quad 2R\cos 2\alpha_r}$$ *Equation 2-5*

where

α_i angle of incidence on the surface

α_r angle of refraction on the surface

T and R represent reflectance and transmittance of light on the boundaries between two media with different refractive indices given by Equations 2-8 to 2-11, which also take into account the polarisation properties of the laser light [13,39]:

$$T_{TE} \quad 1 \quad \left|\frac{n_1 Cos(\alpha_i) \quad n_2 Cos(\alpha_r)}{n_1 Cos(\alpha_i) \quad n_2 Cos(\alpha_r)}\right|^2$$ *Equation 2-6*

$$R_{TE} \quad \left|\frac{n_1 Cos(\alpha_i) \quad n_2 Cos(\alpha_r)}{n_1 Cos(\alpha_i) \quad n_2 Cos(\alpha_r)}\right|^2$$ *Equation 2-7*

$$T_{TM} \quad 1 \quad \left|\frac{n_2 Cos(\alpha_i) \quad n_1 Cos(\alpha_r)}{n_2 Cos(\alpha_i) \quad n_1 Cos(\alpha_r)}\right|^2$$ *Equation 2-8*

$$R_{TM} \quad \left|\frac{n_2 Cos(\alpha_i) \quad n_1 Cos(\alpha_r)}{n_2 Cos(\alpha_i) \quad n_1 Cos(\alpha_r)}\right|^2$$ *Equation 2-9*

in which n_2 represents the refractive index of the refractive medium (in our case the microsphere).

Numerical calculations of R and T for TE and TM polarisation of the dual-beam optical trap forces obtained so far [1,15] reveal that linearly and circularly polarised beams produce the same amount of transverse and axial force when the microsphere is in the close vicinity of equilibrium. However, when we move the microsphere from the point of stability by a distance perpendicular to the optical axis, the transverse and axial components are not identical anymore for different states of light polarisation. It was calculated that the light polarised in the direction of the displacement brings a marginal (7%) rise in the value of the transverse forces.

From a technical point of view it is possible to incorporate extra passive optical elements into the system to at least theoretically obtain better microsphere confinement in the transverse force direction. However beam polarisation always

involves power losses, which, assuming equal values of polarisation components, would be about 50% Obviously this loss of power could not be compensated by the polarisation effect and, in fact, forces acting directly on the microsphere would be lower than that in the original configuration On the other hand, the primary goal here was to build a system containing a minimum number of separate elements The addition of polarizers would require additional effort and would make the system more complicated, which is highly undesirable in any innovative design Despite these drawbacks, polarisation effects on laser trapping forces present some opportunities for LTM systems and these may be utilised in future LTM developments One of these opportunities could be, for example, the incorporation of polarisation elements directly into the microchip structure in order to establish control over the rotational movement of trapped birefringent objects

Once it had been decided to use a circularly polarized laser beam, R and T are given by the arithmetic average of TM and TE components

$$R \quad \frac{R_{TE} \quad R_{TM}}{2} \qquad \text{Equation 2-10}$$

$$T \quad \frac{T_{TE} \quad T_{TM}}{2} \qquad \text{Equation 2-11}$$

Since gradient forces are strictly dependent on intensity gradient changes then the use of multimode light causes the occurrence of more than one stable equilibrium point and hence does not match the system specification Similarly, different mode profiles other than the Gaussian profile of a single mode beam were not considered to avoid adding complexity to the system design

Therefore, for all further investigation of laser trapping calculations, it is assumed that the laser beam acting on a microsphere surface is of Gaussian shape, which means that the differential power incident on the small region of the microsphere, is given by [1]

$$dP \quad I\cos\theta dS \quad \frac{2P_0}{\pi w_0^2}\exp(\; 2r^2/w^2)\cos\theta dS \qquad \text{Equation 2-12}$$

where

P_0 – total power of the laser beam

w_0 – laser beam waist (Figure 2-3)

r – distance from the beam axis to element dS of the surface

w – beam radius at the point for which a Gaussian laser beam is defined as [39]

$$w = w_0 \sqrt{1 + \left(\frac{z_p \lambda_0}{\pi n_1 w_0^2} \right)^2} \qquad \textit{Equation 2-13}$$

θ angle between the normal of the differential area dS and beam axis (Figure 2-4)

dS differential element of irradiated surface

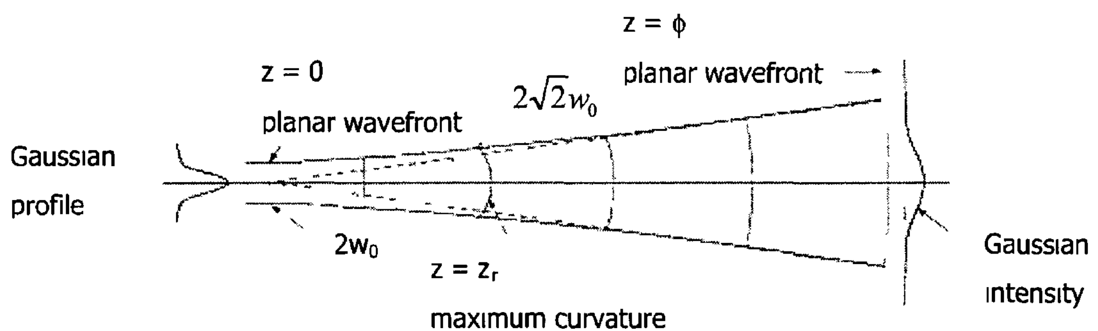

Figure 2-3 Laser beam with Gaussian intensity profile

When examining the forces generated by the laser beam striking the microsphere in the vicinity of stable equilibrium, the microsphere and laser beam must be displaced with respect to each other in order to observe the change in the forces

The most useful method for future calculations is to create a rectangular coordinate system and place its origin (axis x, y, z) in the plane of the beam waist with axis z passing through the centre of the microsphere, assuming a displacement of the laser beam axis, $\overline{CA}$, from the z-axis by a distance d (Figure 2-4)

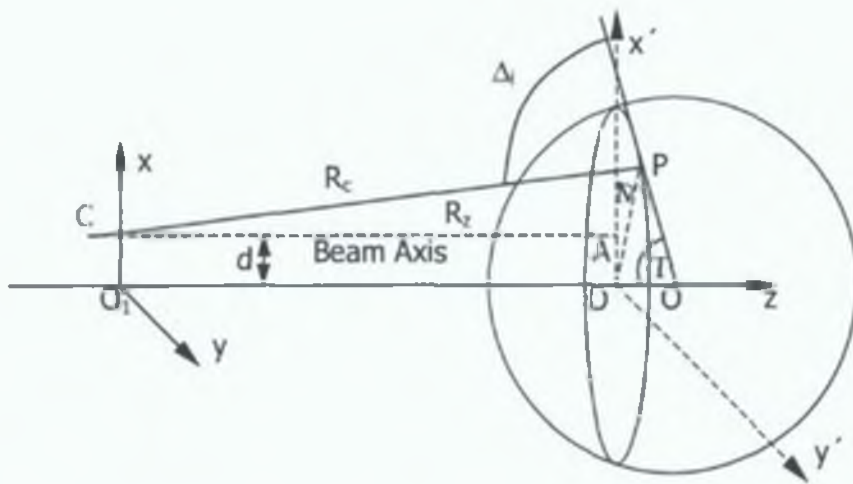

Figure 2-4. Ray optics coordination system

The laser beam is meant to have a positive propagation direction which means that it propagates from left to right towards the microsphere. Then, the curvature R_c of a single ray $\overline{CP}$, which appears to come from the point C behind the plane of the beam waist, is given by [39]:

$$R_c = z_p \left[1 + \left(\frac{\pi n_1 w_0^2}{z_p \lambda_0} \right)^2 \right]$$ *Equation 2-14*

where

z_p z coordinate of point P

w_0 laser beam waist

It seems from Equation 2-14 that the value of R_c can be either positive or negative depending on the value of z_p corresponding to a situation when the microsphere is centred to the right ($R_c > 0$) or to the left ($R_c < 0$) of the beam waist.

In the proposed system, the laser light is confined by the waveguides so beam waists are placed at the waveguides endfaces. Therefore the microsphere cannot be physically moved behind the beam waists and the case $R_c < 0$ is irrelevant for further theoretical investigation. The coordinate z_p of the point P on the boundary can be defined in spherical coordinates with respect to the centre of the microsphere by

$$z_p \quad z_0 \quad r_0 Cos\,\theta$$ *Equation 2-15*

where

z_0 $\quad z$ coordinate of microsphere centre

Following the geometry presented in Figure 2-4 and Figure 2-5 the unit vectors $\hat{s}$ and $\hat{g}$ can be described as [1]

$$\hat{s} \quad \frac{\hat{x}(r_0 \sin\theta\cos\varphi \quad d) \quad \hat{y}(r_0 \sin\theta \sin\varphi) \quad \hat{z}R_z}{|R_c|}$$ *Equation 2-16*

$$\hat{g} \quad \frac{\hat{x}\left(r_0 \sin\theta \sin\varphi \quad d \quad \frac{dR_c}{a\cos\gamma}\right) \quad \hat{y}(r_0 \sin\theta \sin\varphi)}{R_c \tan\gamma}$$ *Equation 2-17*

$$\frac{\hat{z}\left(R_z \quad \frac{R_c(R_z \quad r_0\cos\theta)}{a\cos\gamma}\right)}{R_c \tan\gamma}$$

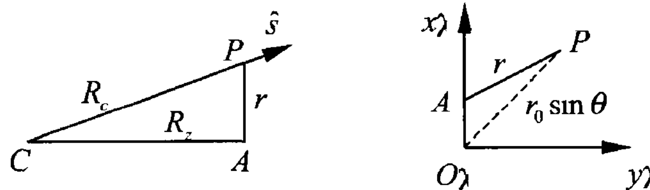

Figure 2-5 Geometrical relationships between various variables

The geometry in the plane of incident light is presented in Figure 2-5 with the projection of vector $\overline{CP}$ on z-axis R_z given by the equation of the right-angled triangle

$$R_z \quad \sqrt{R_c \quad r^2}$$ *Equation 2-18*

Other parameters used in all of the above equations are defined as follows [1]

- Angle of incidence

$$\alpha_i \quad ArcCos[\frac{d^2 \quad (Rz \quad r_0 Cos\,\theta)^2 \quad r_0^2 \quad R_c^2}{2r_0R_c}] \qquad \text{Equation 2-19}$$

and according to Snells law, which describes the relationship between the angles of incidence and refraction and the indices of refraction of the two medium α_r is given for small angles by

$$\alpha_r \quad \frac{n_1}{n_2}\alpha_i \qquad \text{Equation 2-20}$$

- Half-apex angle γ presented in Figure 2-6 and used in the equation can be defined as [1]

$$\gamma \quad ArcCos\left(\frac{R_c^2 \quad a^2 \quad r_0^2}{2aR_c}\right) \qquad \text{Equation 2-21}$$

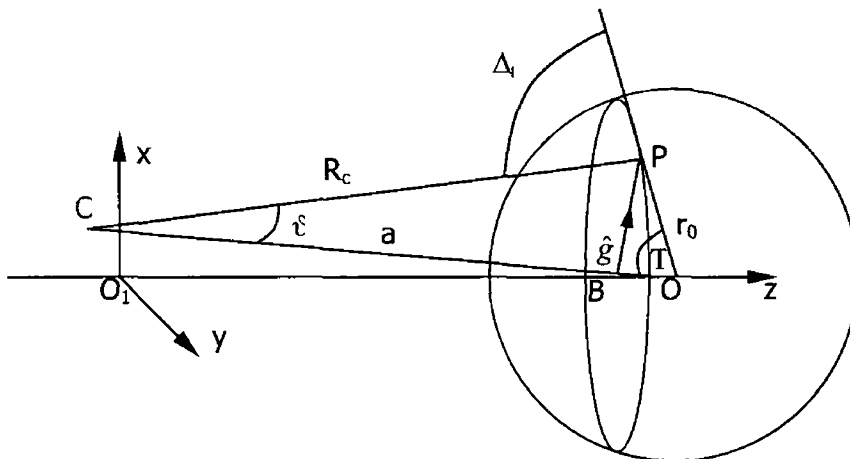

Figure 2-6 Half-apex angle geometry

Geometrical relations and the symmetry of the problem (causing cancellation of dF_y force components) leads to the equation for the total force produced by the laser beam

$$\vec{F} \quad \frac{n_1 P_0}{c}\frac{4r_0^2}{\pi}\int_0^{\pi} d\varphi \int_0^{\theta_{max}} d\theta \sin\theta \,\upsilon \cos\theta \left(\hat{s} q_s \quad \hat{g} q_g\right)\frac{\exp\left(\ 2r^2/w^2\right)}{w^2} \qquad \textit{Equation 2-22}$$

The symmetry for both of the force components in plane $x \rangle y \rangle$ allows the second integral to be carried out from 0 to π instead of from 0 to 2π with respect to angle φ (Figure 2-4) This however implies that both F_z and F_x must be multiplied by a factor of 2

The upper limit of the first integral θ_{max} is found for each value of φ by finding the root of the Equation 2-23 with respect to θ substituting $\theta \quad \theta_{max}$ [1]

$$d^2 \quad (R_z \quad r_0 \cos\theta)^2 \quad r_0^2 \quad R_c^2 \quad 0 \qquad \textit{Equation 2-23}$$

By putting Equations 2-16 and 2-17 into Equation 2-22 and decomposing it into F_x and F_y scalar components, we can then write a more simplified form

$$F_z \quad \frac{n_1 P_0}{c} Q_z \qquad \textit{Equation 2-24}$$

$$F_x \quad \frac{n_1 P_0}{c} Q_x \qquad \textit{Equation 2-25}$$

where Q_z and Q_x are called the trapping efficiencies defined respectively as follows [1]

$$Q_z \quad \frac{2r_0^2}{\pi}\int_0^{\pi} d\varphi \int_0^{\theta_{max}} d\theta \sin 2\theta \frac{\exp\left(\ 2r^2/w^2\right)}{w^2 R_c}\upsilon \qquad \textit{Equation 2-26}$$

$$\upsilon \quad q_s R_z \quad \frac{q_g}{\tan\gamma} R_z \quad \frac{R_c(R_z \quad r_0 \cos\theta)}{a\cos\gamma}$$

$$Q_x \quad \frac{2r_0^2}{\pi} \int_0^{\pi} d\varphi \int_0^{\theta_{max}} d\theta \sin 2\theta \frac{\exp\left(\; 2r^2 / w^2 \right)}{w^2 R_c} \upsilon$$

$$\upsilon \; q_s \left(r_0 \sin\theta \cos\varphi \quad d\right) \quad \frac{q_g}{\tan\gamma} \upsilon \; r_0 \sin\theta \cos\varphi \quad d \quad \frac{R_c}{a \cos\gamma}$$

Equation 2-27

In the case of a dual beam trap the total forces acting on the microsphere are the superposition of the forces exerting on a microsphere by a single laser light source The configuration of the dual beam trap is presented in Figure 2-7, where s is the distance between the waists of the counter propagating beams and z_0 represents a distance between the centre of the X, Y, Z coordination system and the center of the microsphere

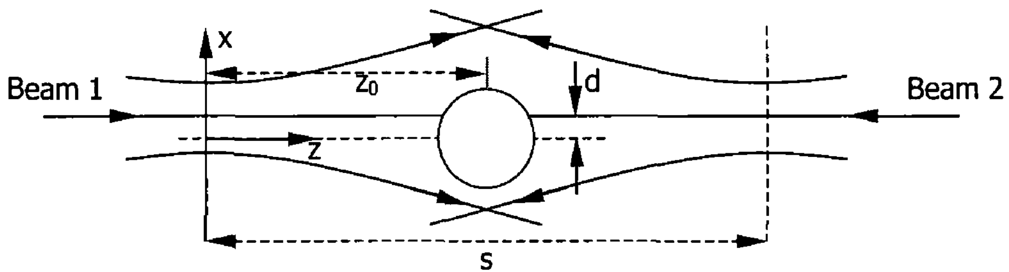

Figure 2-7 Dual beam trapping configuration

Since the two counter propagating beams induce axial (scattering) forces in opposite directions the total force produced can be represented by

$$F_{zt} \quad F_{z1} \quad F_{z2} \quad \frac{n_1}{c}\left(P_1 Q_{z1} \quad P_2 Q_{z2}\right)$$

Equation 2-28

From the other side, the gradient forces acting on the microsphere depend on the intensity distribution and, since both beams have a positive contribution to the intensity gradient, the total force is a sum of the forces produced by each of the beams separately and it is given by

$$F_{xt} \quad F_{x1} \quad F_{x2} \quad \frac{n_1}{c}\left(P_1 Q_{x1} \quad P_2 Q_{x2}\right)$$

Equation 2-29

Since the coordinate system of both beams was measured from the beam waist of the first beam then the second beam coordinate z_0 must be replaced by $s \quad z_0$ as shown in Figure 2-6 Thus an increase in the value of z_0 of the first beam results in a decrease of the second beam z_0 and causes a change in the forces balance

2.3. Conclusion

The presented theoretical background of optical trapping based on ray optics theory is a sufficient approximation for trapping objects of a few micrometers in diameter The set of derived equations also explicitly assumes a spherical shape of the object In practical applications of the optical trapping system this will not always be the case as the living matter can posses various different shapes In these cases the calculations of the trapping forces could present a much bigger challenge both from a geometrical and an analytical point of view especially in terms of solving the integrals of the equations [40,41]

There is also an interesting phenomenon that is not immediately visible from these geometrical relations and which is often used in practical applications Based on the intuitive approach one can conclude that the trapped object is squeezed by the optical forces acting in opposite directions However, more careful study of the geometrical relations reveals that in fact the trapped object is subjected to stretching forces and if the object is a living cell this could cause its extrusion or even permanent damage [17,18,42] This fact can be very useful for measuring the flexibility of the object and its physical endurance, and is an example of another laser trapping microchip application

In summary the physical approximations described in this chapter form a solid base for the numerical calculation of the forces ultimately expected in the LTM device

3. Numerical Calculations and Simulations

3.1. Introduction

The theoretical model presented in Chapter 2 forms a solid background for the numerical evaluation and optimisation of laser trapping forces required to build a workable device.

The first step towards the calculation of optical forces was to find the trapping efficiencies for the specific trapping conditions. These conditions involve combinations of multiple variables, which are the components of Equation 2-25 and Equation 2-26 (w_0 , λ_0 , r_0 , d , z_0). Optimisation consisted of the selection of the combination of variables, which provided the highest transfer of the photon momentum to the trapping forces.

The large number of parameters involved in laser trapping efficiency calculations would imply a huge number of calculations to be conducted. In order to limit the number of iterations to an acceptable level, only a few parameters were varied while others were kept constant as their values were based upon the practical application of the device.

Based upon the anticipated applications of the Laser Trapping Microchip, the trapping parameters that were set as constants were done so for the following reasons:

- Refractive index of surrounding medium (n_1)

  In many biological, biotechnological and laser trapping applications [5,6,7,43], living objects are immersed in solutions mainly consisting of water, which creates a natural environment for living organisms. In our experiment a surfactant, Triton X-100 [19], was used to avoid the sticking of particles to the boundaries of the chamber. The surfactant Triton X-100 was mixed with the particles immersed in water in the ratio 50:1 to produce a final particle solution. Since the refractive index of Triton X-100 is close in value to the refractive index of water [44] and its concentration in solution was small it was considered to have marginal influence on the refractive index of the solution and thus final results obtained from calculations.

For these reasons, the value of n_1 in all the numerical calculations was taken to be that of the refractive index of water, 1 333

- Refractive index of the trapped object (n_2)

As seen from Snells equation (Equation 2-20) the n_2 value works in the opposite direction to n_1 which means the higher n_2 the higher the force generated by the trap

In order to provide the best comparison to the previously reported experiments on optical trapping [1,13,26,30,45-48], polystyrene microspheres were used as typical testing objects for the optical trapping devices Available polystyrene microspheres produced by Microsphere Polysciences Inc were characterised with a refractive index of n_2 =1 59 and this value was used in further numerical calculations as a constant

In real applications one should be aware of the fact that the refractive index of the object could be lower than the refractive index of polystyrene Typical living objects contain a high amount of water causing their refractive index value to differ only slightly from the refractive index of pure water (a typical surrounding medium), in which case the trapping forces are greatly reduced [7,43]

- Laser light wavelength (λ_0)

The operational laser light wavelength used during all experiments was 662 nm in the visible range and this value was used in all numerical calculations

The primary consideration in the selection of the laser light wavelength was its visibility This was due to the fact that only light from the visible spectrum range could provide a way to achieve good coupling by the accurate visual alignment between the pigtailed fibre and the waveguide Once the device is pigtailed and the coupling of the light is no longer a problem, then the laser light wavelength can be tailored to the particular application

Another factor, which had an influence on choosing this wavelength, was its interaction properties with bioorganisms. Since experiments started with bioorganisms using the laser trapping method, scientists have been looking for a way to reduce the damaging effect of laser light on the molecular structures of those organisms [49-54]. Svoboda and Block [49] recommend that a laser wavelength in the near infrared region was suitable as it has a reduced influence on the trapped objects molecular structures (Figure 3-1).

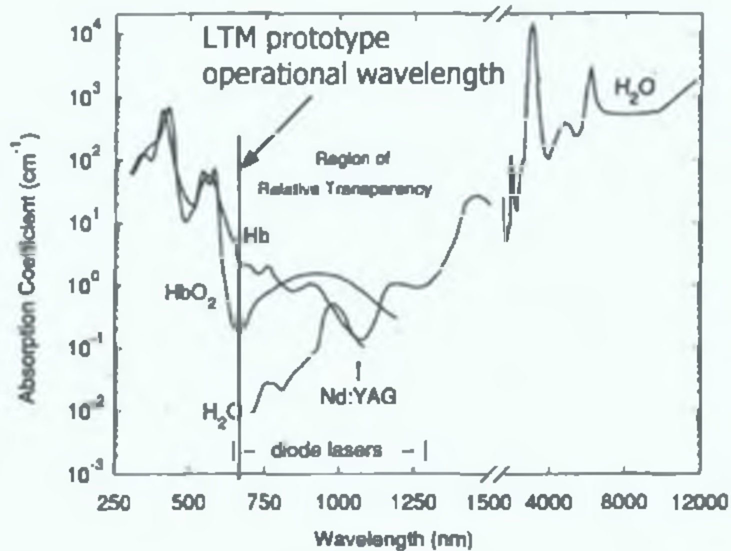

Figure 3-1. Absorption spectra of biological material in the near infrared region, showing absorption of water, deoxyhemoglobin (Hb) and oxyhemoglobin (HbO_2)

At the beginning of the calculations it was assumed that we should manipulate only with the values of those variables, which are relatively easy to adjust and control. It means that the beam waist diameter, polystyrene bead sizes, and the endfaces separation distance were our primary choices.

Parameters which were changed and their influence was a subject of this analysis were:

- Beam waist radius (w_0)

In the presented theoretical model the waveguide size corresponds to twice the beam waist radius. The beam waist variations covered the range between 2 pm to 10 µm. The minimum range was set by fabrication process limitations, which

affected the quality of the waveguides In our process the ridge waveguide shapes deteriorated rapidly below the width of 4 µm The upper limit was based on the ability to produce a large waveguide having a single mode guiding profile Bigger waveguides would require a smaller difference in refractive index between core and the cladding of the waveguide

- Particles (trapped objects) radius (r_0)

In order to be useful for most of the biological applications the device should work with various sizes of living objects The radius of these falls in the range between 2 µm and 5 µm Taking this into account a model was set up to find stable conditions common for different particle sizes Specific calculations were done for available polystyrene beads, which were of three different radii 1 4185 µm, 2 916 µm, and 4 57 µm

For the purpose of homogenous presentation, most of the computational parameters (Figure 3-2) were normalised according to the beam waist size w_0 These parameters include

- Normalised beam waist separation

  $S \quad s/w_0$ *Equation 3-1*

- Transverse offset

  $D \quad d/w_0$ *Equation 3-2*

- Normalised beam waist distance from shifted axial offset

  $Z_0' \quad Z_0 \quad S/2 \quad z_0/w_0 \quad S/2$ *Equation 3-3*

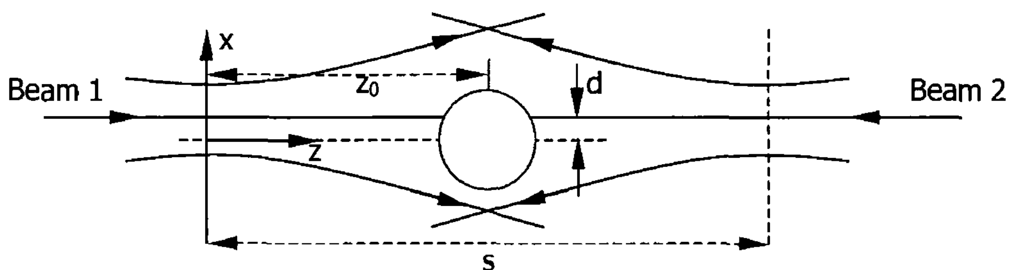

Figure 3-2 Computational parameters of dual-beam trap

This section also contains the calculation of the refractive index difference that should exist between core and the cladding of the waveguides inside the chip to provide single mode guiding This is crucial for a single trapping equilibrium to exist

Finally the impact of the quality of the waveguide endfaces was evaluated by estimating the displacement of the beam centre when the waveguide endface is not perpendicular to the waveguide optical axis The results provided further guidance towards the selection of the fabrication method for the particle chamber

3.2. Numerical Calculations of Trapping Efficiency

For optimisation and numerical evaluation of the trapping efficiency values presented in Chapter 2 (Equation 2-26 and 2-27), the Wolfram Mathematica 4.1. software package was used. Results were achieved separately for both transverse trapping efficiency (Q_{xt}) and axial trapping efficiency (Q_{zt}), which are the components of scattering and gradient trapping forces respectively. Two examples, for beam waist size 2 μm and particle radius 2.916 μm are presented below (Figure 3-3).

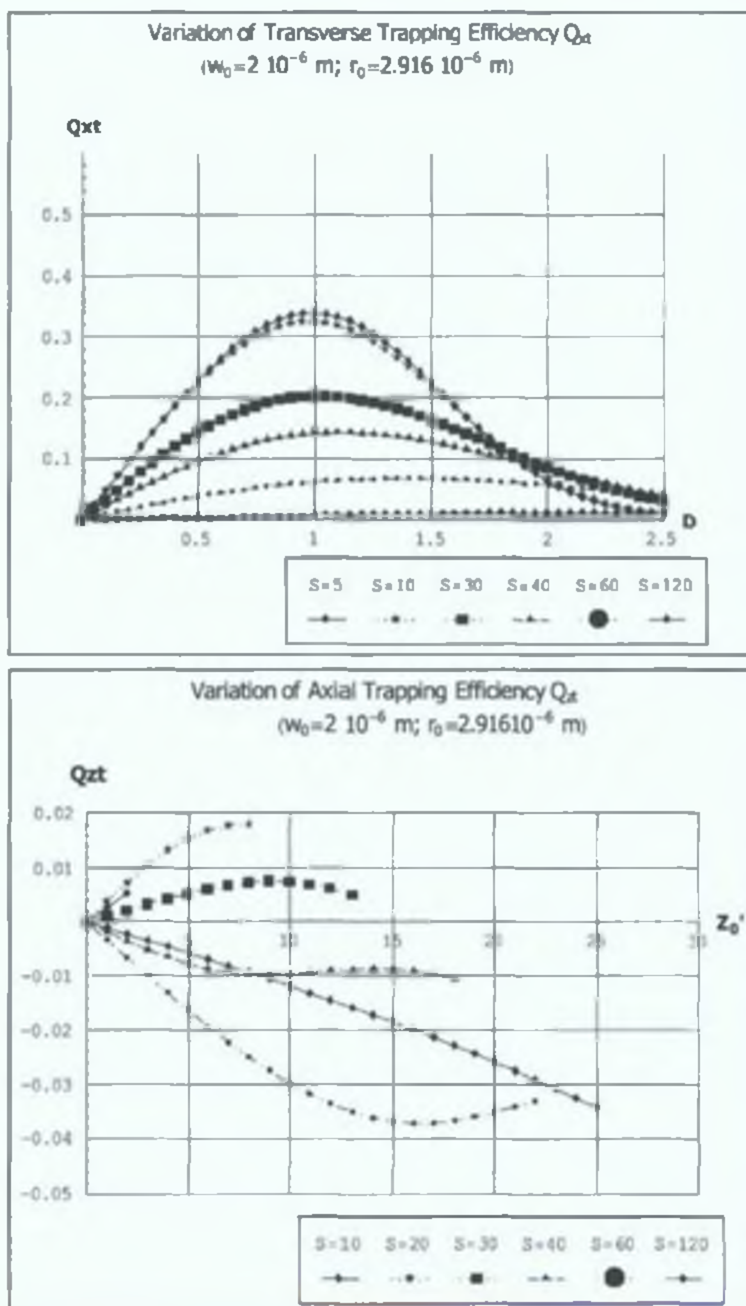

Figure 3-3. Variation of transverse and axial trapping efficiencies vs. microsphere displacement for different separation distance of waveguide endfaces

All the graphs are plotted versus normalised dimensions with respect to the beam waist diameter The transverse efficiency reaches a maximum of 0 75 for the biggest particles in question (4 75 µm) and beam waist size 1 µm The maximum efficiency in axial direction for all considered cases can be observed for 1 µm beam waists separated by 60 µm and a microsphere radius 1 4185 µm From the graphs (Figure 3-5) one can see that the transverse trapping efficiency Q_{xt} decreases with the distance between beam waists and the bigger the diameter of microsphere the higher the maximum value of Q_{xt}

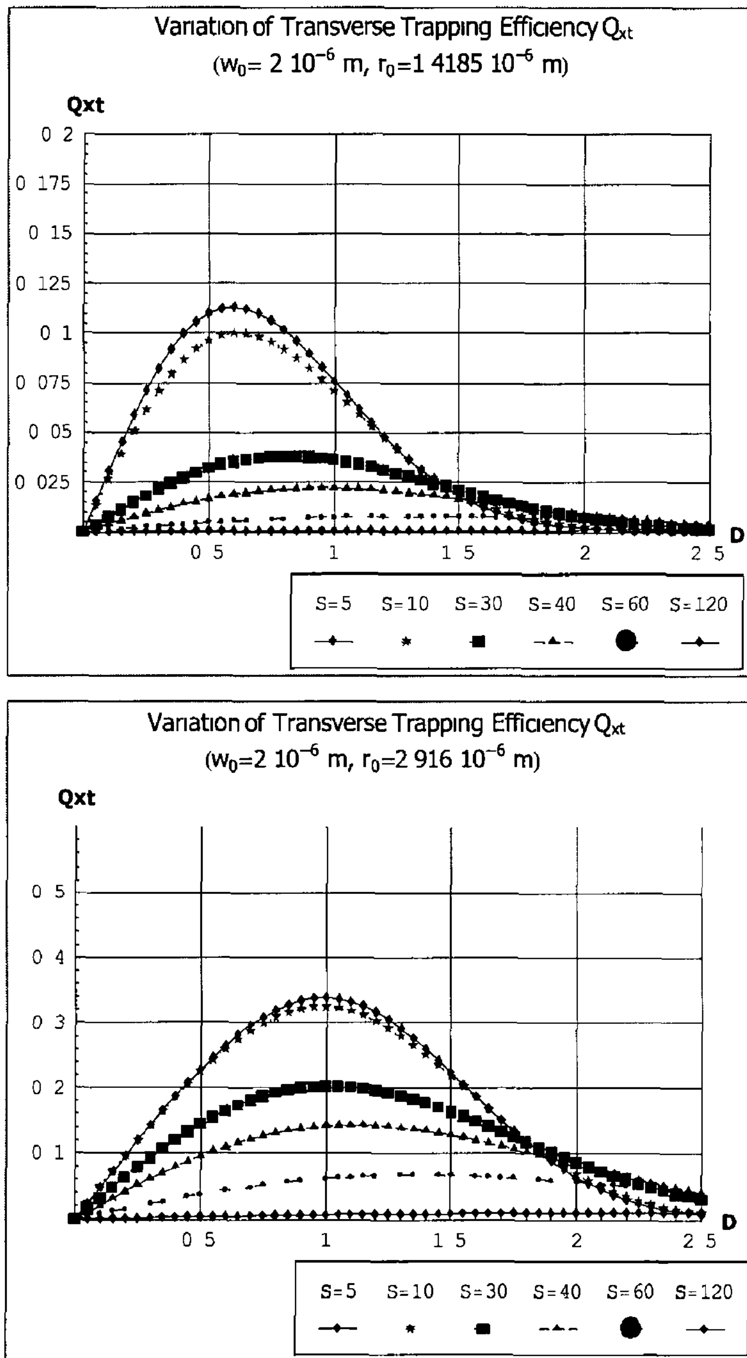

Figure 3-4 Variation of transverse and axial trapping efficiencies for different sizes of the microspheres

In the case of Q_{xt} however the trapping efficiency behaves in the opposite way and decreases with S. As S reaches certain limits and the Q_{xt} slope becomes positive the trapping equilibrium point becomes unstable. This leads to the particle being trapped against the endface of one of the waveguides [1]. From the scale of figures for Q_{zt} and Q_{xt} it is seen that values of Q_{xt} are at least ten times lower than in case of Q_{zt}. Thus the optimisation should be more focused on the axial trapping rather than transverse trapping forces.

Another important factor that was considered in the microchip design was the linearity and the working distance of the axial forces. Small waveguide sizes make the confinement range along the z-axis very short as well as causing fast degradation of the linearity of trapping efficiency. This in combination with the reposition of the object by external factors along the z-axis might induce loss of trapping confinement of the object. It is apparent that axial forces do not vary significantly with particle size changes but they experience a major influence due to beam separation variations, which should be precisely adjusted (Figure 3-2). In some cases shape deviations appear (Figure 3-5). This is a result of model limitations and approximations used when creating the theoretical model such as Snell's law approximation etc. However as it was stated previously, these inaccuracies can be neglected for our application.

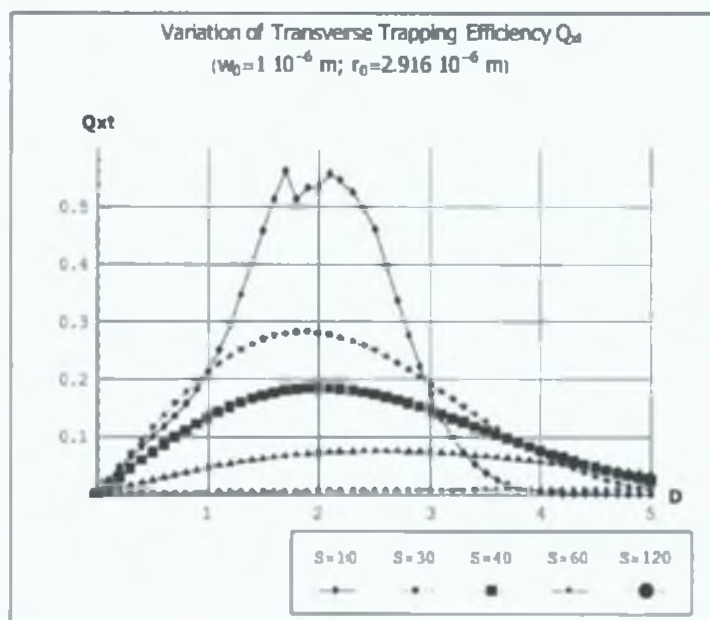

Figure 3-5. Variation of transverse trapping efficiency vs. microsphere displacement for different separation distances of the waveguide endfaces.

In order to meet two major objectives ı e high transverse force efficiency and highly negative and linear axial efficiency slope, the following waveguide sizes (ws=$2w_0$) for the prototype device were selected

- for particle radius r_0=1 4185 10^{6} m (Figure 3-6)
  ws=2x10^{-6} m with s=20x10^{6} m, and ws=4x10^{-6} m with s=40x10^{6} m

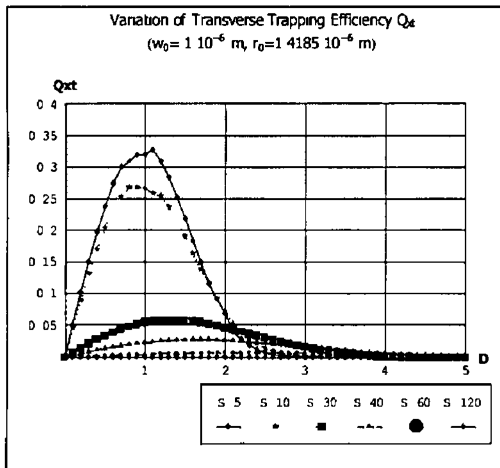

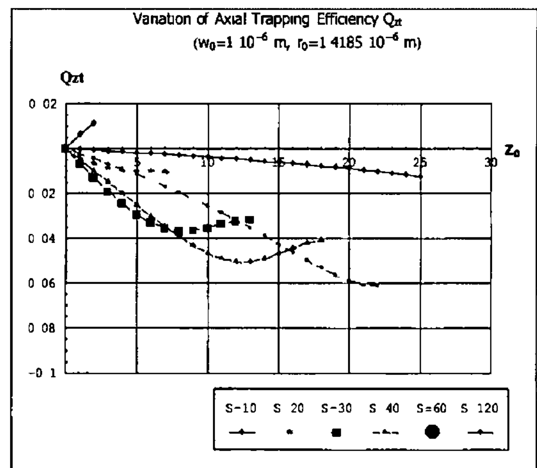

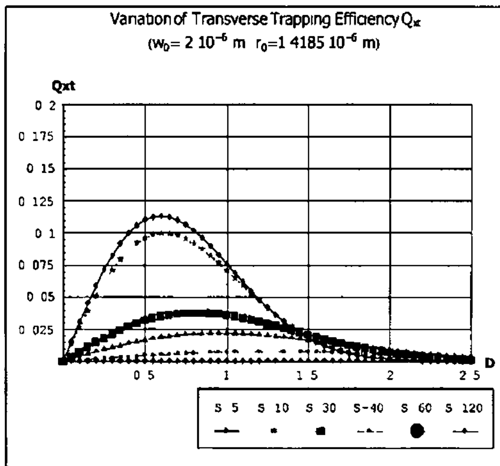

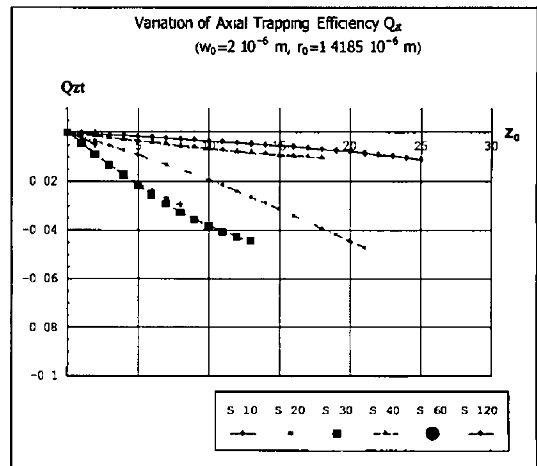

Figure 3-6 Optical efficiency graphs for particle radius r_0=1 4185 10^{6} m

- for particle radius r_0=2 916 10^{6} m (Figure 3-7)
  ws=4x10^{6} m with s=80 10^{6} m, and ws=6 10^{6} m with s=90x10^{6} m

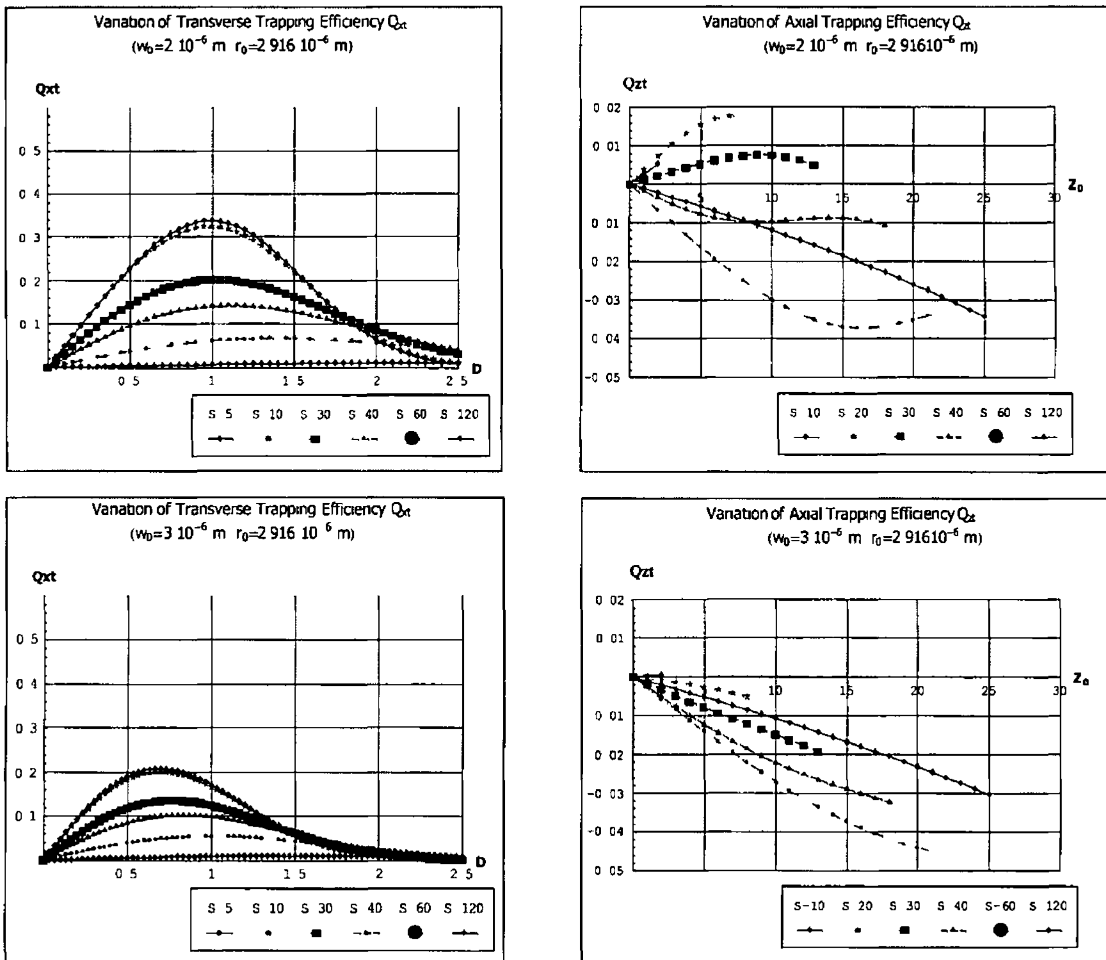

Figure 3-7 Optical efficiency graphs for particle radius r_0=2 916 10^{6} m

- for particle radius r_0=4 57 10 ^{6} m (Figure 3-8)
  ws=8x10 ^{6} m with 160x10 ^{6} m, and ws=10x10 ^{6} m with s=200 10 ^{6} m

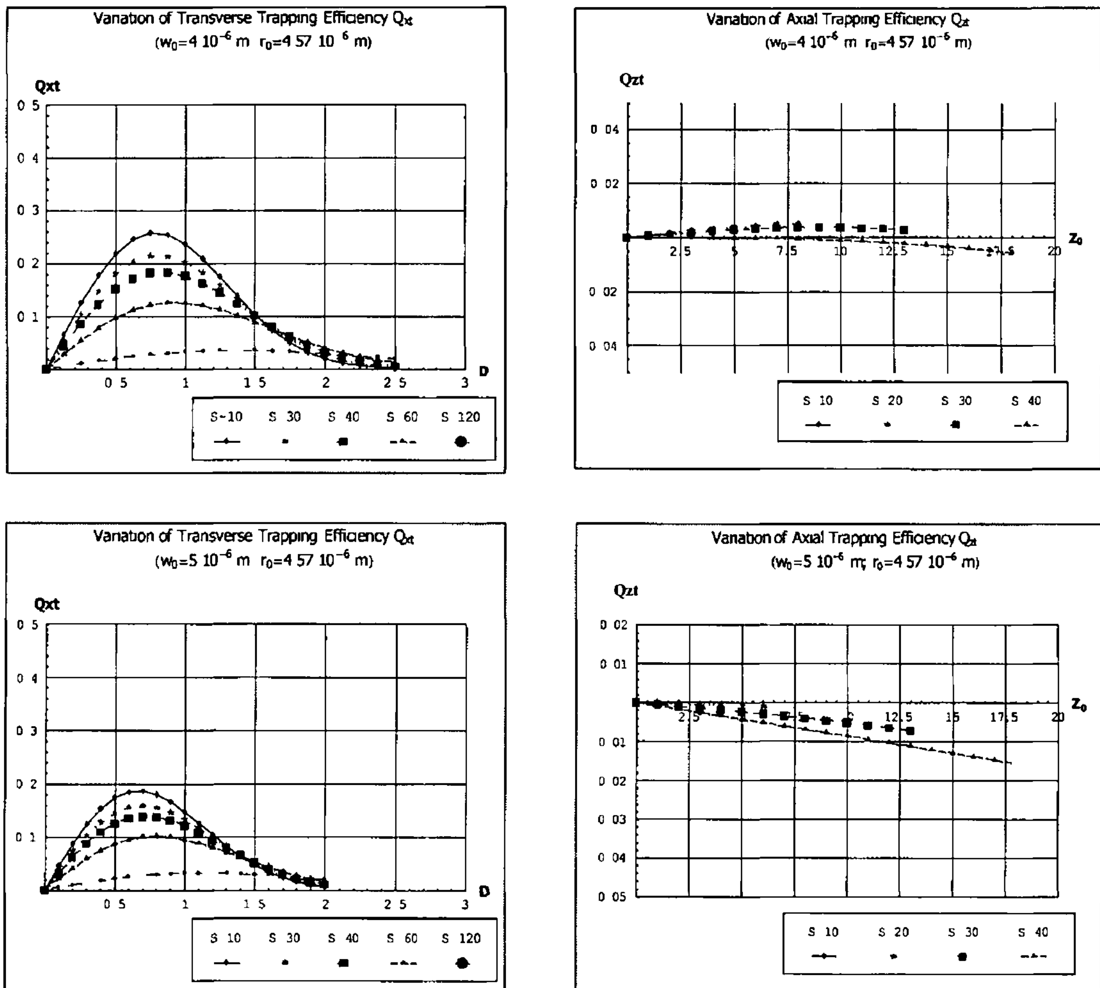

Figure 3-8 Optical efficiency graphs for particle radius r_0=2 916 10 ^{6} m

The specification however may vary depending on the application and for that reason the photolithography mask incorporated a structure (see Chapter 6 Mask Design) that was designed for testing all cases considered in the calculations

3.3. Refractive Index Step Calculation for Single Mode Waveguides

Calculations of trapping efficiency explicitly assumed that the beam propagates on a single mode basis. The excitation of other modes could have resulted in unnecessary loss of optical power along the waveguide [55,56] and even more importantly they might have caused the appearance of other equilibrium points. This would decrease the trapping efficiency and would be inconsistent with the presented LTM concept.

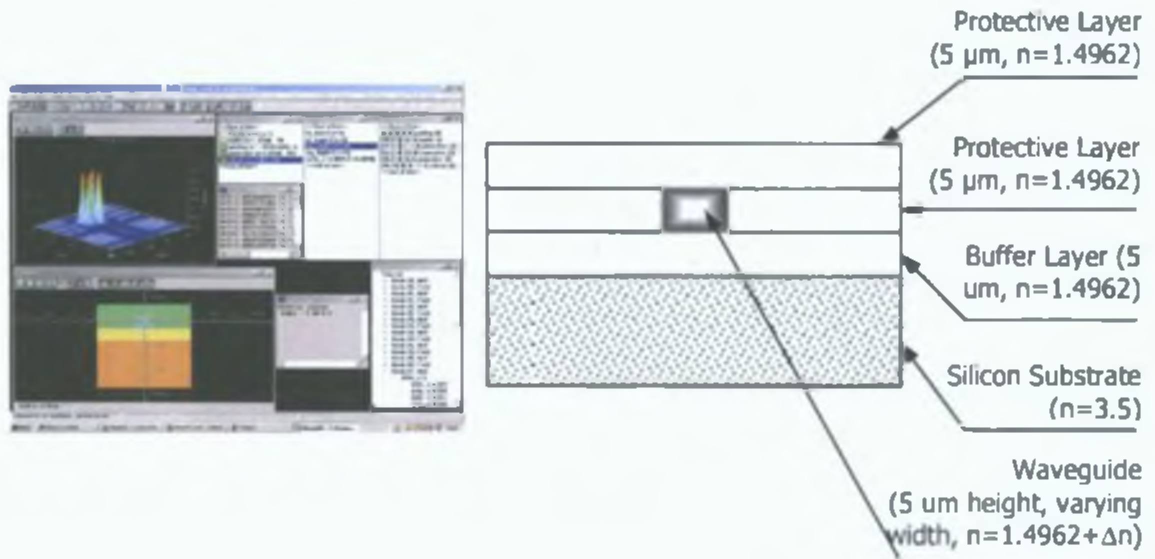

Figure 3-9. Optical modes propagation model

In order to make a single step refractive index waveguide capable of guiding only the TE_{00} mode of light, both the size of the waveguide and its refractive index difference between core and cladding must be established. Calculations of trapping efficiency revealed that a beam waist of between 1 μm and 5 μm results in optimal trapping conditions. This covers a wide range of particle diameters from 2.8 μm to 9.16 μm.

Taking this into account, simulations were performed using C2V Selene Software in order to find the modal excitation distribution and the refractive index difference that would allow single mode light guiding for almost all considered waveguides diameters (Figure 3-9).

The model of a rectangular waveguide on a 5 μm buffer layer and covered with two protective layers, all on a thick silicon substrate, was created. During calculations the height of the waveguides was kept constant while their width was changed in the

range between 2 µm and 10 µm. The constant height was selected in order to simplify the fabrication process and make it less time consuming in the primary stage of prototype testing. Since all waveguide sizes were fabricated from the same mask, preparation of specific devices serving particular microparticle diameters with distinctive guiding layer height would require additional process adjustments.

Since the LTM research was focused primarily on demonstrating the functionality of the device therefore precise adjustment of the guiding layer was not in the scope of this work. For that reason the fabrication process was adjusted to deliver 5 µm high waveguides on the single 4-inch wafer, which is in the middle range of all considered cases.

Figure 3-10 and 3-11 shows the effective refractive indices (related to each existing propagating TE mode) plotted versus refractive index difference of the waveguide for each waveguide width.

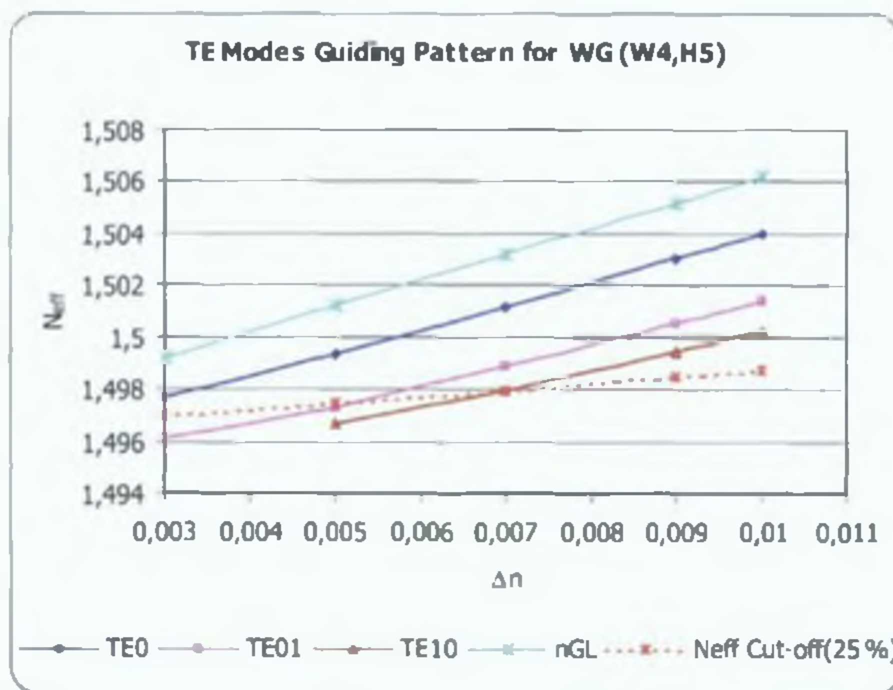

Figure 3-10. Optical modes calculated for waveguides width 4 µm and height 5 µm for the optical wavelength of 662 nm

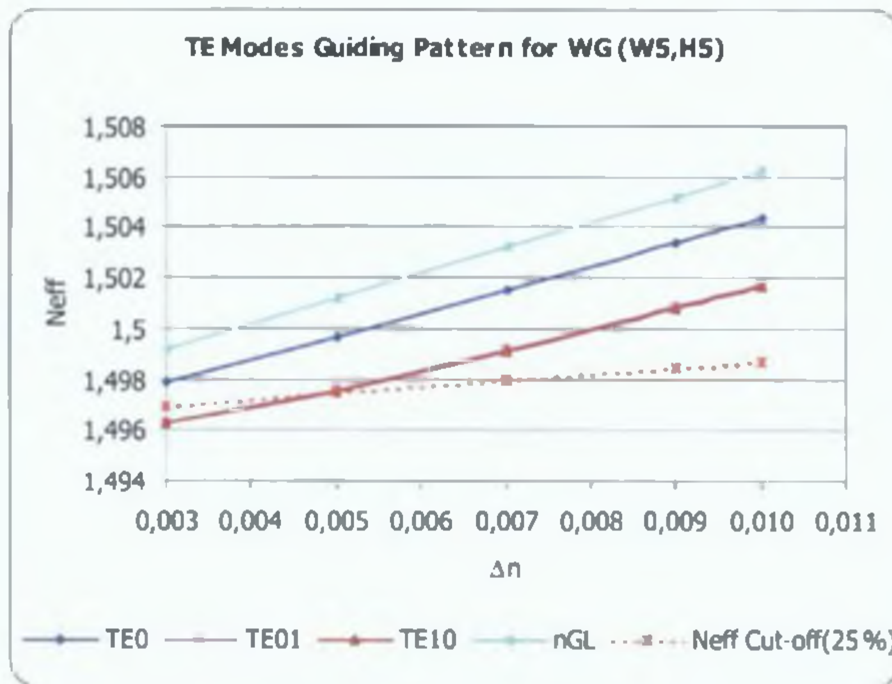

Figure 3-11. Optical modes calculated for waveguides width 5 μm and height 5 μm for the optical wavelength of 662 nm

As a base, the cladding (buffer and protective layer) refractive index of 1.4962 was selected. The straight cross-marked lines on Figure 3-10 and 3-11 denote the refractive index of the core for the value 1.4962+Δn with Δn varying from 0.003 to 0.01.

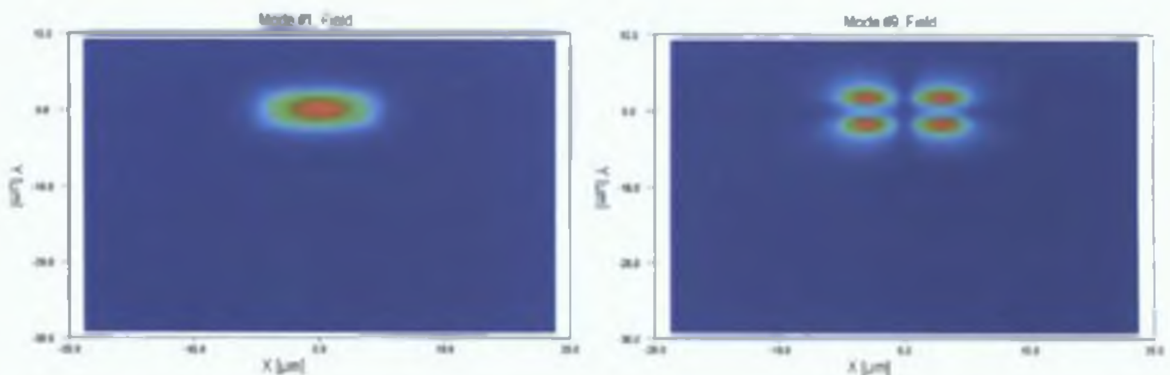

Figure 3-12. Sample of the optical modes from the simulation.

From wave-guiding theory [57], it is known that every mode can be characterised by its distinctive effective refractive index (N_{eff}). The closer the value of the effective refractive indices of the modes to the refractive index of the guiding layer the more confined they are and more initial power is transferred to these modes. This implies

that higher order modes tend to appear as the Δn increases The importance of selecting the biggest possible Δn whilst maintaining the single mode operation is that with a very small Δn the fundamental mode experiences heavy losses due to extension of its evanescent field in the cladding [58] A tradeoff had to be achieved between these two situations so $N_{eff} = n_{buff} + 25\%\Delta n$ was arbitrary chosen as a cut-off boundary (dashed lines in Figure 3-10 and Figure 3-11)

From the plots it can be observed that when waveguide widths grow relative to their heights, N_{eff} of mode TE_{10} becomes larger that that of mode TE_{01} Additionally, increases in waveguide width make it difficult to keep their single mode properties and for widths over 6 µm even a refractive index difference of 0 003 and the 25% cut-off assumption is not sufficient to only carry the fundamental mode of the beam

It is expected that in the event of a second mode propagating in the waveguide the optical scattering losses of this mode will be significant Thus the unwanted mode will be attenuated and the majority of power transmitted will be in the desired TM_{00} mode Therefore a Δn of 0 003 was selected, which should support a single mode operation of the LTM device

3.4. Light Propagation Simulation

The last stage of the LTM theoretical model investigation was a simulation of the laser beam shape exiting the waveguide endface inside the microchip housing. The primary aim of the simulation was to obtain an understanding of the light field distribution at a certain distance from the endface of the waveguide (especially in the vicinity of the point where laser trapping occurs) and to compare the entrance and end field intensity distributions. The secondary purpose of the simulation was to evaluate the influence of a situation when the waveguides endface is tilted by an angle in the plane perpendicular to the optical axis.

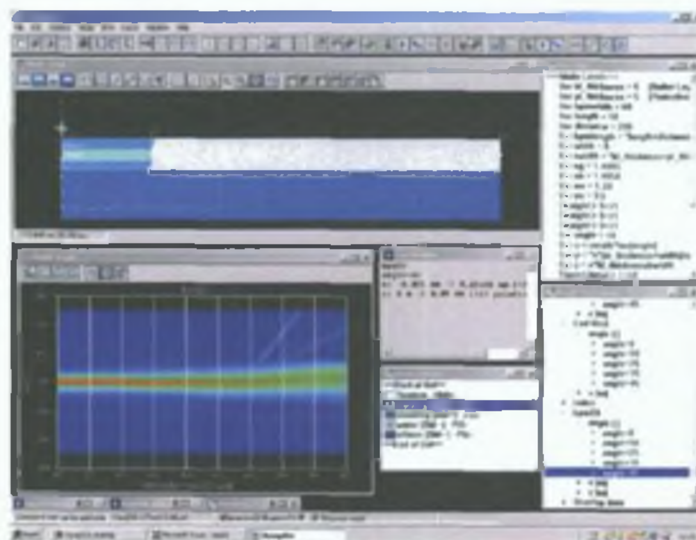

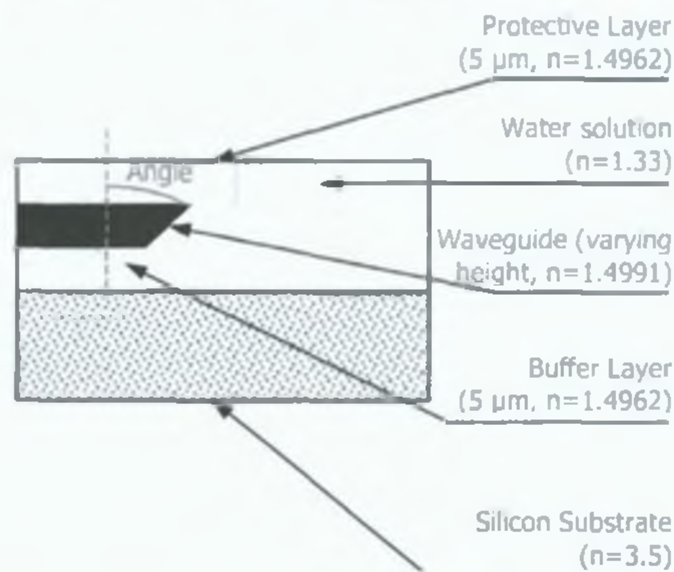

Figure 3-13. Light propagation simulation model

The simulation was performed using C2V Prometheus Software and was carried out for the optimised parameters, which were the results of the optical trapping efficiency calculations. Following these calculations the simulation was carried out for a range of waveguide heights between 2 and 10 µm.

The actual refractive index values of the optical materials used for fabricating each layer of the microchip were obtained using the prism coupling technique (see Chapter 4) on a Metricon Corporation system. Those values were introduced to the program and the resulting refractive index of the model can be seen in Figure 3-13 and Figure 3-14

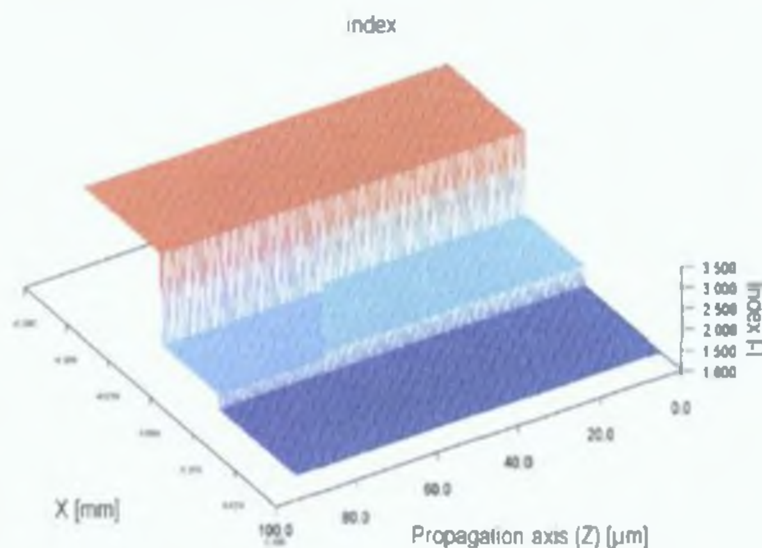

Figure 3-14. Refractive index step for the LTM light propagation simulation.

The tilt of the waveguide endface was varied in the simulation between 0° and 45°. The entrance field was assumed to be single mode with a Gaussian intensity distribution with a FWHM (Full-Width Half-Maximum) of 4 µm and a wavelength of 662 nm (Figure 3-10)

The simulations revealed no distortions in the field shape propagating to the centre point between both waveguides for perpendicular waveguide endfaces. However, irregularities like tilted or angled faces have an influence on the beam shape and its relative position to the initial propagation axis of the beam (Figure 3-10).

It is shown in Figure 3-10 (for the waveguide height of 5 μm) that at a distance of 40 μm from the point where the beam enters the water solution a 10 degree angled endface (which is very unlikely for the production technology used) causes about 0.5 μm optical field displacement from the centre of the optical axis. Since the misalignment of the counter-propagating beam for this angle is very small and occurs in the same direction for both beams (as the chamber is made in the same process for both) it should have a marginal influence on the trapping properties. Additionally for 5 μm waveguides and an end field distance of 40 μm, even when the distortion occurs there are no significant changes in the Gaussian field distribution, which is the key for the efficient optical trapping.

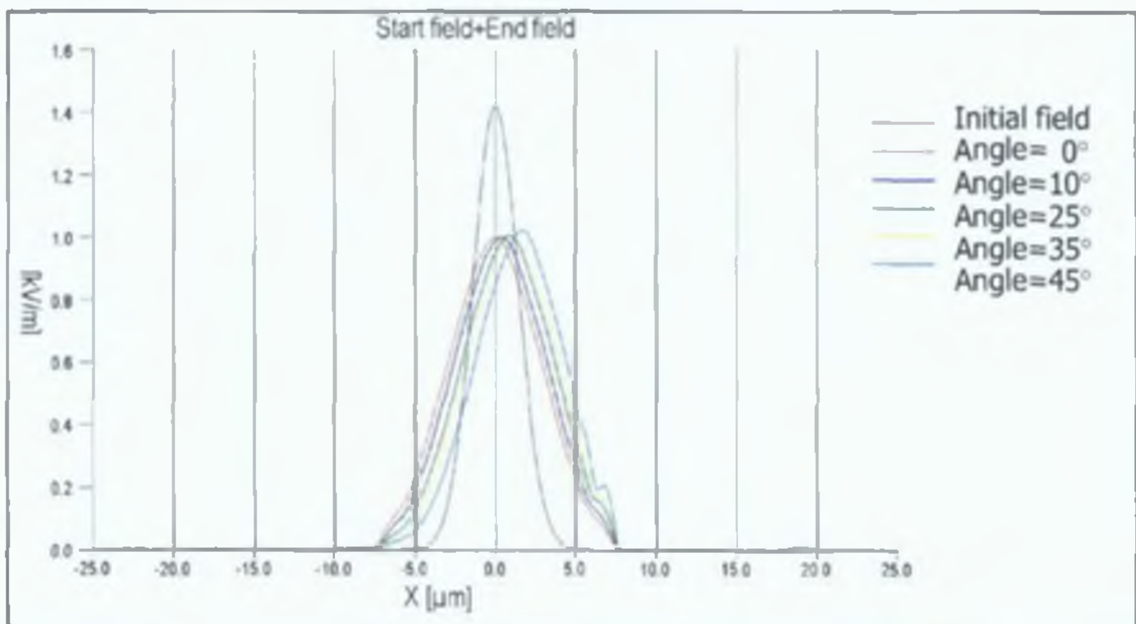

Figure 3-15. Start and end optical intensity fields at a distance of 40 μm for a waveguide of 5 μm height

In the case of the far field distance from the waveguide endface (100 μm) and high angled waveguide, the Gaussian beam shape becomes more irregular and the situation become even worse for bigger waveguide sizes (Figure 3-16 and Figure 3-17). In the prototype device the guiding layer has a thickness of 5 μm, therefore most cases are covered by the optical fields presented in Figure 3-10.

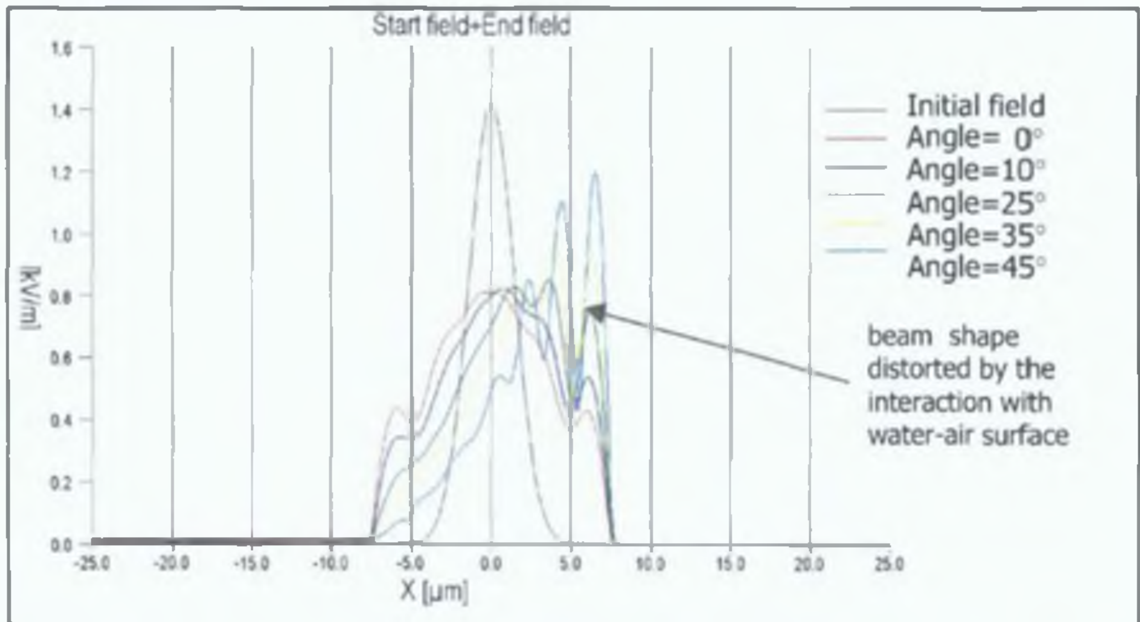

Figure 3-16. Start and end optical intensity fields at a distance of 100 µm for a waveguide of 5 µm height

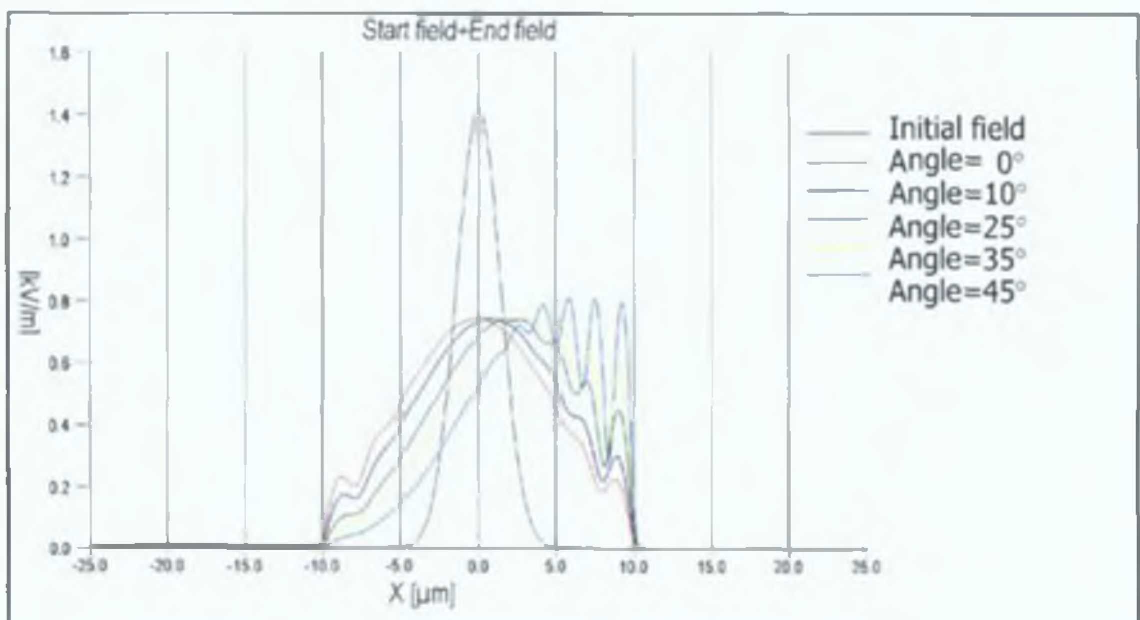

Figure 3-17. Start and end optical intensity fields at a distance of 100 µm for a waveguide of 10 µm height

Most of the considered separation distances are very small with very few reaching 200 µm. Thus they should not be affected by the quality of the process used in trap housing fabrication. These few however should provide an opportunity to measure and observe the influence of the beam distortion on a trapped object.

The selected fabrication process, reactive ion etching, typically does not create structures with features angled more than a few degrees and thus the beam shape should be close to that depicted in Figure 3-18.

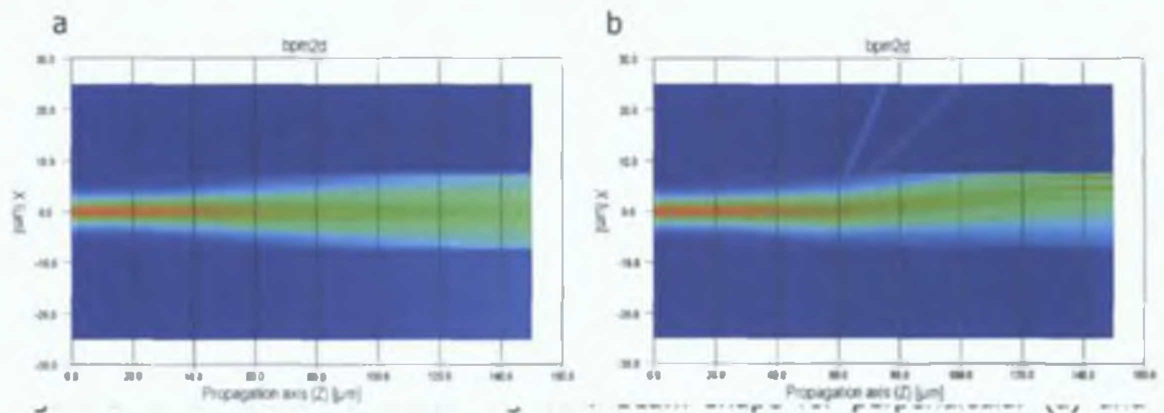

angled (b) waveguide endface.

3.5. Conclusion

The main objective of the presented calculations was successfully achieved. Numerical estimations required for the final optical trapping force calculations enabled optimisation of the optical trapping parameters with respect to LTM waveguide sizes, beam waist separations and object size.

It was shown that for the LTM device, the larger the radius of the object, the larger the waveguide size and the beam separation is required in order to provide stable and efficient trapping. Specifically, for the intermediate particle size (r_0=2.916x10^{-6} m), the optimum trapping efficiency is obtained for a 4 μm waveguide width and the beam waists separation of 80 μm.

The optical profile was another crucial factor, which was investigated. As presented in the theoretical model, a Gaussian intensity profile of the counter-propagating laser beams is required in order to produce a single trapping equilibrium. It was shown that obtaining such Gaussian profiles for the waveguide considered meant that the refractive index difference should not exceed a value of 0.003. Therefore this value was used during material design. It was also argued that the guiding layer thickness of 5 μm would provide a stable trapping point for all the considered cases and simplify the prototype fabrication process.

Finally, a simulation was performed to evaluate the impact of the waveguide endface perpendicularity on the propagation and shape of the beam intensity profile resulting from the quality of the fabrication process The major conclusion from these simulations was that there is a high tolerance available for the fabrication process as the change in the directionality of the beam is negligible even with the endface angled by as much as 10θ. However this impact becomes higher as larger waveguides are considered

The numerical calculations and simulations also helped in minimising time, cost and risk involved in the fabrication of the LTM prototype as the selection of the fabrication technologies was now based on strict requirements with regard to shape, quality and the geometrical parameters of the device

4. Properties of the Materials Used

4.1. Introduction

To implement the LTM concept one of the major objectives of this work was the selection and development of a material that could be easily tranformable into light guiding embedded ridge structures and would be able take advantage of the photopatterning technology This implied that not only its refractive index should be easily adjustable, but its molecular structure should allow rapid polymerisation of the material in the presence of the ulraviolet light (photopolymerisation) Based on this objective the initial intention was to synthesize a photopatternable material using a sol-gel technology by taking advantage of its variuos positive physical, chemical and optical properties To achieve this it was necessary to develop multiple material fabrication methodologies which included the following requirements

- Optimal properties for thin film deposition using the spincoating technique involving minimal thickness variations (striation free film) after coating and a reduced edge effect

  Spincoating is often a technique of choice for coating large substrates such as 4-inch silicon wafers and produces highly uniform films for optimised materials and coating conditions [59-61] The uniformity of coating thickness is an important quality for producing repeatable micron sized optical paths Thus it directly influences the intensity losses and the quality of the modal distribution of the electromagnetic field travelling through the optical path During the fabrication of the optical trap housing, any change in the coating thickness contributes to uncertainty in the process time employed to produce a certain chamber depth

  The edge effect, which appears during spincoating film deposition, is a consequence of surface tension effects This makes it difficult for the solution, that is flowing radially outward, to detach from the wafer This results in an increased thickness of the spincoated material around the entire perimeter of the substrate If better uniformity can be maintained out to the edges then more area can be

used for device fabrication and enhancing photolithography mask contact properties

- Precise control of the refractive index in order to obtain Δn=0 003 between the waveguide and cladding (buffer and protective) layers

- Greater stability and durability allowing for extended storage time between material synthesis and deposition

  Changes in the properties of the material such as viscosity or speed of photopolymerisation have a serious impact on the properties of the final device Specific concerns about viscosity changes over time were experimentally addressed to reduce the thickness variation and the device surface uniformity

- Low optical propagation losses

  Optical propagation losses are related to the physical and chemical properties of the material They are related to the transparency of the material to the propagating light and involve physical phenomena such as light scattering and absorption with the former mostly related to the uniformity and the roughness of the guiding structure [62] The material is expected to generate the lowest possible attenuation of the electromagnetic field in order to produce the optical trap of the highest possible trapping forces

- High photolithographic contrast or low Critical Modulation Function allowing for 4 µm size feature to be resolved separated by a distance of no less than 6 µm

  The contrast is an important feature of every material used in the photolithography process [63], it determines the spatial resolution achievable for the patterned features It is defined as

$$\gamma \quad \frac{1}{\log_{10}\frac{D_f}{D_0}}$$

Equation 4-1

D_f and D_0 are exposure doses where the material becomes entirely polymerised or not polymerised at all (Figure 4-1)

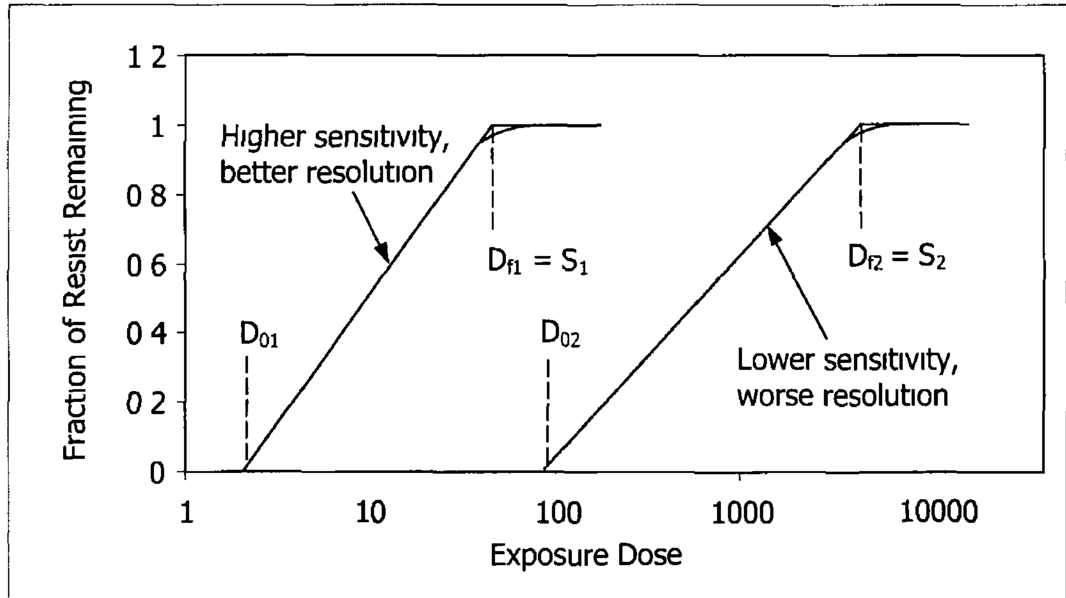

Figure 4-1 Material contrast function

The photopatternable qualities of the material can also be represented by a Critical Modulation Function (CMTF), which is defined as

$$CMTF = \frac{D_f - D_0}{D_f + D_0} = \frac{10^{1/\gamma} - 1}{10^{1/\gamma} + 1}$$ Equation 4-2

Lower CMTF values give better resolution and feature quality from the photolithography process

The combined material features were used to set the criteria for selection and synthesis of the material used in LTM fabrication The material chosen to fulfil all the above requirements was a photopatternable composite produced using sol-gel technology

4.2. Sol-gel Materials

During the second half of the 20th century sol-gel technology has gained increasing attention from the scientific community as a source of inorganic and composite organic-inorganic materials A relatively simple low-temperature production process combined with easy control of the physical and chemical properties of sol-gel materials has generated much interest within the optics and optoelectronics industries [62,64-72]

The fundamental sol-gel chemical process is relatively easy to understand involving the evolution of solid-state materials from a molecular liquid phase The most common way of processing sol-gel involves the use of metal alkoxides through hydrolysis and condensation reactions of the precursors [73-78]

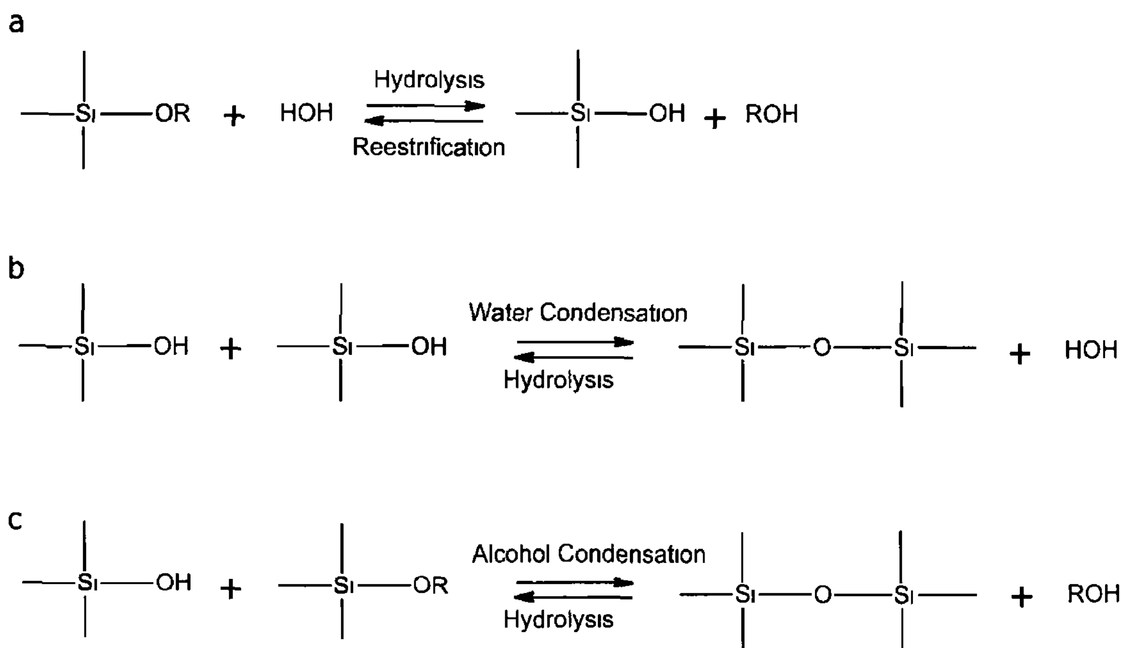

Figure 4-2 Basic reactions involved in the organosilicon material synthesis (a hydrolysis, b water condensation, c alcohol condensation)

In reaction a (Figure 4-2) alkoxide groups (OR) are replaced with hydroxyl groups (OH), which produce a silanol species (Si-OH) and alcohol ROH Two further reactions, water condensation and alcohol condensation occur In reaction b (Figure 4-2) two silanol species react producing siloxane bonds (Si-O-Si) and water as a by-product

Alcohol condensation (reaction c Figure 4-2) involves silanol and alkoxide species reacting, resulting in the creation of siloxane bonds and alcohol as a by-product

Under most conditions, condensation takes place before hydrolysis is completed Since water and aloxides are immiscible (i e they are incapable of mixing) an alcohol solvent (e g ethanol) is typically utilised to improve the quality and homogeneity of the reaction Further condensation proceeds while water and alcohol evaporate and are driven off from the system Although it is possible for hydrolysis to occur without the addition of an external catalyst it is preferable to add one in order to make the whole reaction more rapid and complete For that purpose mineral acids (e g HCl), ammonia, acetic acid, KOH, amines, KF, and HF are commonly used

For the purpose of the LTM fabrication, a photopatternable optical quality material was developed and prepared via a classical hydrolytic sol-gel route [79,80,81,82] The material was based on a typical photopatternable sol-gel composition, which contains two parts the organic component (responsible for UV cross linking properties) and the inorganic one (composed of SiO_2 chains) (Figure 4-3)

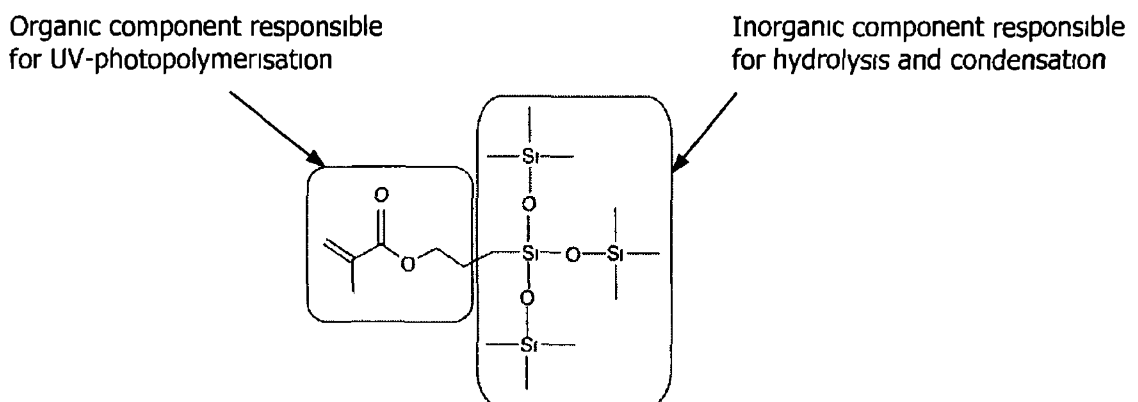

Figure 4-3 General composition of a typical photopatternable sol-gel material

The utilisation of the material organic part for photopatterning required the material to be combined with the suitable cross linking agent (photoinitiator) The cross linking molecule is responsible for the material polymerisation when exposed to the correct wavelength of light For this reason the photoinitiator type and quantity directly influences the photopatterning quality of the material

A photoinitiator Irgacure 819 was chosen for its excellent light absorption properties near the wavelength of 365 nm, which is the operational wavelength of the UV-exposure system used for the LTM fabrication (Figure 4-4)

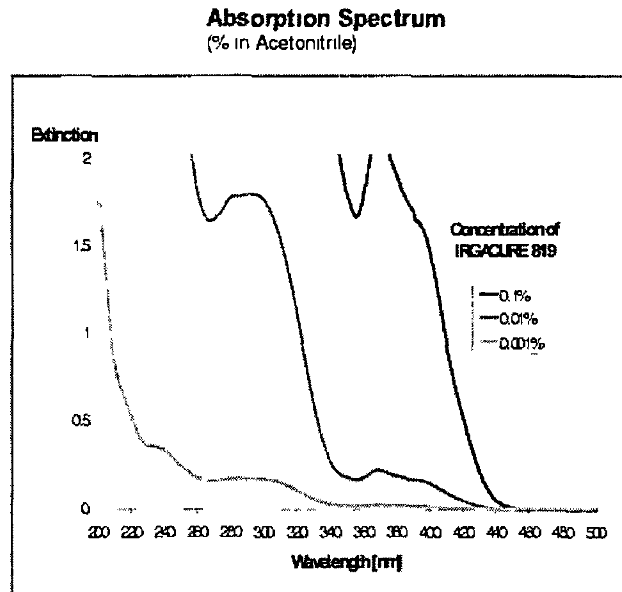

Figure 4-4 Irgacure 819 absorption spectrum (source Ciba Speciality Chemicals photoinitiator specification)

The content of the photoinitiator was modified experimentally to the value of 1 8% in order to match the sensitivity (S - Figure 4-1) to the output power of the mask aligner

Another crucial task during the sol-gel material development was a modification of its refractive index in order to match the LTM specification The refractive index difference (Δn) between the buffer layer, protective layer and the guiding layer was obtained by doping the material with Zirconium [83-86] A desired value of Δn=0 003 was achieved by adding in molar quantities 4% of Zirconium to the guiding layer and 2% of Zirconium to both buffer and protective layer

The refractive indices of the materials were measured using a Metricon 2010 Prism Coupler, which utilises optical waveguiding techniques to rapidly and accurately measure both the thickness and the refractive index of dielectric and polymer films In an automated measurement, the tool offers a refractive index accuracy of ± 001 and resolution of 0 0005

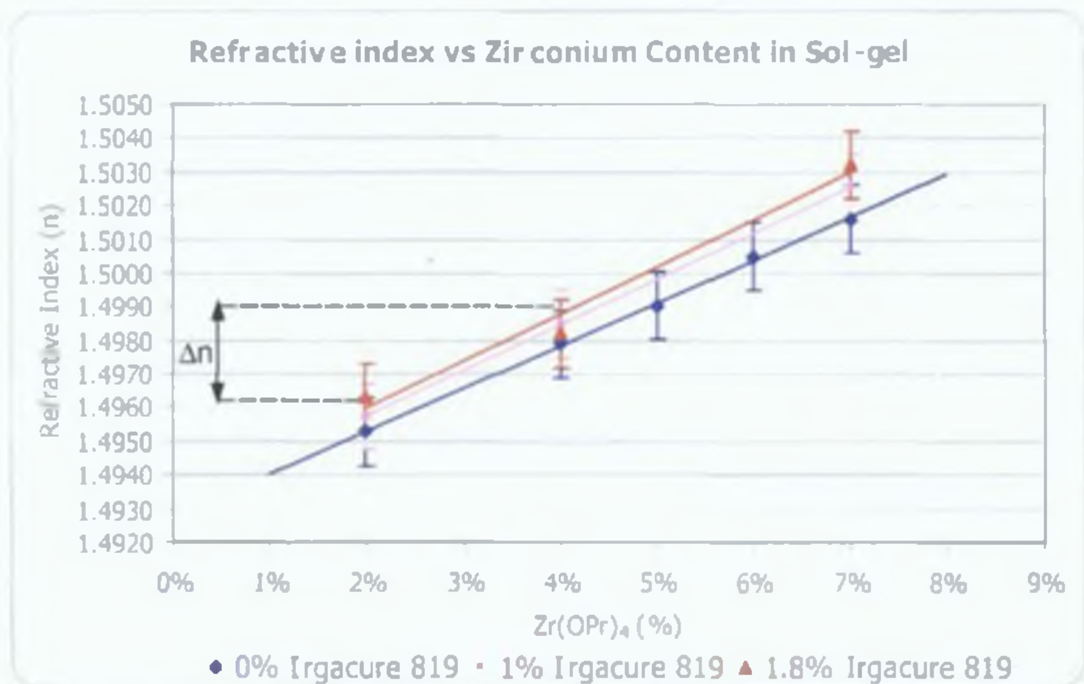

Figure 4-5. Refractive indices of the sol-gel obtained using the Metricon prism coupling technique for a single wavelength (632 nm)

Experiments conducted revealed that for every 1% of added Zirconium tetrapropoxide a change in the absolute refractive index of 0.015 occurred as shown in Figure 4-5. Addition of photoinitiator (Irgacure 819) also accounted for a change in the absolute refractive index of each layer and although its influence is minor, the photoinitiator was added to all layers to entirely reduce its effect on the Δn value.

The final material synthesis involved MAPTMS (methacryloxypropyltrimethoxysilane) and a complex issue from the chelation of the zirconium n-propoxide ($Zr(OPr)_4$, Aldrich, 70 % in 1-propanol) and methacrylic acid (MAA, Aldrich, 99%), as depicted in Figure 4-6.

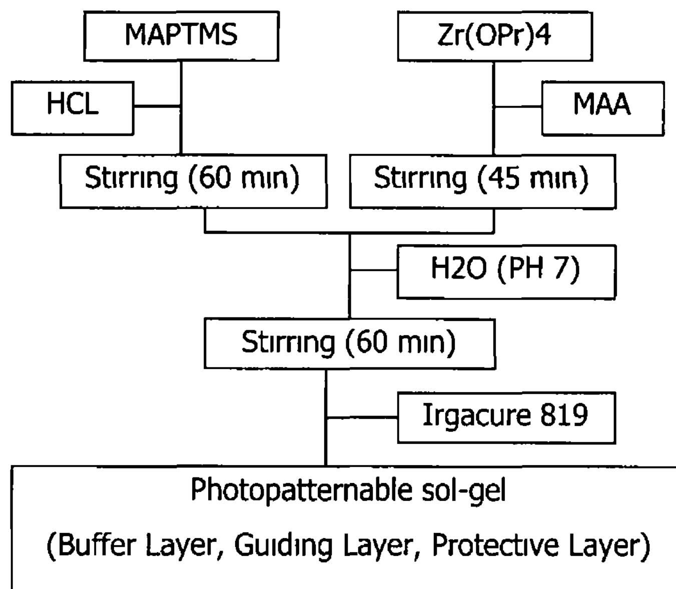

Figure 4-6 LTM Material Synthesis Process

The photosensitive property was produced by MAPTMS, which possess a methacrylate group that permits polymerisation upon irradiation with UV-light MAPTMS was hydrolysed with an aqueous solution (HCl 0 01N) employing 2 1 water to alkoxide ratio The solution was then stirred for 60 minutes at 80 °C to produce a homogeneous sol Independently, MAA was added to $Zr(OPr)_4$ with a 4 1 acid to zirconate molar ratio, and stirred for 45 minutes at ambient temperature This formed a complex,which reduced the high hydrophilicity of the zirconium nuclei The MAPTMS was then added dropwise to the zirconate Following another 45 minutes, a further hydrolysis was performed, employing a pH 7 water leading to a final ratio MAPTMS $Zr(OPr)_4$ MAA H_2O of 50 1 4 5 Finally the 1 8% photoinitiator Irgacure 819 (Ciba Specialty Chemicals) was addded giving the material its UV-photopolymerisation property

In the course of the research the thin film (and the overall device) thickness variations were taken into consideration Since the film thickness produced by the spincoating technique is directly dependent on the viscosity of the material [87], any time related rise in the material viscosity automatically increases the thickness variations between fabricated wafers or even between each layer of the same wafer

In the case of sol-gel materials, the viscosity stability over time is of particular concern due to its relatively fast rate of change The main factors responsible for this

phenomenon are the solvent evaporation from the material and continuously ongoing chemical reactions inside the sol-gel. The longer the aging time the higher the viscosity [76] of the sol-gel material.

The viscosity changes were measured using a Brookfiled DV-II+ viscometer with nominal accuracy of ±1% and repeatability of ±0.2% for different water/sol ratios. An averaged value was derived for each point in time from the moment the sol-gel achieved full synthesis (Figure 4-7).

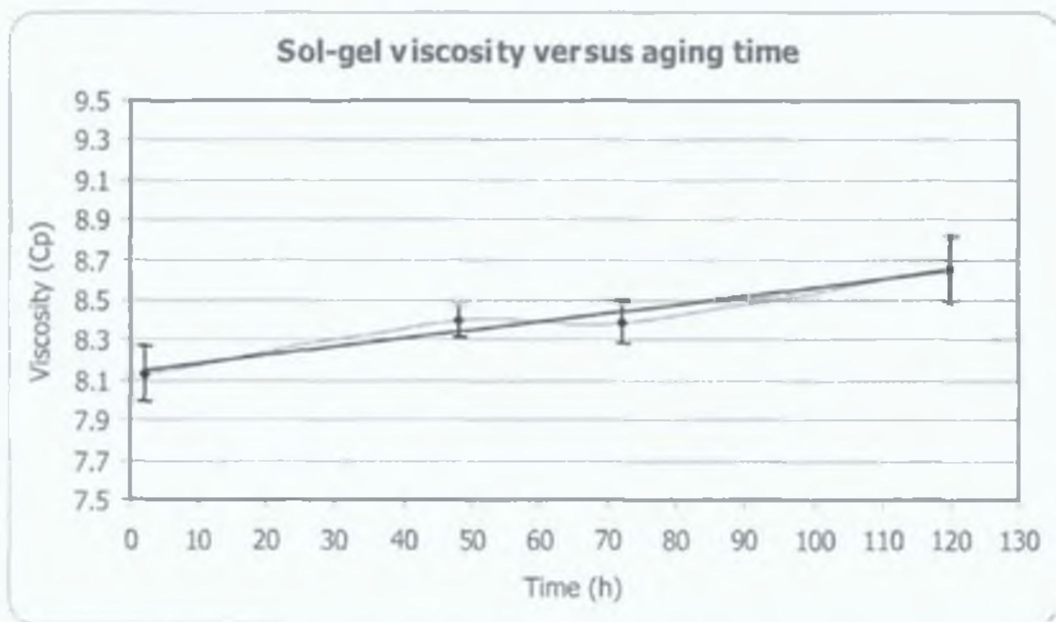

Figure 4-7. LTM sol-gel viscosity versus aging time

The results show that the initial absolute viscosity of 8.15 Cp increased to 8.65 Cp after storing the sol-gel at ambient temperature for 120 hr. Based on the direct relation between viscosity and the spincoated film thickness this change would account for a 10% change in each layer thickness. In order to minimise these differences prepared materials were used within 48 hr from the preparation and were stored at low temperature in order to slow down the chemical reaction within the material. This allowed good repeatability of the overall thickness of the device.

In order to obtain striation free films and reduce edge effects the spincoating process was optimised and samples were coated in a saturated Isopropanol atmosphere. The occurrence of striations is thought to arise due to evaporation driven surface tension effects. The early evaporation of a light solvent can cause an enrichment of water

and/or other less volatile species in the surface layer If the surface tension of this layer is larger than the starting solution (which still exists at deeper levels), then instability exists The higher surface tension draws material in at regular intervals creating spaces where the solvent can evaporate The surface relief that develops, results in film thickness variations Using a saturated solvent atmosphere during spincoating helped to reduce the solvent evaporation and produced silica films on silicon of better quality [59]

4.3. Conclusion

For the purpose of the LTM development an organic-inorganic composite material was synthesised, which possesses all the qualities required for the successful fabrication of the device The inexpensive and easy to synthesize material proved to be highly stable over time and it was optimised to provide the desired refractive index difference between buffer, protective and guiding layer The photopatternable properties of the material were developed and in combination with the photolithography process allowed waveguides of desirable dimensions and optical properties to be fabricated (see Chapter 7)

5. Fabrication Process

5.1. Introduction

The device fabrication process was designed to fulfil the requirements presented in the previous sections to match the properties of the chosen material. These include:

- Fully automated large volume fabrication combined with small device size

  Large production volumes and relatively low cost technologies should be employed to reduce the device fabrication costs. This should in turn allow the LTM to be affordable for the target market consisting mostly of biotechnological laboratories. A highly efficient fabrication methodology is required as the device is designed as a semi-disposable component i.e. the device can be either used once and disposed or it can be used multiple times for less sterile or demanding tasks.

  In addition the device should be able to easily fit under a microscope objective, thus allowing trapping observation. PLC technology was used to enable this facility.

- Waveguide size

  The selected technologies should allow waveguide fabrication with dimensions as low as 4 µm. In addition the waveguide dimensions (width and height) should be repeatable with a high degree of precision.

- Quality and separation of the waveguide endfaces

  The quality of the waveguide endfaces for the optical trapping can be evaluated mostly in terms of their perpendicularity to the waveguide optical axis and the accuracy of the vertical and horizontal position in front of the counter guiding waveguide.

  The influence of the perpendicularity was presented in the optical simulation section. This quality measure was especially important for bigger waveguides, and for most conditions restricted the degree of skewness to 10θ (Figure 5-1).

Good accuracy of the vertical and horizontal positioning for the fabrication process was considered to be one of the major advantages of this device compared to other counter-propagating optical traps This was one of the primary conditions that had to be met by the technologies considered

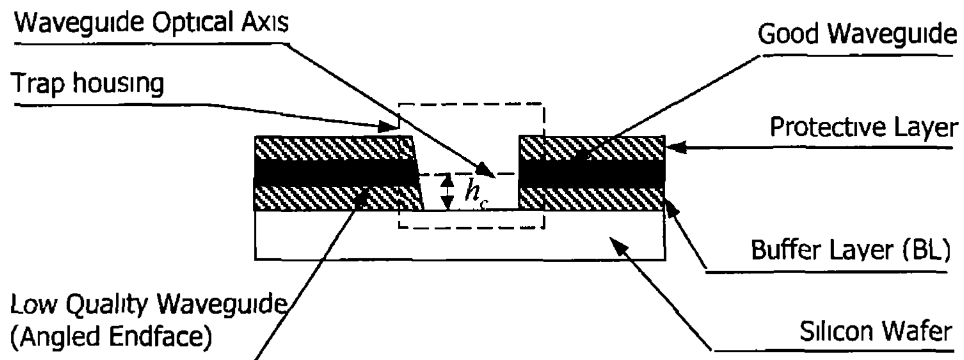

Figure 5-1 Imperfection in the quality of waveguides

- Distance between the bottom surface of the device chamber and the centre of the waveguide

Ideally the particle chamber should be deep enough to protect the laser beam from being distorted by the bottom of the trapping chamber Since the laser beam radius r_{beam} is expanding while light progresses towards the centre of the trap, the distance from the centre of the beam to the bottom of the chamber should be greater than the radius of the beam in the place where trapping occurs If however the beam waist radius is smaller than the object radius then the distance between chamber bottom and the waveguides optical axis should be bigger than the particle radius h_c ' $\max(r_0, r_{beam})$

The optical simulation (

Figure 3-15) enabled prediction and visualisation of the beam radius at the equilibrium point The radius was calculated to have a value of approximately 6 µm for a waveguide of 5 µm height, at a distance from the waveguide endface of 40 µm Taking

this into consideration a value of $h_c = 7\ 5$ µm was selected, which implied the use of a buffer layer thickness of 5 µm (Figure 5-1)

These presented requirements became the platform specifications upon which the selection of the process technologies and the final prototype design of the LTM were made

The selection of the waveguide fabrication method was in fact a choice between laser-writing and photolithography The laser writing technique uses a tightly focused laser beam to interact with the material causing photo-polymerisation The major advantage of this technique is its ability to create complicated shapes and for this reason it is often used in fabrication of PLC devices [64,68] This technology is unsuitable if large-scale fabrication is considered This problem can be overcome by using photolithography, which although less flexible in terms of changes in the design, allows high reproducibility of the results and is more suitable for commercial applications

The fabrication requirement for the trap housing was mostly related to the quality of the endfaces and the technological ability to accurately reproduce the device dimensions For this reason dry reactive ion etching (RIE) was the technology of choice (see Chapter 8)

Once it was decided to use photolithography, plasma-etching and sol-gel technology the microchip fabrication process was designed to comply with the overall system requirements

5.2. Process Steps

The base for the microchip is constituted from standard 4-inch (100mm) silicon wafers with a thickness of approximately 450 μm. The wafer was cleaned with IPA solution and kept at 90 °C for 100 min in order to promote adhesion to the surface.

Figure 5-2. Introduction of silicon wafer

A sol-gel layer was spincoated (Laurell Technologies WS-400B-6NPP-LITE Spin Processor) on top, creating a buffer layer (BL) with refractive index value of 1.4962 and nominal thickness 5 μm, followed by thermal hardening on a hot plate at 120 °C for 2 hours (Figure 5-3).

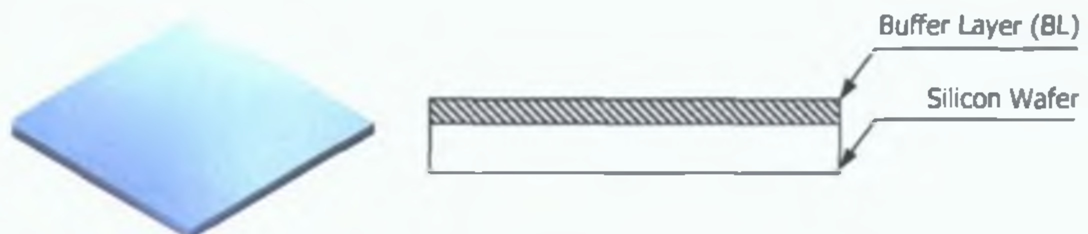

Figure 5-3. Spincoating of buffer layer (BL)

The role of the buffer layer was to insulate the waveguide from the refractive index step between it and the silicon wafer. Given that the refractive index of silicon is approximately 3.5, leaving the device without the buffer layer would prevent the light from being confined in the waveguide.

The Guiding Layer (GL) of the microchip was composed from same type of sol-gel as in the Buffer Layer. However it was modified by the addition of a higher amount of zirconium. Its function was to increase the sol-gel refractive index to 1.4991.

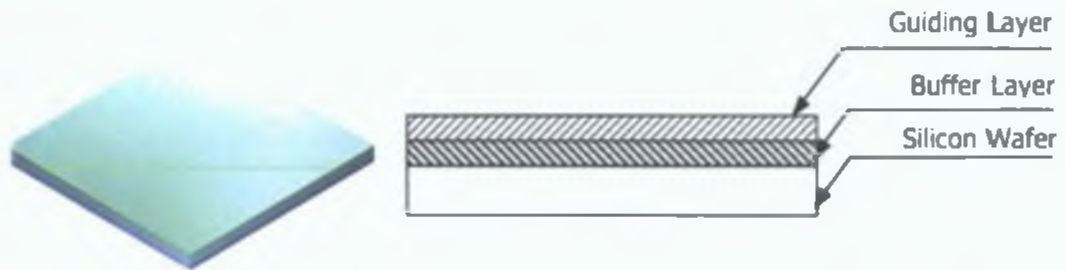

Figure 5-4. Spincoating of the Guiding Layer (GL)

The Guiding Layer (GL) coated wafer was then prebaked and placed in a mask aligner. The prebaking temperature was set to 120°C to shorten the fabrication process, reduce edge effects and allow crack free film formation. Then the sol-gel was exposed to UV light through a specially designed chromium-coated mask causing photo-polymerisation (Figure 5-5, for more details see Chapter 6).

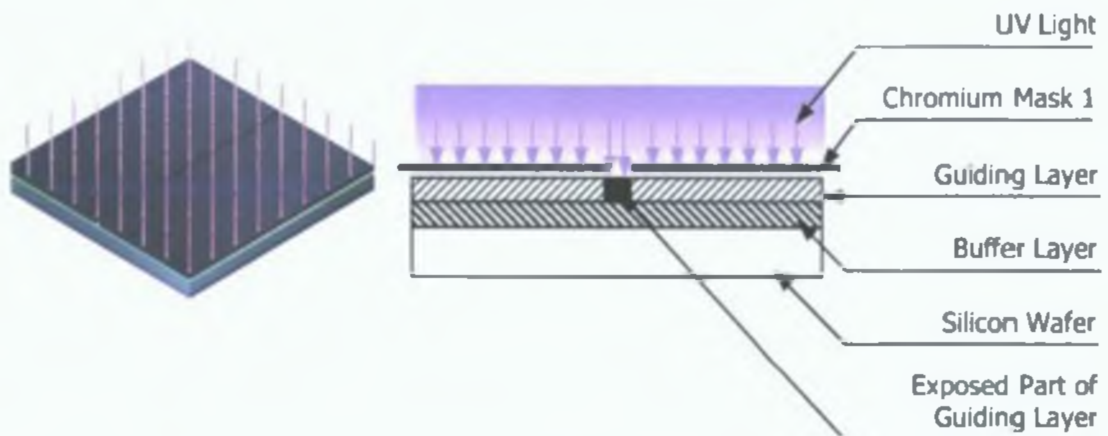

Figure 5-5. UV exposure of guiding sol-gel layer

Given that the Guiding Layer is a negatively patternable material, the unexposed part (not photocured) could be easily rinsed away with isopropanol as an etchant (Figure 5-6). The etched guiding layer creates patterns of ridges on the wafer, which form the optical waveguides.

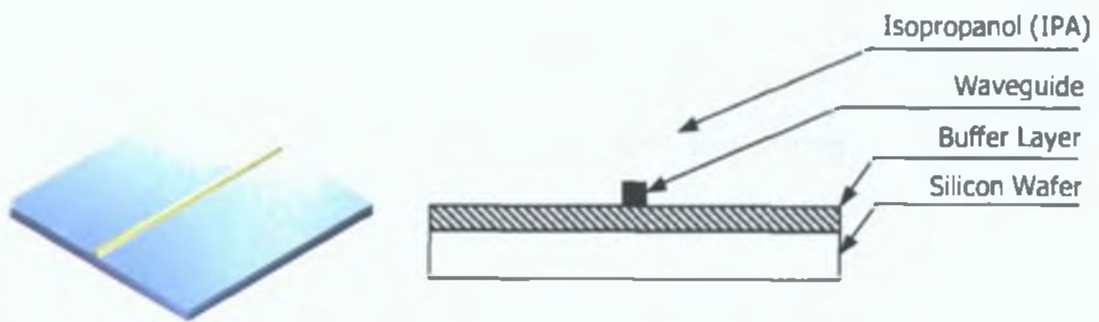

Figure 5-6. Post-exposure waveguide development

Once the waveguiding ridges were obtained, the First Protective Layer (PL1, chemically and optically identical to the buffer layer) was spincoated on (Figure 5-7). Its function was to fill the gaps between ridges (planarise the structure) and provide an identical refractive index material on all sides of the waveguides.

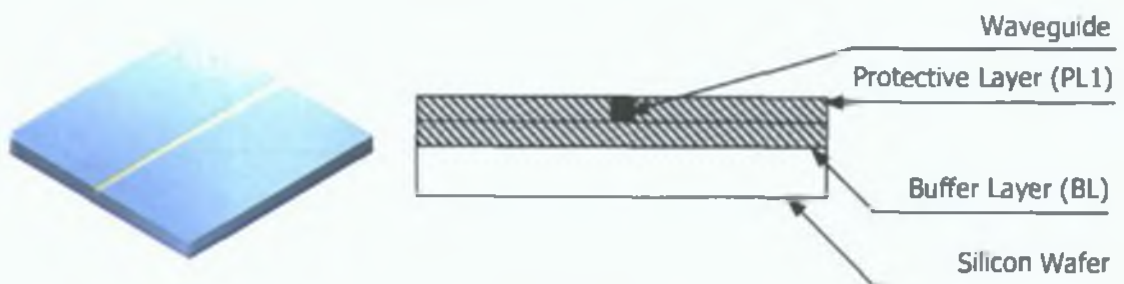

Figure 5-7. Spincoating first protective layer (PL1)

The next step in the microchip fabrication process was to spincoat the second layer of protective (PL2) sol-gel, which had a refractive index and chemical composition that were identical to the Buffer Layer, and the First Protective Layer (Figure 5-8). The role of this protective layer was to ensure that the waveguide had an identical cladding refractive index on all sides, to minimise optical losses and to maintain the quality of the Gaussian beam propagating through the waveguide. It was also used to protect the entire structure from the external environment and to provide additional height to give sufficient chamber volume for the particles if a microscope cover slip is placed on the top of the device.

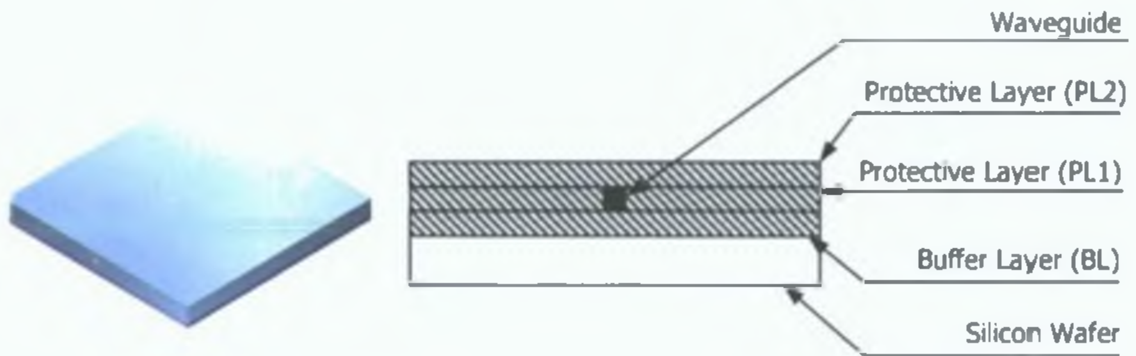

Figure 5-8. Spincoating second protective layer (PL2)

The final stages in the fabrication process were to create a trap housing using plasma-etching techniques. The processes described in the subsequent chapters were designed and optimised for etching sol-gel components in order to create a housing for the particles to be trapped in.

After spincoating the Second Protective Layer was covered with a positive photoresist material (Figure 5-9), UV exposed (Figure 5-10) and rinsed with solvent (Figure 5-11) to create a pattern for the trap housing, which later on would be exposed to the plasma etching process. The SPR-220 7.0 photoresist was selected due to its suitability for thick film deposition and exposure, easy removal with the photoresist stripper and its general availability on the market.

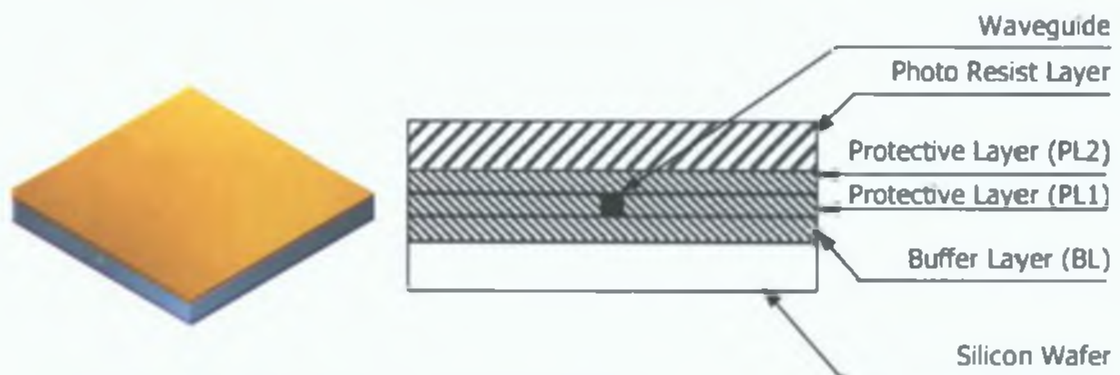

Figure 5-9. Spincoating of photoresist layer (PRL)

Then photoresist was UV exposed through the mask with the desired pattern for the sample chamber. The mask is positioned accurately over the sol-gel waveguides using alignment cross marks, which were produced together with the ridge waveguides in the waveguiding layer (see Chapter 6 - Mask Design).

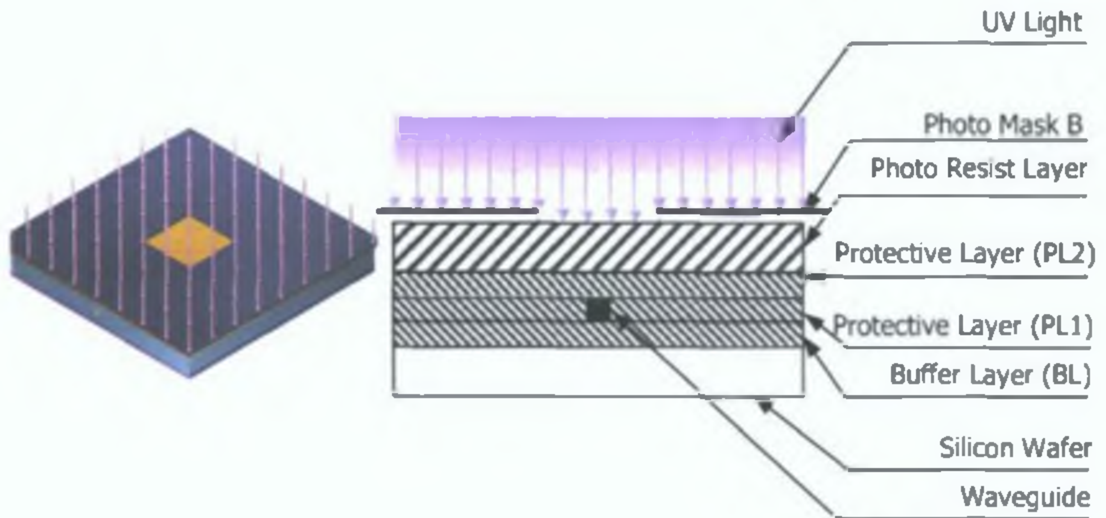

Figure 5-10. Photoresist UV-exposure

In the photoresist development stage the processed wafer was cured with a developer. Since the photoresist was positive, the UV exposed part was washed away and chamber pattern appears.

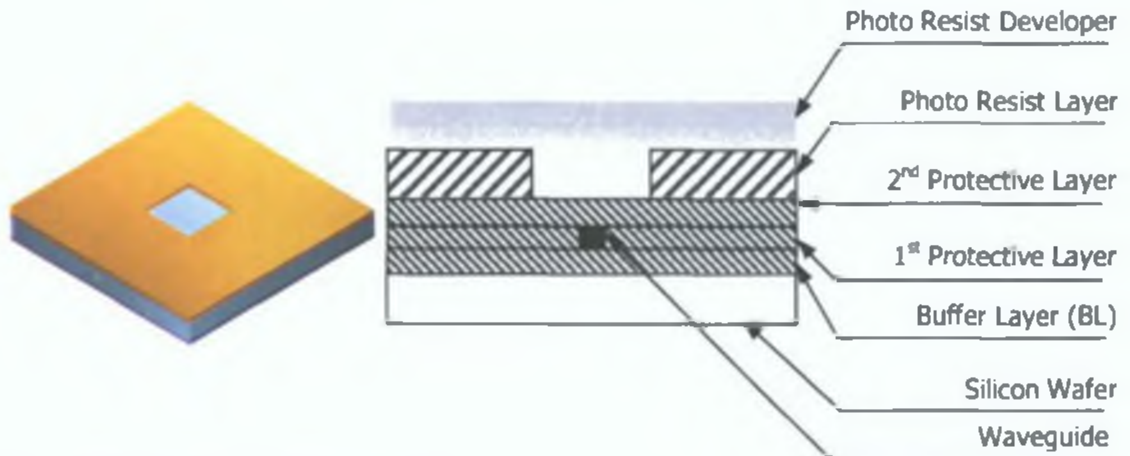

Figure 5-11. Photoresist developing

The prepared wafer was then placed into the plasma-etching chamber and exposed to plasma as described in the following chapters. Sol-gel layers, which were not protected by photoresist, were etched down until the wafer surface was reached.

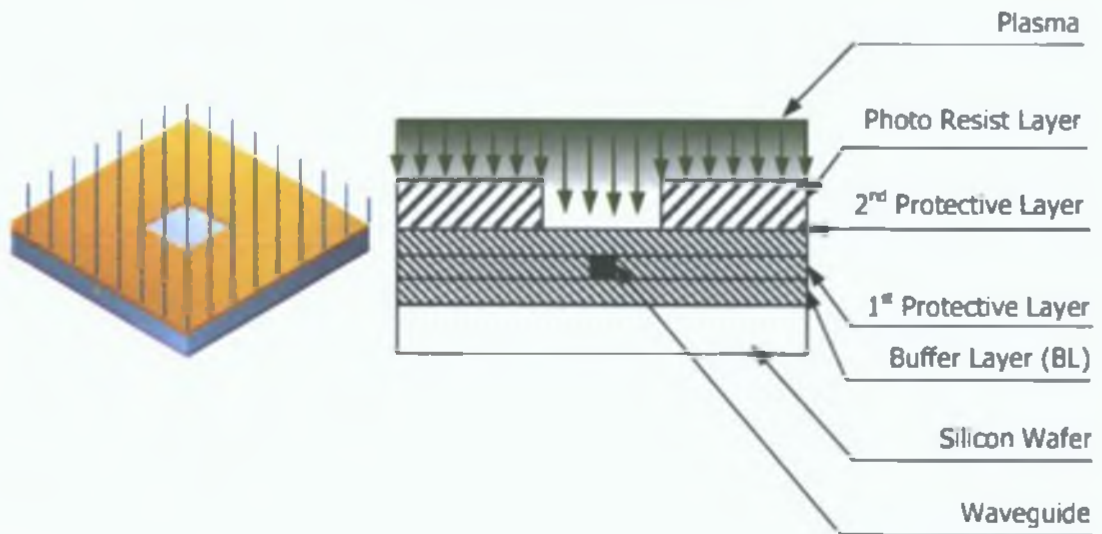

Figure 5-12. Plasma etching

After etching, the photoresist was then stripped off using photoresist stripper, which completed the wafer processing (Figure 5-13).

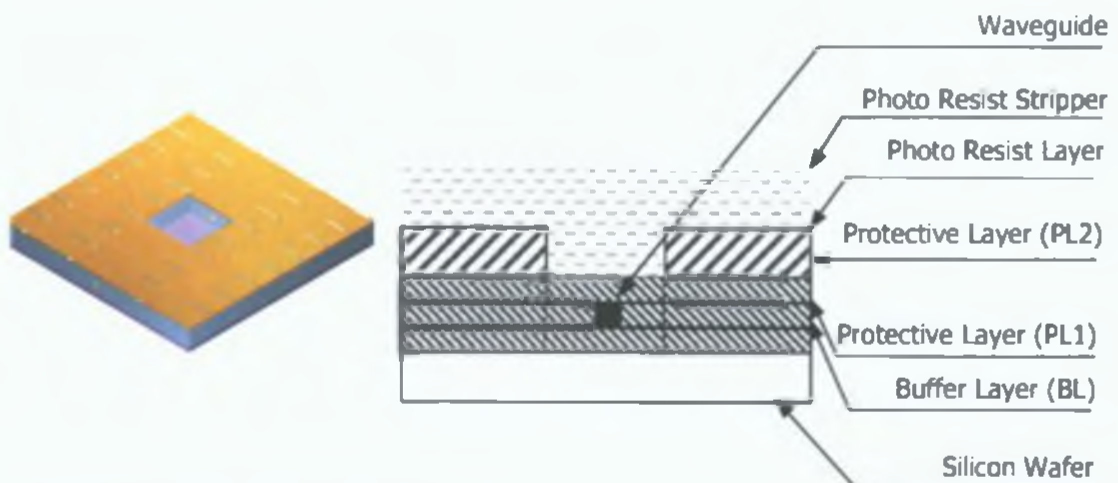

Figure 5-13. Stripping off photoresist

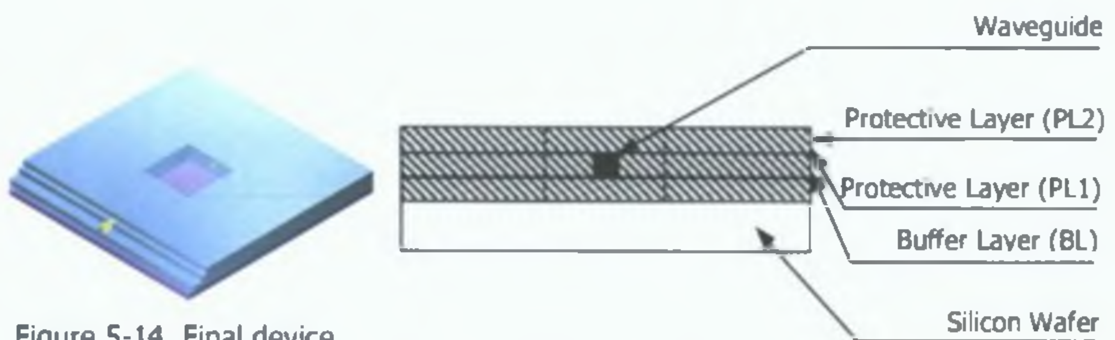

Figure 5-14. Final device

Finally the device was extracted from the silicon wafer by cleaving the wafer along the crystallographic planes allowing smooth coupling regions to be obtained. The AutoCAD final LTM model is presented in Figure 5-15.

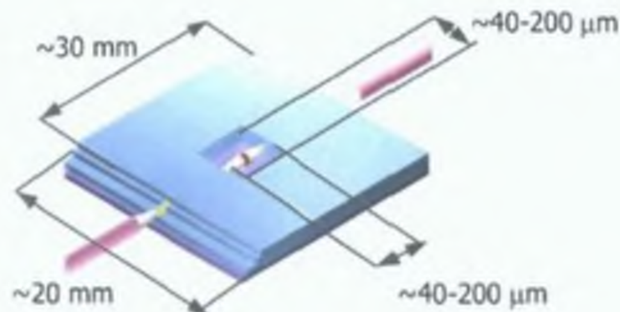

Figure 5-15. The final 3D model of the LTM device

5.3. Conclusion

The chapter summarises the requirements, which underpin the system fabrication steps and system design. The presented process does not cover exact details and timings of each single fabrication step, however these can be found in Appendix.

The final remark on the LTM fabrication process from the commercialisation point of view would be that optical fibre pigtailing and packaging should be considered in order to provide a complete device to the final customer. The cleaving technique should be replaced by a more accurate technique for the separation of the devices, such as dicing and polishing (Figure 5-15).

However given that the major objective of this work was a proof of the LTM concept, the presented fabrication was confirmed to be an appropriate choice for the prototype device.

6. Mask Design

6.1. Introduction

For the purpose of the manufacturing process two photolithography masks were designed. The designs were drawn using C2V Prometheus software conforming to all current mask design conventions [88] and prepared to cover a 4-inch wafer with the patterns shown in Figure 6-1 and Figure 6-2.

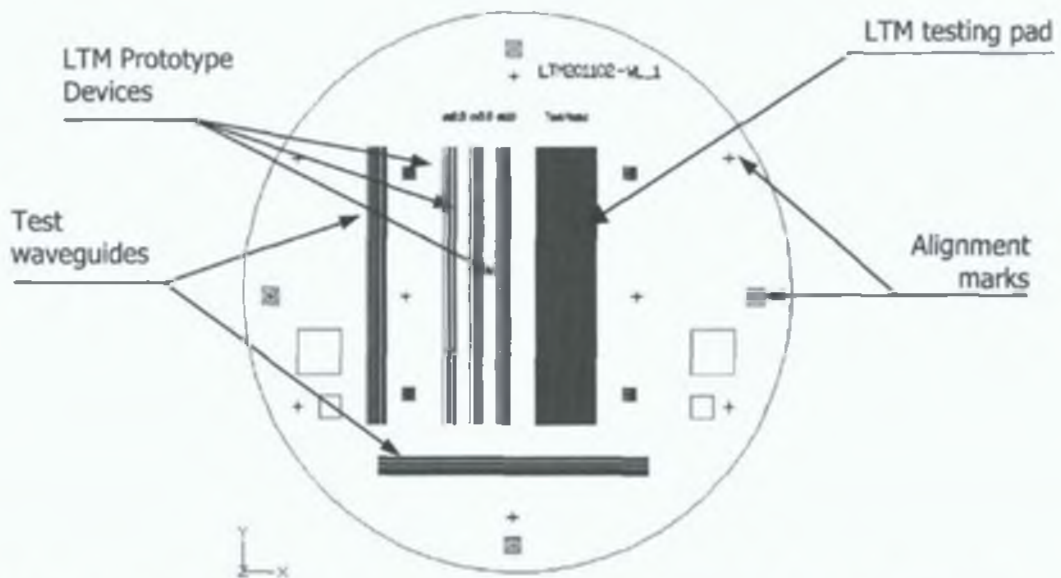

Figure 6-1. LTM photolithography mask A (design for creating ridge waveguides)

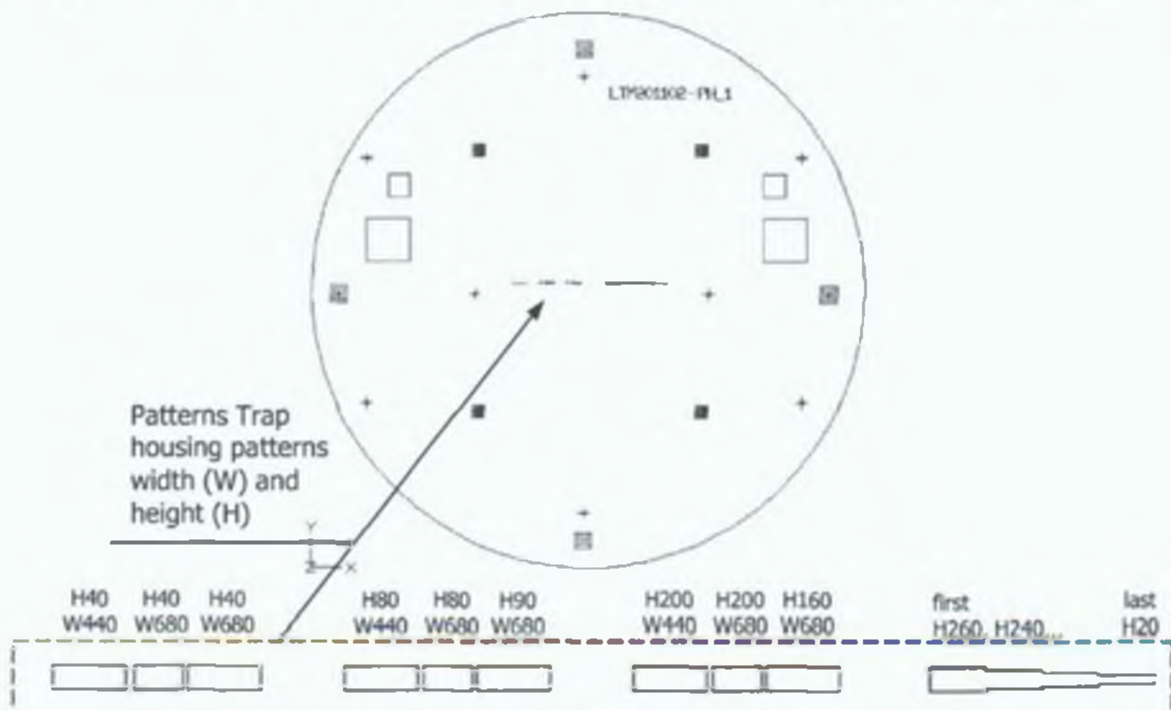

Figure 6-2. LTM photolithography mask B (design for the trap housing)

6.2. Mask Details

As indicated in Figure 6-1 and 6-2, alignment marks were incorporated in order to allow the exact superimposition of pattern elements during processing Final chromium masks were produced (Compugraphics Ltd) using state-of-the art technology, allowing high grid positioning accuracy In addition, all crucial LTM elements were placed in the centre of the wafer in order to avoid thickness fluctuations that tend to be higher near the edge of the wafer when the spincoating process is used Three different elements were processed using the two masks to produce fully functional testing prototypes of the laser trapping device

A series of straight openings of varying width (2x100 µm, 2x50 µm, 2x7 µm, 2x6 µm, 2x5 µm, 2x4 µm, 2x3 µm) was placed horizontally and vertically on the border of the mask (Figure 6-1) Through the photolithography process these openings form test ridge waveguides in the sol-gel Guiding Layer These features permit the testing of waveguide quality and optical losses by comparing the light intensities emitted from longer and shorter cut samples (see Chapter 9)

A further feature on the masks is the LTM testing pad It consists of straight openings placed on mask A, forming groups of different widths (2x6 µm, 2x5 µm, 2x4 µm, 2x3 µm, 2x2 µm) (Figure 6-3a) This pattern is transformed to the Guiding Layer to create ridge waveguides A second feature of the LTM testing pad is located on mask B and consists of a tapered rectangular opening with height ranging between 260 µm and 20 µm (Figure 6-3b) This shape is then transferred first to the photoresist and then to all sol-gel layers with the reactive ion etching exactly above the groups of straight waveguides On the wafer these two patterns overlap forming the LTM device for testing various combinations of two basic LTM parameters such as waveguide endface separation and waveguide size (Figure 6-4)

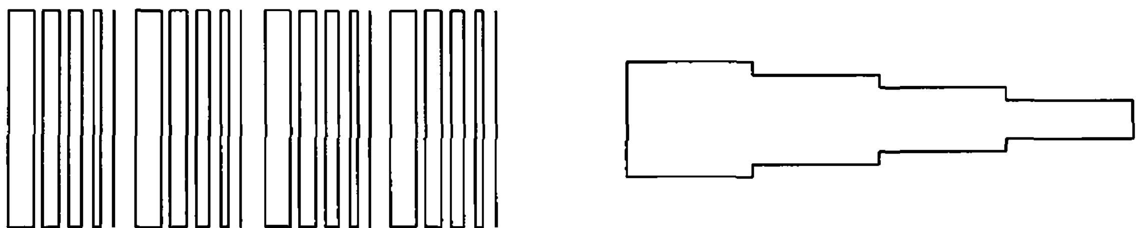

Figure 6-3 LTM testing pad components a) Waveguides pattern on Mask A b) Trap housing on Mask B

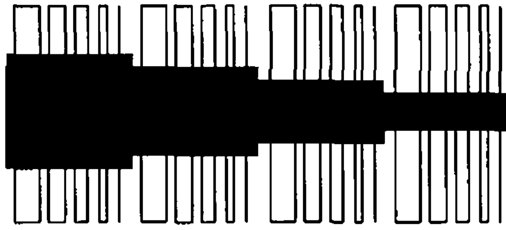

Figure 6-4 Final LTM testing pad

The final LTM device also comprises of two patterns placed on masks A and B, the dimensions of which are selected following the recommendations presented in Chapter 3 for each particle size separately The groups of separated openings of identical widths on mask A form, through the photolithography process, ridge waveguide structures in the Guiding Layer (Figure 6-5a) These groups are subsequently etched through the middle as indicated by the pattern on mask B (Figure 6-5b) The LTM devices formed in this way form three separate groups for each particle size, with each group containing the three optimal combinations of the LTM dimensions (see Chapter 3 and Figure 6-6)

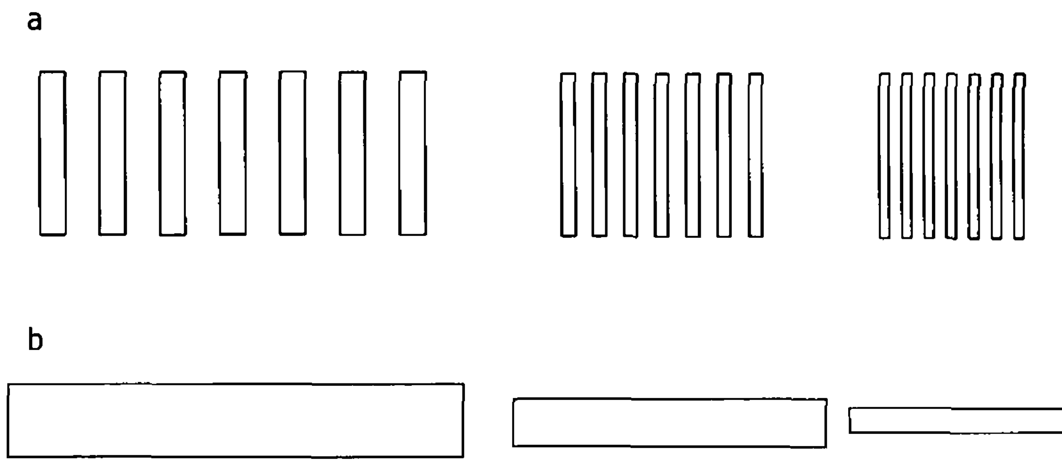

Figure 6-5 LTM device components for certain object sizes a) Waveguides pattern on Mask A b) Trap housing on Mask B

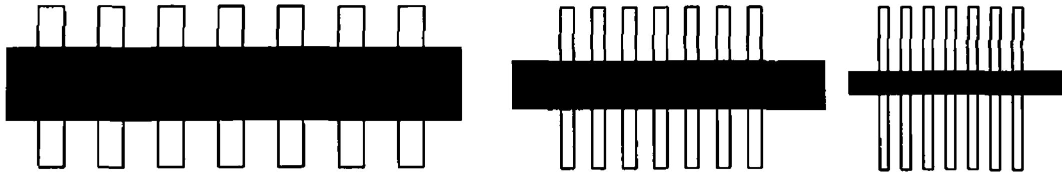

Figure 6-6 LTM prototype devices each containing multiple identical waveguides

6.3. Conclusion

In conclusion, two photolithography masks were designed to match the device specification, and to permit exact positioning of the mask features contained in the LTM

7. Photolithography Process Optimisation

7.1. Introduction

Optical lithography (photolithography) is the process used to transfer patterns from the mask to a layer of photosensitive film deposited on the surface of the wafer and it is currently one of the most important technologies used in sol-gel integrated device manufacturing [89,90] The basic system includes a light source, which illuminates the sample through the openings in the mask (with an imprinted negative pattern of the final features) The light, which passes through the mask, interacts with the photosensitive material causing its polymerisation For the photopatternable sol-gels after chemical treatment the exposed part of the desired pattern remains on the substrate [91]

At present, the majority of market available photolithographic systems are designed in three different configurations presented below

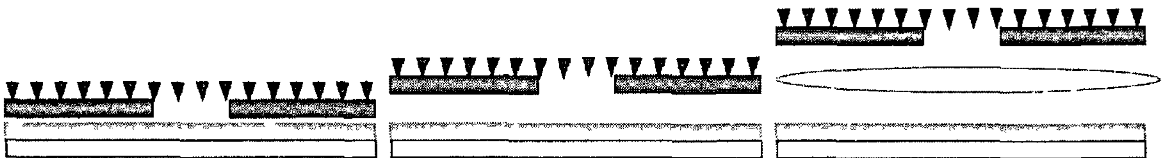

Figure 7-1 Photolithographic systems configurations (from the left contact, proximity, projection)

In contact mode the mask is placed in direct contact with the exposed film This relatively inexpensive method provides relatively high resolution (R) derived from Fresnel (near field) diffraction theory and is given by the formula [92]

$$R \mid k[\lambda(s \quad 0\,5d)]^{1/2} \qquad \textit{Equation 7-1}$$

where

λ - exposure system light wavelength

s - separation gap between mask and film

d - film thickness

k - constant that depends on the photoresist and the development procedures (typically k=3)

Using the above equation, contact mode systems of this kind achieve resolution of around 1.6 µm, which is similar to the resolution provided in the specification of SUSS MA56 (R | 1 2 µm for PMMA material) used for the LTM fabrication.

In reality, the Modulation Transfer Function (MTF) is a better approximation of the photolithographic system capability because it not only provides information about the resolution but also about the sharpness of the optical exposure [91]. MTF, also known as optical contrast is given by the formula:

$$MTF = \frac{I_{max} - I_{min}}{I_{max} + I_{min}}$$ Equation 7-2

where I_{max} and I_{min} are the local maximum and minimum intensities emerging from the mask.

The reason for using MTF is that it is possible to achieve high resolution but a poor contrast, and vice versa. An ideal situation is when resolution and contrast go hand-in-hand. For practical reasons (since the MTF is an experimental measure), it was decided that information provided by the theoretical resolution is sufficient for the LTM optical path fabrication.

Contact mode has advantages of simplicity and good resolution, but it has also some disadvantages, the most important being fast degradation of the mask (pinholes, scratches etc.), as well as the imaging of all particles and dirt directly onto the wafer and the mask.

The second type of system operates in proximity mode, which, in principle, is similar to contact mode, but in this case the mask and the film are separated from each other by a certain distance (s ! 0) called the "separation distance". As it might be expected in this configuration mask damage is reduced. As stated by Equation 7-1, resolution drops significantly compared to contact mode to over 2 µm.

Finally, in projection mode the mask pattern is projected onto the film through a system of lenses, creating a smaller version of the image The resolution of these systems is very high, varying around 0 07 µm The lack of contact between the mask and the wafer results in almost no mask wear (high production compatible) and mask defects or contamination on the mask are reduced in size on the wafer The major disadvantages of these types of systems however are their high cost and additional problems with Fraunhofer diffraction resulting in accuracy variations in the final pattern

All three options bring certain benefits but there is little doubt that projection systems provide superior resolution and quality of all the systems presented Considering however the available equipment, switching cost, and resolution required, the contact mode method seemed to be the best choice for the LTM waveguides fabrication The instrumentation available for this work is a SUSS MA56 Mask Aligner that can operate both in contact and proximity mode In order to utilise the full capabilities of this system it was operated in contact mode configuration This enabled high quality fabrication of 4 µm features and assured good repeatability across 4-inch wafers The following factors were identified as important to the photolithography process

- Equipment and the lithography system setup including illumination optics and system configuration, wavelength of the light used in the process and its intensity distribution pattern, uniformity of the light power used for exposure, separation distance between the mask and material

- The parameters of the process baking time of the sample between spincoating and exposure (defined as prebaking time), material layer thickness and uniformity

- Material properties photoinitiator concentration and compatibility of the photoinitiator with the exposure system

Optimisation focused mainly on parameters that were relatively easy to control during the fabrication process For that reason parameters related to the equipment setup and process were chosen Development of the material properties was beyond the scope of

this work, as it required greater expertise in chemical science and significant development time.

7.2. Light intensity Distribution

As can be seen from Equation 7-1, diffraction theory predicts the limits of the resolution of the lithographic system to the wavelength of light used for illumination. The lower the wavelength the lower the influence of the exposure gap and the better overall resolution.

The initial intensity spectrum of the mask aligner (SUSS MA56) is presented in Figure 7-2. The pattern is spread over wide range of wavelengths including the region of interest of 350 – 500 nm. In order to improve the resolution, an optical filter was installed between the halogen lamp and the exposure system cutting off all wavelengths in the region of interest except 365 nm. The wavelength spectrum obtained after the procedure (Figure 7-2) revealed the presence of a single intensity peak around 365 nm, which had a positive influence on the system resolution capabilities.

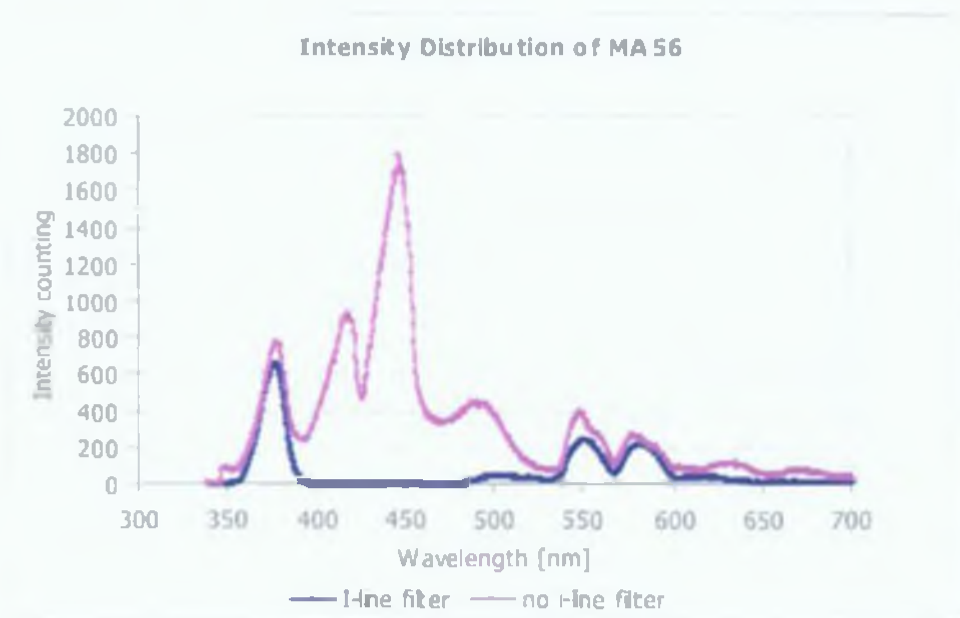

Figure 7-2. Intensity distribution versus wavelength

7.3. Exposure Dose Uniformity

The intensity spatial uniformity of the exposure system is an important factor, which guarantees repeatability of quality across the substrate The spatial intensity variation parameter is defined as

$$\gamma = \frac{I_{max} - I_{min}}{I_{max} + I_{min}} \times 100 \qquad \textit{Equation 7-3}$$

where I_{max} and I_{min} are the maximum and minimum intensities measured across the 4-inch wafer being exposed

Using this formula the uniformity was calculated to be 1 9% with an i-line filter as compared to 3 5% with no filter installed Since the quality of the final features is directly related to the exposure dose of the light given by

$$D = I \times t \qquad \textit{Equation 7-4}$$

where

I - intensity of the light coming from the illumination system

t - exposure time

Therefore, the decrease in the intensity variation parameter directly improves quality of the features across the 4-inch wafer

7.4. Illumination Optics

The illumination optics design also influences the overall resolution of the contact and proximity mode systems Since we had little control over the optical configuration no changes were made to this part of the system However it is worth noting that the SUSS MA56 was equipped with a diffraction reduction system that slightly improved its resolution capabilities (Figure 7-3)

Figure 7-3 Optimised optical exposure system of SUSS M56 mask aligner

7.5. Separation Distance Between the Mask and Material

Another parameter that affects lithographic resolution is the distance between the mask and exposed film

The proximity system's Fresnel (near field) diffraction effect is proportional to the square root of the wavelength and exposure gap between the mask and film The ideal situation occurs when the mask is in close contact with the film

In real systems various types of nonuniformities of film thickness across wafers (especially at the edges) prevent this separation distance from being equal to zero Due to the physical contact the mask can be easily damaged and accumulates various kinds of defects In our system, in order to obtain the best possible resolution, contact mode was utilised and particular attention was paid to the reduction of edge effects arising from the spincoating process (as presented in Chapter 4)

7.6. Sample Baking Time and Temperature Before Exposure

As presented in Chapter 5, the prebaking fabrication step occurs right after spinning the film to the substrate This involves placing the substrate with the deposited film on the hot-plate for a specific time and temperature to obtain a film with the desired properties before the UV-exposure takes place This part of the process is of particular importance to ensure the quality of the optical waveguides that can be produced using sol-gel and contact photolithography technologies The main factors influenced by the time and the temperature of the prebaking process include

- Material resistance to mechanical contact with the mask
- Variation of the material refractive index

- Changes in the molar absorptivity of the material

The material resistance to mechanical contact is directly related to the situation where the mask touches the material surface before exposure If the material were in a liquid or semi-liquid state then the physical contact with the mask could influence the uniformity of the coating and thus as described previously the quality of the final LTM feature The reduction of the damage imposed on the mask by the material was also considered This implied that the prebaking time and temperature had to be adjusted to provide enough mechanical resistance to the layer, but still leaving the photopolymerisation properties of the material intact

The small refractive index difference between buffer, protective layers and guiding layer and thus the refractive index reproducibility was another factor that influenced the selection of the optimised prebaking conditions Based on the findings presented by Coudray et al [89], a baking temperature of 120°C was selected to minimise the refractive index variation to the lowest possible level

The absorption in the photopatternable sol-gel material is a measure of its sensitivity to the UV exposure This sensitivity can be modified both by changing the concentration of the photoititiator as well as the prebaking time In order to reduce the influence of the process conditions (variations in prebaking time, environmental temperature and time between pre baking and exposure) on the sensitivity of the material, the prebaking time was selected based on the absorptivity curve, which was obtained experimentally (Figure 7-4)

The measured samples included glass slides coated with the LTM sol-gel matenal The absorption spectrum was measured using a UV-vis spectrometer (type) The data revealed that the absorption of the material decreases as prebaking time increases and reaches a saturation level after 35 min For descriptive purposes the absorptivity curve was subdivided into three distinctive phases as the material changed photopatterning properties

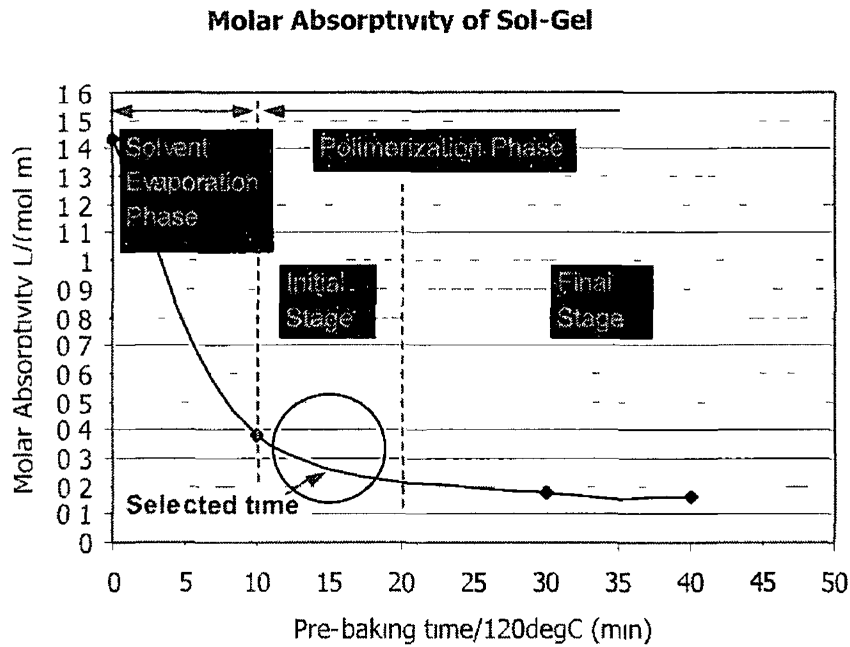

Figure 7-4 Molar absorptivity curve of the sol-gel (experimental result)

The first phase is the solvent evaporation and material densification where a significant drop in absorptivity (and thus energy level required to trigger polymerimerisation) occurred After 10 min the absorptivity level tends to stabilise As baking time passes 20 min the etching properties decrease and the material transforms thereby making fine etching of the waveguides difficult Furthermore, baking over 40 min gave waveguides where etching was impossible with standard solvent (isopropanol)

The adjustment of the prebaking time was optimised by identifying the region of the absorption curve (Figure 7-4), which showed a relatively low gradient of the absorption with time This region, which does not compromise the photopatternable properties of the material led to the selection of a prebaking condition of 15 min at 120ºC for the final device fabrication

7.7. Conclusion

For the purpose of LTM optical waveguide fabrication the photolithography technology in contact mode was optimised and used for the LTM fabrication.

Together with adjusted material properties and the fabrication process it allowed fabrication of fine quality ridge waveguides (Figure 7-5) sufficient to meet the LTM design requirements.

Figure 7-5. Ridge waveguides fabricated using sol-gel and photolithography technology

Although contact mode photolithography utilises a high modulation transfer function, rapid wear on the mask reduces its application to laboratories and small-scale production lines. Thus for the full commercial application of the LTM device it would be recommended to use projection photolithography which allows to achieve resolution of the contact mode which at the same time reducing the damaging effect of the mask on the wafer and wear on mask itself.

8. Trap Housing Fabrication (Reactive Ion Etching)

8.1. Introduction

Reactive Ion Etching used in the fabrication of the LTM trap housing is a relatively new technology This technology dates back to the seventies when the first experiments on etching were reported, and has been developed over the years to become the most popular and widespread technology for integrated circuit fabrication It emerged from mainstream etching methods and was qualified as a dry method due to its principles of operation (Figure 8-1) [93,94]

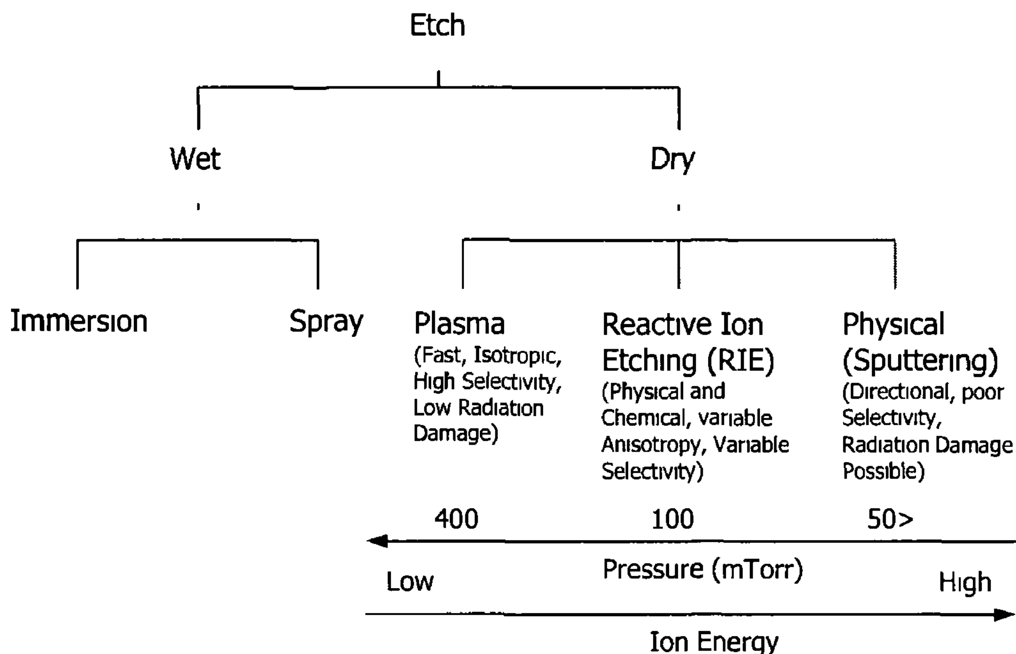

Figure 8-1 Typical material etching techniques

In general, dry etching is a process that utilises gases and high voltage energy to create a partially ionised gas called a plasma, which is able to chemically react with certain materials The plasma is composed of free electrons, which are generated through high kinetic energy collisions between neutral atoms With sufficient voltage, which increases the kinetic energy of the electrons, the gas becomes filled with positive and negative particles throughout its volume i e it becomes ionised The applied electric field can be either constant (DC Glow Discharge) or can vary in time

(RF Glow Discharge) The major disadvantage of DC Glow Discharge systems is that they are restricted to etching only conductive materials due to the accumulation of positive charge on a dielectric, which prevents the gas from sustaining the plasma state

Since all materials used in the LTM system are dielectrics, this type of system could not be successfully applied In the AC Discharge configuration the positive ion bombardment effect during the first half of the AC cycle is entirely neutralised by electron bombardment during the next half of the cycle In order to prevent dielectric surface ionisation, the AC frequency has to be high enough so that the half period is shorter than the charge-up period of the dielectric This requires a frequency of over 100 kHz (RF frequencies), typically 13 56 MHz At these frequencies the free electrons are able to follow the variations of the applied electric field and, unless they suffer a collision, they can gain energy of the order of a hundred of eVs On the other hand, the energy of positive ions (much heavier than electrons) is almost not influenced and their small energy (~0 01 eV) comes mainly from the thermal energy of the environment

A typical capacitively-coupled RF plasma etcher used in RIE mode consists of a chamber, vacuum system, gas supply and a RF frequency power generator as shown in Figure 8-2

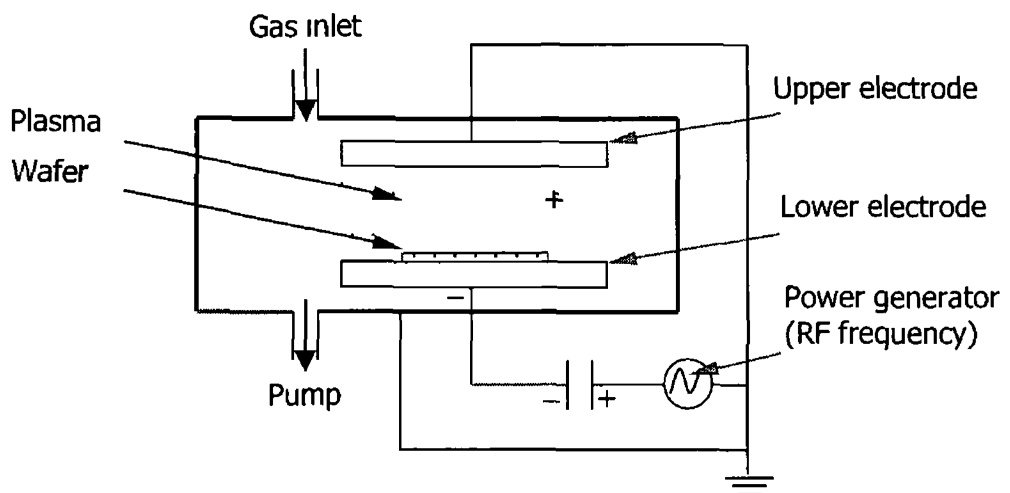

Figure 8-2 Typical plasma reactor in Reactive Ion Etching mode

The process starts with placing the wafer covered with a substrate on the lower electrode and establishing a vacuum. The proper mixture of gases is released into the chamber and power applied to the lower and upper electrodes creating a radio frequency (RF) electric field between electrodes, which energises the gas mixture to the plasma state. During the first few cycles of the applied voltage, electrons generated in the plasma escape to the electrode and charge the capacitor negatively, separating the power source from the lower electrode. In this way the negative DC bias voltage is formed on the electrode and the AC voltage becomes superposed on this negative DC voltage as shown in Figure 8-3

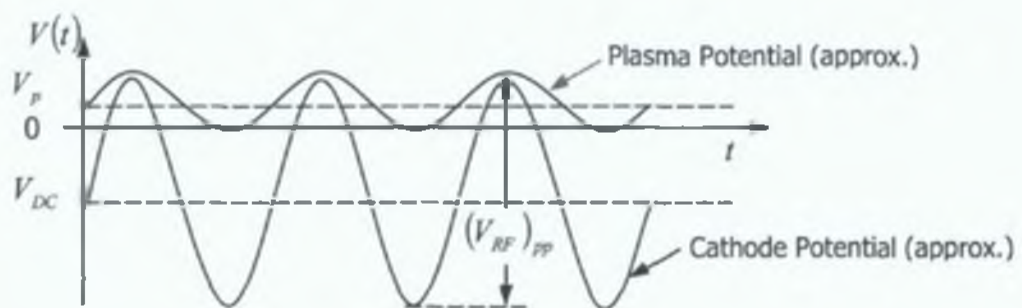

Figure 8-3. Plasma and RF potential fluctuations

In the pressure range of a few mTorr to a few hundreds of mTorr, the electrons travel much longer distances than the ions. The result is a higher rate of collision of electrons with the reactor walls than in the case of positive ions, which leads to a high discrepancy between number of electrons and the number of ions observed near the walls (Figure 8-4).

The difference in concentration of counter charged particles has a significant impact on potential profile, which is positive within the plasma ($\rho \quad e(n_i \quad n_e)$ >0, ~10 V) but falls sharply to 0 near the walls. The electrostatic field between the plasma and the wall induced by the potential acts as a confining potential ("valley" for electrons and "hill" for ions). This implies that the force acting on the electrons is directed into the plasma slowing down their movement and alternatively accelerating ions towards the wall. Potential wells in the vicinity of the walls are called dark-sheets and reduce the electrons capability to escape from the plasma cloud, therefore helping the plasma to keep its quasineutral state.

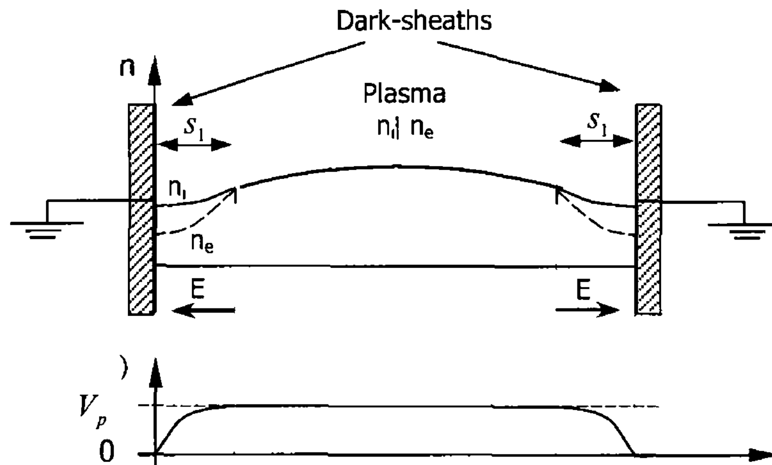

Figure 8-4 Formation of dark sheaths

The effect of dark-sheet formation can be observed in front of both electrodes In this case, however, the presence of the capacitor between the RF power generator and the cathode (lower electrode in RIE mode) makes the voltage distribution asymmetric, increasing the potential difference between the plasma and cathode by the average of the applied RF electric field (Figure 8-5)

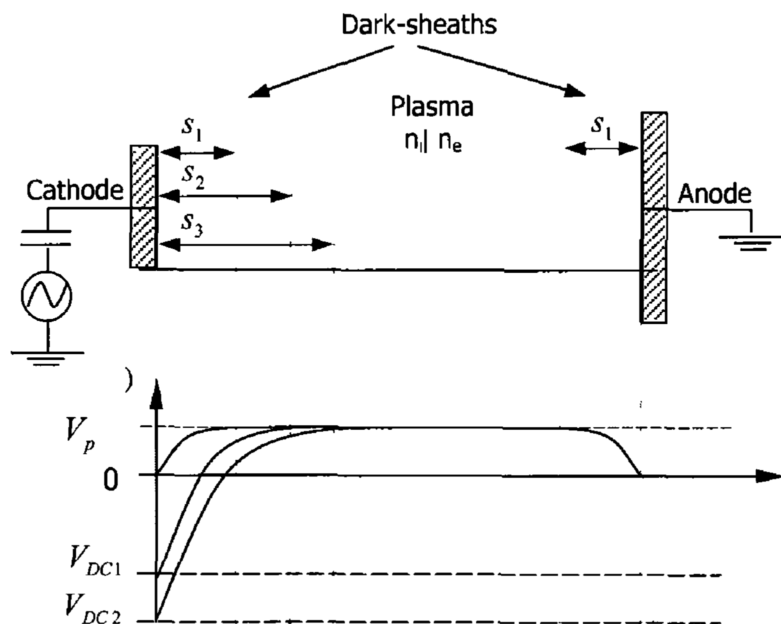

Figure 8-5 Dark sheaths in the vicinity of the electrodes

The increased electric field results in additional energetic (physical) ion bombardment of the surface, which improves the chemical reaction between the material and the

reactive plasma species. This particular combination of chemical and physical dry plasma etching is known as Reactive Ion Etching.

Once established, the plasma becomes on extremely volatile environment involving various kinds of physical and chemical processes. Its characteristic depends on many parameters such as reactive gas type and mixture with other gases, chamber pressure, applied power, reactor design etc. The most typical internal plasma reactions include: dissociation, ionisation, dissociative ionisation, excitation and recombination (Table 8-1 presents examples of these reactions for CF_4 based plasmas). As a result of these reactions multiple new species are produced of which only a few are responsible for the etching properties of plasmas [93,95].

Basic reactions in CF4 plasma	
Dissociation, Radical Formation	$CF_4 + e^-$ o $CF_3 + F + e^-$
Ionisation	$CF_3 + e^-$ o $CF_3^+ + 2e^-$
Dissociative ionization	$CF_4 + e^-$ o $CF_3^+ + F + 2e^-$
Excitation	$CF_4 + e^-$ o $CF_4^* + e^-$
Recombination	$CF_3^+ + F + e^-$ o CF_4; $F + F$ o $2F$

Table 8-1. Typical reactions in plasma reactor for CF4 based plasma

Depending on the character of these species and the extent of their contribution the dry etching mechanisms fall into one of four basic categories:

- Sputtering

  In this type of reaction, particles (usually positive ions created through ionisation and dissociative ionisation) impact the etched surface. If their energy is high enough atoms, molecules or ions are ejected from the surface. Since sputtering is a purely physical mechanism, it requires a large amount of energy and produces etching profiles that are highly vertical. It is also much less selective than other types of reactions and all materials can be sputtered at about the same rate. Physical sputtering can also cause damage to the surface where the extent and amount of damage is a direct function of the ion energy delivered.

- Chemical Etching

For chemical etching a suitable gas mixture is introduced to the chamber to produce reactive species by molecular dissociation into radicals and excitation of neutrals During chemical etching the following steps can be identified (Figure 8-6)

- formation of the reactive particle
- diffusion of the reactive particle to the surface to be etched
- adsorption of the reactive particle at the surface to be etched
- chemisorption of the reactive particle at the surface, i e a chemical bond is formed
- desorption of the product molecule
- diffusion of the product molecule into bulk gas

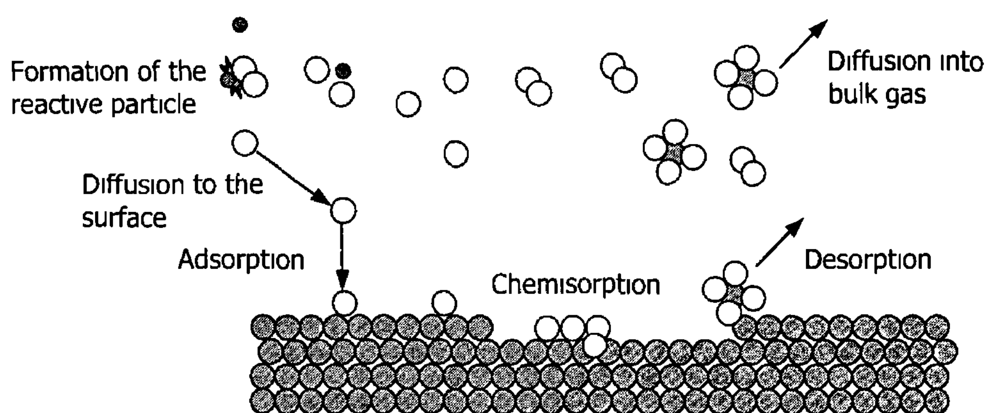

Figure 8-6 Reactions observed during the chemical etching of a material

By its nature chemical etching is very selective and very isotropic and can cause serious problems such as edge undercutting The best results for this type of processing can be achieved when the proper gas mixture is chosen, i e reactive species are able to remove molecules from the surface of the film

- Ion-enhanced etching

This process is the result of the combined effect of chemical etching and sputtering Synergy of both mechanisms working together results in an increased etch rate of the films because impacting ions damage the surface of the film and

this leaves it vulnerable to reactive species as they can penetrate the etched material deeper and more efficiently Reactive Ion Etching is an example of this type of etching

- Inhibitor ion-enhanced etching

  In this type of mechanism the discharge supplies etchants, energetic ions and inhibitor precursor molecules that adsorb or deposit on the substrate to form a protective layer or polymer film, i e it involves the use of an inhibitor species In the absence of either ion bombardment or the inhibitor, the etchant produces a high chemical etch rate of the substrate If properly controlled, the process can provide anisotropic features over very large etch depth

Figure 8-7 depicts all of the above etching processes and their contribution to the final shape of the etched features It also shows that the ideal dry etching process is difficult to develop and several factors like mask erosion, anisotropy (undercutting), trenching etc have to be considered while selecting the dry etching mechanism in order to meet the final design requirements [96]

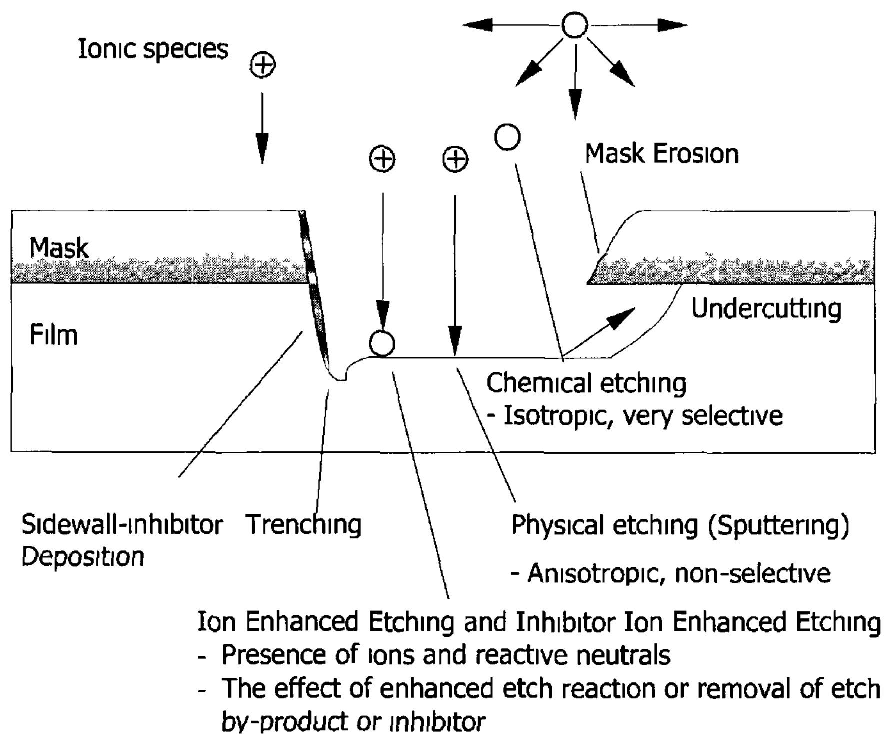

Figure 8-7 Typical reactions between the plasma and the material

Dry etching was a natural choice for LTM manufacturing since it possesses many advantages compared to wet etching, which make it a much better choice for fabrication of small high quality features These are

- No requirement for rinse and dry steps as in the case of wet etching
- No need for toxic and hazardous chemicals
- Failure in adhesion between resist and wafer does not cause serious edge undercutting
- Dry etching is less anisotropic and is capable of etching small structures < 3 pm i e compared to wet etching dry etching leaves vertical sidewalls of the etched layers, while avoiding undercutting of the material under the photoresist (Figure 8-8)

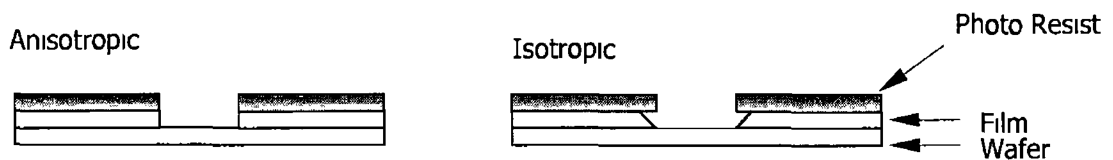

Figure 8-8 Isotropic and anisotropic etch

For the LTM application Reactive Ion Etching has outstanding characteristics, superior to other dry etching methods Ion Milling, despite very good anisotropic properties has poor selectivity and samples are exposed to high radiation created by ionisation mechanisms, which could have influenced the initial refractive index of the waveguides For chemical etching even though the selectivity is substantially improved, due to the chemical nature of the process [97,98], the etching rate of the sol-gels was expected to be poor, which was our main concern as the thickness of the etched film was 15 µm

These arguments and the available equipment supported the selection of RIE mode for LTM trap housing fabrication and thus optimisation of the plasma conditions took place in the parameter range suitable for this type of etching

8.2. Reactive Ion Etching Process Optimisation

Experiments with RIE were carried out to investigate the influence of the plasma etching process parameters and to evaluate whether an optimised combination of these parameters will allow the LTM trapping chamber to meet the design specifications.

Following the initial design assumptions, the RIE process had to be optimised to accurately etch features of a minimum width of 20 μm with a depth of 15 μm. A verticality of the etch sidewalls below 10θ and overall process repeatability also had to be assured.

An Oxford Instruments Plasmalab 80Plus capacitively coupled reactive ion etcher was used during the entire testing and manufacturing process. The etching procedure was optimised for this particular machine. The results may vary for other types of plasma etchers, materials used, and types of wafer as well as wafer coating procedures.

The existence of the SiO_2 sol-gel component influenced the selection of a fluorine-based plasma as the primary chemistry for the etching due to the previously reported excellent properties of SF_6 plasmas on the quality and efficiency of etching [99-101]. Most of these studies were focused on optimising gas mixtures for etching SiO_2 or pure silicon rather than deep etching of organic-inorganic composites. It can be argued that the widely known BOSH process [102-104] could be more efficient than the typical reactive ion etching. However, currently more laboratories are equipped with less expensive RIE tools, which makes the presented process interesting.

8.2.1. Samples Preparation

In order to ensure repeatability of the results, each sample was processed in an identical manner and under identical conditions. Standard 4-inch (100mm) silicon wafers with a thickness of approximately 450 μm formed the substrate for the sample. The sol-gel layer was spincoated on top, creating a layer with a refractive index value of 1.4963 and nominal thickness of 5 μm, followed by prebaking at 120 θC. The sample was then exposed in contact mode for 210 s to UV light and further baked at 120 θC

for 1 hour For UV exposure a SUSS MA56 mask aligner was used, which delivered 10W/cm^2 of optical power at a wavelength of 365 nm The procedure was repeated 3 times in order to obtain a 15 μm thick film The sample was then covered with a 12 μm film of SPR-220 7 0 positive photoresist [105] (the same that is used in the LTM fabrication), UV-exposed and rinsed with solvent to create openings through which the plasma could interact with the sol-gel surface (Figure 8-9) Finally, the photoresist was additionally hardened by baking in an oven for 30 min at 90 ºC

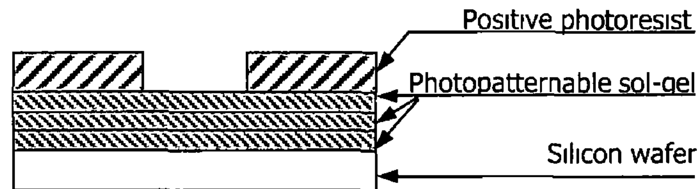

Figure 8-9 RIE experimental sample

8 2 2 Sample Characterisation

There are several parameters used to investigate quality and efficiency of the etching process This number was however reduced to the parameters, which would have the most significant impact on quality and efficiency of the LTM performance These major parameters are photopatternable sol-gel etch rate, selectivity, etch anisotropy and etch bias These are defined as follows

- Etch rate of the film

  Etch rate (ER) is a measure of how fast the material is etched and it provides information about the efficiency of the plasma process It is typically expressed in nm/min

- Selectivity

Selectivity is the ratio of etch rates between two films (in our case between resist and sol-gel), a parameter developed for the optimisation of the thickness of the photo resist films

$$S \quad \frac{ER_{sg}}{Er_{mask}}$$ *Equation 8-1*

The selectivity value ultimately limits the depth of the material that can be etched for the specific process and the masking material used For LTM fabrication and with the maximum achievable thickness of 12 µm for the SPR-220 photoresist achieved by single coating, a selectivity greater than 1 25 is sufficient to etch through all the hybrid sol-gel layers

In addition the selectivity is high, the thickness of the masking material can be reduced and thus better quality features can be produced

- Etch bias

Etch bias (E_b) is designed to measure the change in linewidth due to anisotropic properties of the thin films It is defined as a difference between original linewidth (W_b) and final linewidth after photoresist removal (W_a) (Equation 8-2, Figure 8-10)

$$E_b \quad W_a \quad W_b$$ *Equation 8-2*

Figure 8-10 Definition of etch bias

Since accurate dimensions of the trapping chamber are of particular importance the etch bias provides information about the difference between the final feature size compared to the dimensions of this feature on the masking material

- Etch anisotropy

Etch anisotropy is defined as

$$A_f \quad 1 \quad \frac{r_{hor}}{r_{ver}}$$ *Equation 8-3*

where r_{hor} and r_{ver} are layer horizontal and vertical etch respectively as shown in Figure 8-11

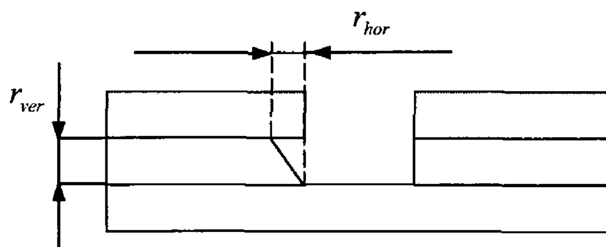

Figure 8-11 Etch anisotropy

When $A_f = 1$ the etching is considered as anisotropic and, as discussed before, it results in smaller divergence of the beam from the waveguide optical propagation axis, resulting in an improvement in the efficiency of the optical trapping

A typical investigation of etching quality involves the use of Scanning Electron Microscopy In this case however the dielectric properties of the sol-gel caused the application of this method to be limited For this reason, all the results were obtained using a Veeco NT1100 White Light Optical Profiling System The vertical measurement range of the instrument in the VSI (Vertical Scanning Interferometry) mode is up to 2 mm and the vertical resolution is 3 nm The system allowed highly accurate measurements of the etch rate as well as evaluation of the quality of etching both in terms of the etch bottom roughness and the verticality of the etch

The measurement procedure involved the sample being scratched using a sharp blade down to the top surface of the silicon wafer This allowed the creation of a stable

reference for sol-gel and photoresist thickness measurement. The sample was then scanned and the data saved. After the sample was etched another scratch was made down to the unetched top surface of the silicon wafer and again measurements were taken to provide both etch rate and selectivity of the process.

The selection of the etching conditions based on etch rate and selectivity as the parameters of critical importance was followed by the measurement of the bottom etch roughness and etch anisotropy.

Optical emission spectroscopy (OES) spectra were taken for each experiment. An Ocean Optics USB2000 Spectrometer was used to determine the plasma characteristics for different powers, pressures and flow rates of gases. The OES spectra wavelength range was between 180-880 nm. For each experiment the data for 10 spectra were averaged.

Based on the previous experience with plasma etching technology and preliminary tests with wafers covered with sol-gel, the following conditions were set as a start point for all investigated etching conditions: RF power = 300 W; SF_6 flow = 80 sccm; O_2 flow = 20 sccm; argon flow = 70 sccm, plasma pressure = 60 mTorr; bottom electrode temperature = 15 °C. Only one parameter was varied at a time for each set of experiments.

8.2.3. Influence of O_2 flow on etching properties

In typical fluorine based plasma for SiO_2 etching, the addition of oxygen increases the amount of fluorine available in the plasma by preventing the recombination of fluorine with sulfur. It is explained by the fact that certain amounts of O_2 react with fluorine species (SF_x) and slow down the SF_x+F recombination process (Equation 8-4).

Equation 8-4

Hence more reactive species are available and the chemical etching is improved and the etching rate increased. The oxygen also provides additional activation energy to the surface, thinning the S_xF_x layer and allowing higher etching rates [106].

The major drawback of the oxygen addition is a reduction in the etch selectivity between the organic photoresist and the silicon based materials when the oxygen reacts with the carbon component of the photoresist organic structure (Equation 8-5).

$$C_xH_yO_z + O_2 \rightarrow CO_a + HO_b$$

The influence of oxygen flow on the etching rate and selectivity of the LTM photopatternable sol-gel is presented in Figure 8-12 and Figure 8-13.

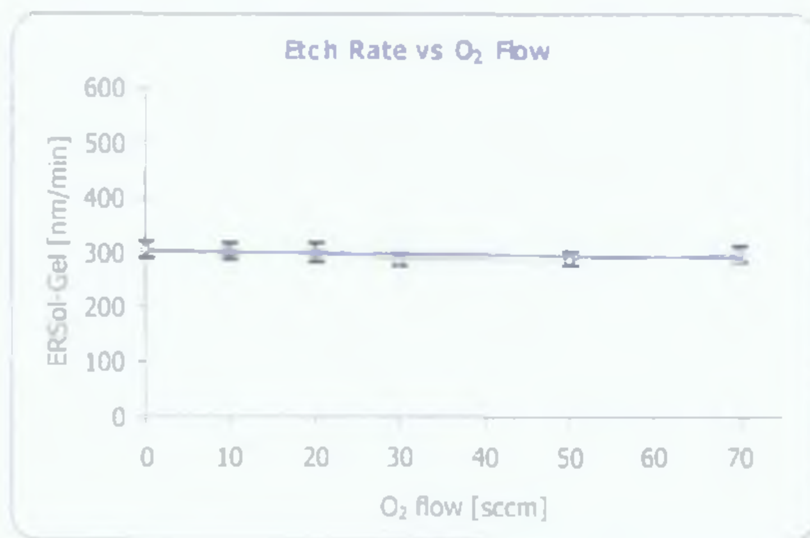

Figure 8-12. Etch rate versus oxygen flow

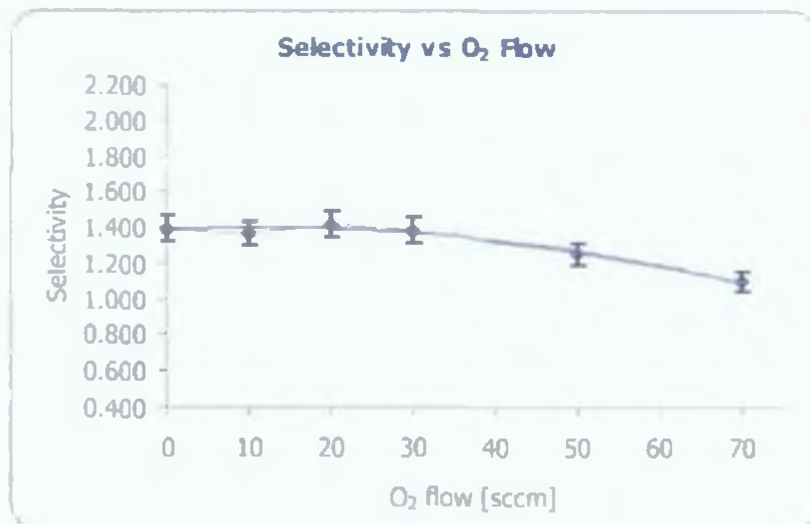

Figure 8-13. Selectivity versus oxygen flow

It can be seen from the graphs that oxygen addition has a small effect on the etching rate and a relatively higher effect on the selectivity of the process The reason for the stable etching rate is probably due to the fact that there is enough oxygen present in the sol-gel itself to sustain a high concentration of the fluorine atoms It is estimated that the photopatternable sol-gel contains approximately 21% oxygen atoms, 43% hydrogen, 31% carbon, 3 8% silicon and a small amount of zirconium A very similar set of atoms could be found in the photoresist with the exception of silicon and zirconium

The high saturation of the fluorine atoms caused by high SF_6 flow (80 sccm) can offer an additional explanation for the flat etching rate curve The presence of the fluorine atoms is so high that the etch rate of the material has reached a maximum and further improvement is not possible The drop in selectivity for higher oxygen flow is caused by the higher etch rate of the photoresist in the high presence of O_2 Oxygen does not have any positive impact on the etch rate of sol-gel and increases the etch rate of the photoresist, which is evident in the drop in selectivity This should be avoided in etching photopatternable sol-gels

8 2 4 Influence of Argon Flow

In order to measure the influence of ambient gas pressure on the etching rate and selectivity, the samples were prepared using standard process and etching conditions

Argon is another gas widely used in combination with fluorine chemistry [107,108] In a typical plasma etch, argon influences the residence time of the gas in the chamber and reduces redeposition of the etchant such as SiF_4 This effect together with the physical sputtering of the material typically improves etching rates and to a lesser extent selectivity

The influence of the argon flow on the etching rate and selectivity of the LTM sol-gel process is presented in Figure 8-14 and Figure 8-15 As mentioned earlier, higher argon flow in the plasma should reduce the residence time of the gas in the chamber, thus reducing fluorine species available for etching and lowering the SiF redeposition

The low response of the etch rate to the argon flow confirms that the plasma environment created is rich with fluorines and additional fluorine atoms do not make a significant contribution to the etching of the sol-gel. The effect of etchant redeposition with the addition of argon is observed on the selectivity graph. The overall good selectivity of the process can be explained by the passivation of the photoresist surface by the fluorines, thus the reduction in redeposition of etchant has a negative affect on the selectivity.

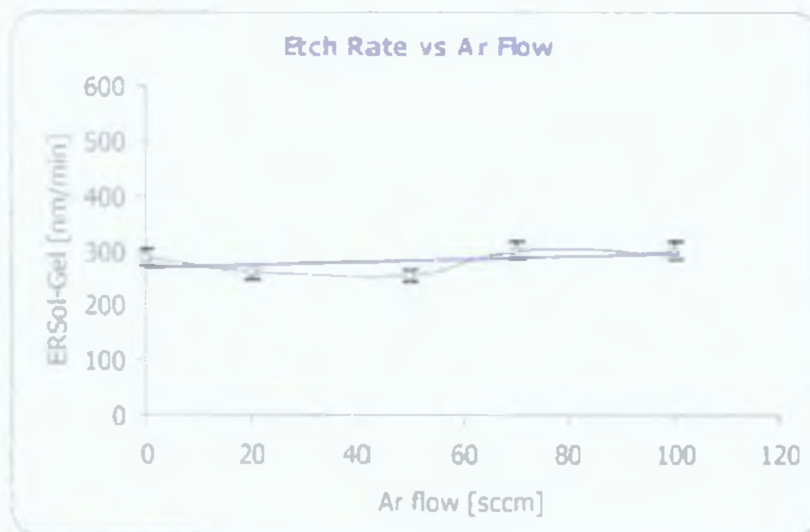

Figure 8-14. Process etch rate versus argon flow

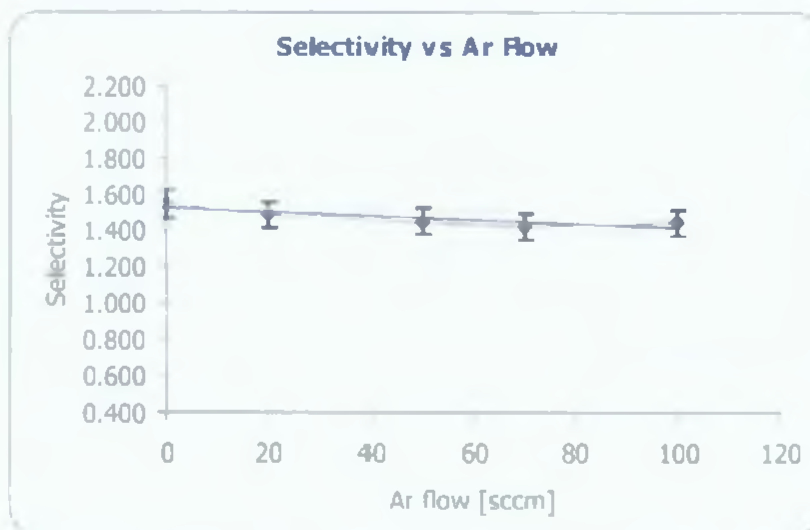

Figure 8-15. Process selectivity versus argon flow

In addition, the increase in argon flow rate increases the number of argon ions further decreasing selectivity due to the sputtering of photoresist. The OES scans revealed that the dominant ions are argon ions, which are responsible for sputtering of the sol-gel, causing a small increase in the etch rate. Taking these effects into consideration it can be argued against using argon as an addition to pure SF_6 for highly selective etching of sol-gels.

Lower pressure indicates that both photoresist and sol-gel film are equally exposed to impacting free ions and other high-energy species. The degree of pressure influence on selectivity is however low and supports the selection of the photoresist material as fairly resistive to purely chemical damage. This does not change the fact that the value of selectivity for this combination of materials is low, as it is for most of the silicate materials. As a result the thickness of the photoresist layer has to be comparable to the etching depth.

8.2.5. Influence of SF_6 Flow

The most important effect of etching sol-gel with SF_6 can be observed in Figure 8-16. This shows the existence of a threshold for SF_6 flow, below which we can see a significant drop in the selectivity. This shows the importance of the passivation process in achieving good selectivity in the process where deep etching is required.

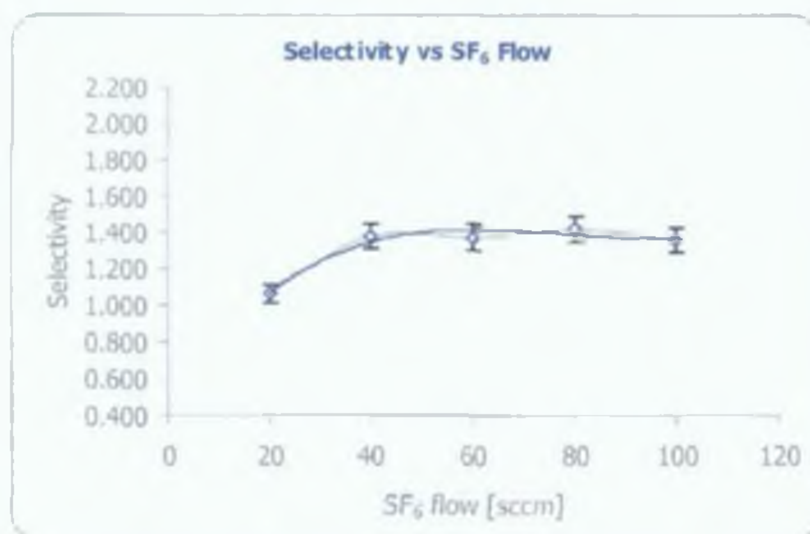

Figure 8-16 Process selectivity versus SF_6 flow

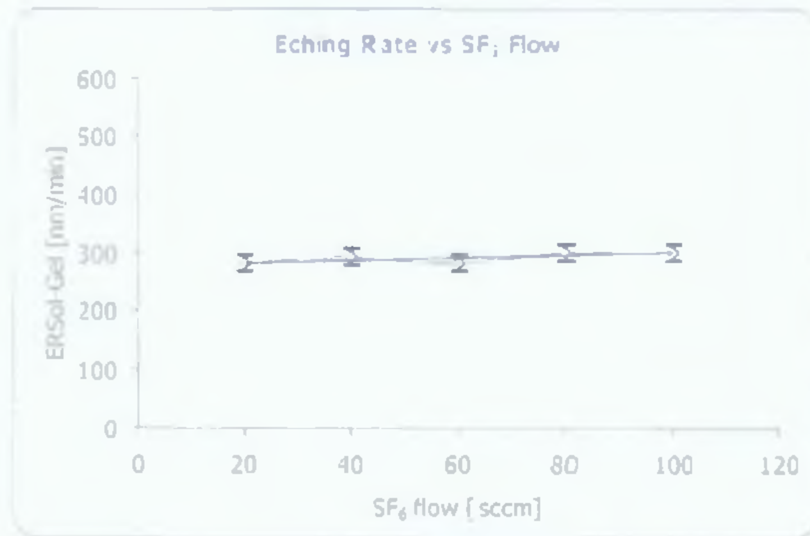

Figure 8-17 Process etch rate versus SF_6 flow

An overall stability of the etch rate with SF_6 again confirms the high Fluorine content in the plasma environment (Figure 8-17).

8.2.6. Influence of RF Power

Scans in RF power show little effect on etch rate (Figure 8-18). The strong increase in the selectivity of RF power (Figure 8-19) implies a significant photoresist etch rate decrease with power.

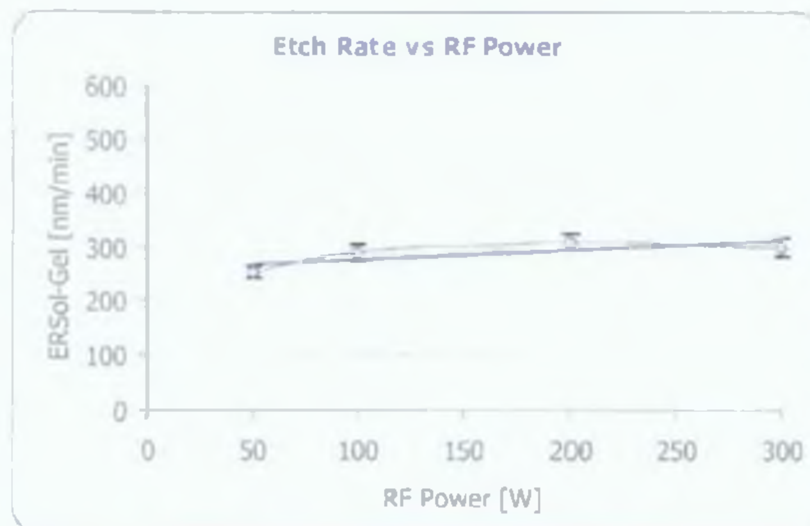

Figure 8-18 Process etch rate versus RF power

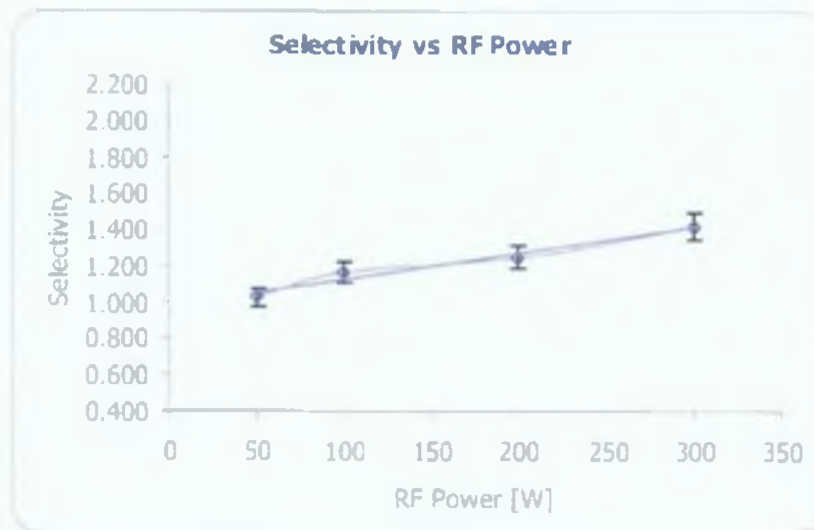

Figure 8-19 Process selectivity versus RF power

An explanation consistent with this result is that the surface passivation of the photoresist by a fluorine exchange reaction with hydrogen exceeds the destruction of the carbon-chain of the photoresist caused by the expected oxygen density increase at higher power.

In a typical OES spectrum, O_2, OII, S_2, SiO_2, CO, OH, C_2, ZrO, SII, OV, FIII, ZrI, SiII, SiF, ArI emission lines were observed (Figure 8-20) and confirm increased emission line intensities of argon, SiF and sputtered sol-gel molecular emission in higher RF power. The Roman numbers denote the level of ionisation of the particular atom.

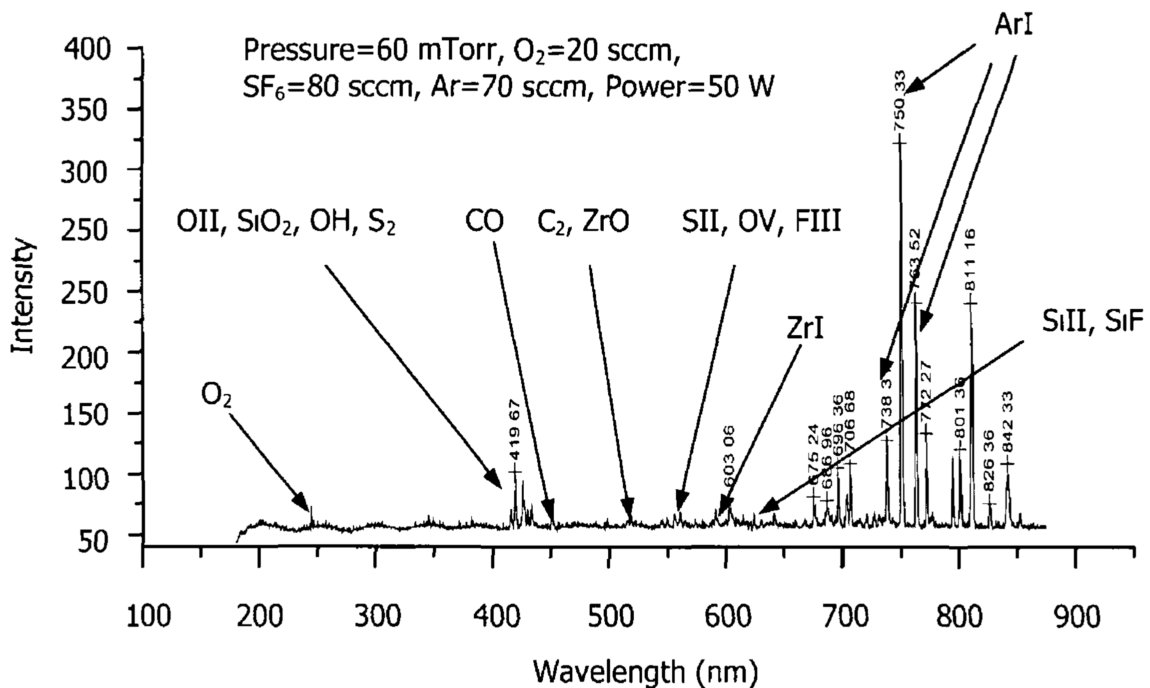

Figure 8-20 Typical optical emission spectra for Power=300 W, Pressure=60 mTorr, O_2 flow=20 sccm, SF_6=80 sccm, Ar flow=70 sccm

Visual observation of the etched samples influenced the use of plasma pressures below 30 mTorr, which aided the reduction of surface residues on the sol-gel leaving the surface clean and free of impurities, which may benefit the functionality of the LTM devices Residues at high pressure are thought to be micro-masking by the low volatility zirconium compounds, higher ion bombardment at low pressures alleviated this problem

8 2 7 RIE Process Parameters Selection

The optimisation of the etching condition was based on achieving the highest possible selectivity with reasonably fast etching rate The final etching set-up does not vary much from the original starting point The only changes introduced were the elimination of oxygen addition to the plasma and a small decrease in Argon flow Hence the final values of the etching process parameters for LTM fabrication were kept as follows Power = 300 W, 0_2 flow = 0 sccm, Ar flow = 60 sccm, Pressure = 60 mTor, bottom electrode temperature =15 °C, SF_6 = 80 sccm, Time = 60 min

This optimised RIE process etched the features as presented in Figure 8-21.

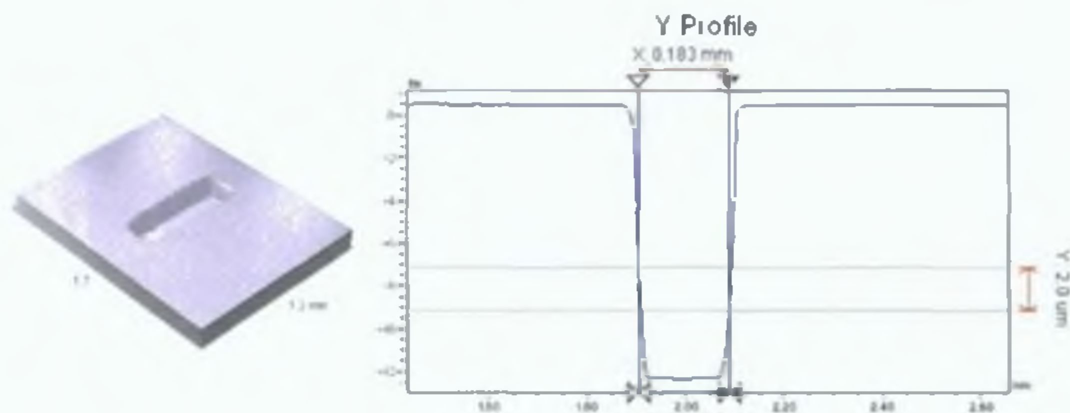

Figure 8-21 LTM device profile after etching with the optimised RIE process

A relatively high etch bias of the final etched structures as compared to the initial dimensions on the mask was observed. The average enlargement of the horizontal dimensions of the etched structures was 20 μm. This etch bias is probably a result of the inaccurate transfer of the dimensions from the mask to the photoresist, which would suggest that further improvement in the photopatterning procedure of the photoresist is required. However, no additional measurements were carried out to confirm this theory. The higher etch bias had no influence on the testing phase of the LTM development as this possibility was addressed in the design phase by incorporating a variety of chamber widths into the photolithographic mask.

In addition, as presented in Figure 8-22, the optimised RIE process achieved favourable roughness parameters, which were measured from the bottom of the etched chambers.

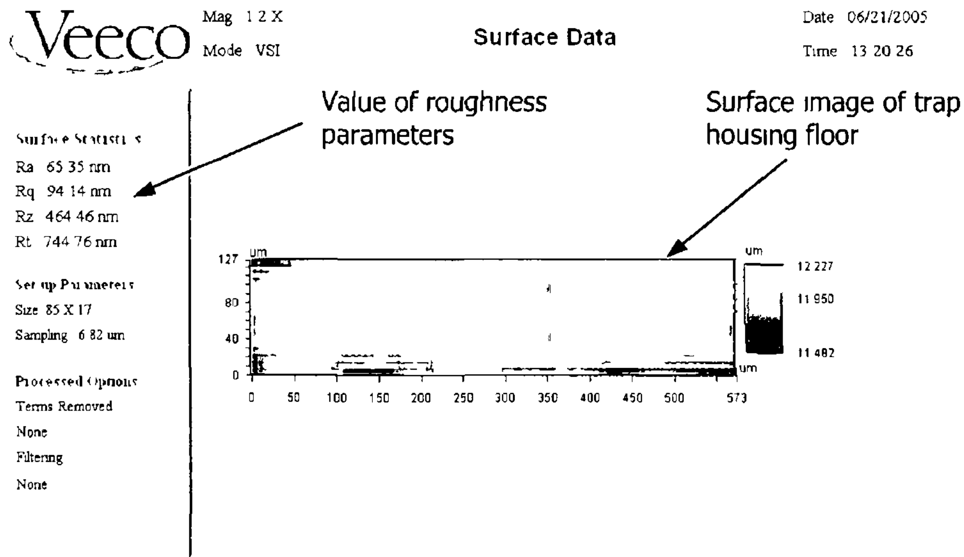

Figure 8-22 Roughness of the trap housing floor

The average roughness (Ra) of the chamber floor was found to be in each case below 70 nm These values of the roughness parameters were thought to be sufficiently low to prevent any influence on the trapping beams or trapped object

8.3. Conclusion

All the results from the conducted experiments appear to be consistent with the general theoretical approach of plasma etch processing taken Since our primarily goal was to optimise this particular process, the results are considered to be specifically adjusted for the plasma chamber available, sol-gel recipes, and photoresist layer etc

The presented optimisation process has explored Reactive Ion Etching as a means of LTM trap housing microfabrication Good etching rates and selectivity were obtained for a generally available thick photoresist material using SF_6 chemistry and provided a novel study of the influence of oxygen and argon addition

It has been shown that with the high flow of SF_6 gas there is enough chemistry available to achieve selectivity that allows 15 µm deep good quality etching, which is a requirement for the LTM device Thus the SF_6-based plasma chemistry and photoresist material can be recommended as a method of microfabrication for the LTM trap housing as well as for other photopatternable inorganic-organic composites synthesised by the sol-gel technique

9. Estimation of the LTM Trapping Forces

9.1. Introduction

Assuming that all previously obtained numerical estimations and assumptions are correct it can be shown that the LTM is capable of establishing a stable equilibrium point with sufficient optical forces to compensate for the major external forces acting on the trapped microsphere These however required two more physical measures to be taken, namely characterization of the light intensity distribution inside the LTM waveguide, and measurement of the power losses incurred by this light as it propagates between the fibre output and the trapping chamber

The requirement for the characterization of the light intensity distribution inside the waveguides was a direct result of the assumption that the waveguides are capable of guiding only the fundamental mode, with a Gaussian intensity distribution As discussed earlier, this condition was crucial for calculating the trapping efficiencies that allows the most efficient utilisation of the available optical power Thus once the LTM device was fabricated the waveguides had to be tested to confirm that they match the system specification

Subsequently, the optical losses had to be measured to provide information about the ultimate power of the light available from the output of the waveguides This optical power value was used to calculate the final LTM trapping forces as given by the Equations 2-24 and 2-25, assuming the initial power of the laser diode was 15 mW

The numerical estimation of the trapping forces was then compared to the calculated values of the external forces acting on the microspheres immersed in water solution and confined within the chamber walls This assessment was designed to provide assurance that the device would function properly, and it was completed prior to demonstration taking place

9.2. Optical Beam Intensity Profile

The waveguide dimensions and refractive index difference Δn =0.003 between the guiding and both the buffer and protective layers were designed to produce a single mode intensity profile at the waveguide output.

In order to confirm that this was really the case an intensity profile was obtained by launching the light from the pigtailed laser diode into the waveguide (Figure 9-1).

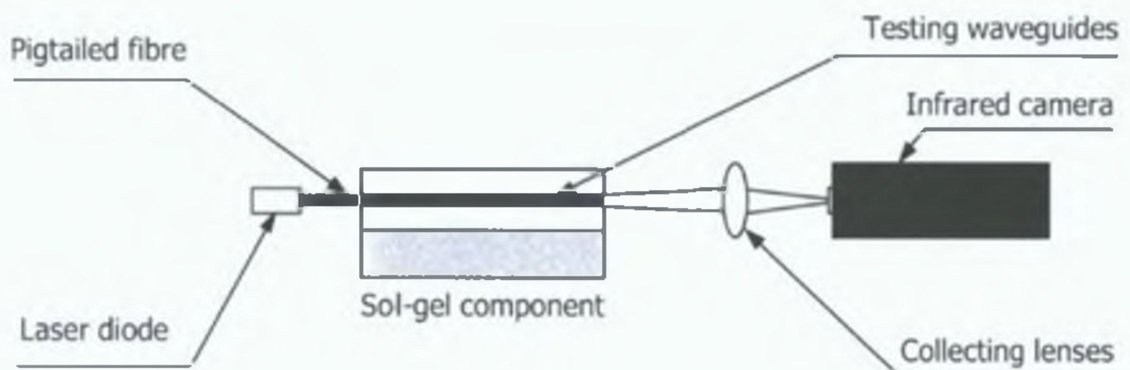

Figure 9-1. Optical setup for measuring waveguides intensity profile

The light coming out of the waveguide endface was collected using a series of lenses and focused on a highly sensitive Hamamatsu Photonics infrared camera (model: C2741). The result is presented in Figure 9-2 and it may be seen that the intensity profile is very close to the purely Gaussian profile.

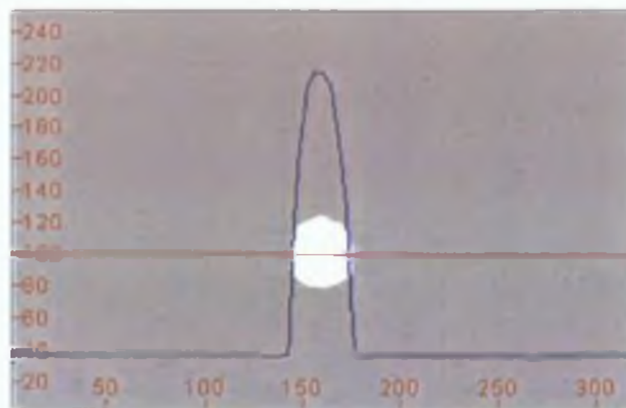

Figure 9-2. Single mode intensity profile of a 4 µm square waveguide

The experiments conducted on the waveguides in the range between 2 and 10 μm confirm that fabricated waveguides met the design specifications and allowed only the fundamental mode to be guided Similar but more rectangular intensity profiles of these waveguides were observed as a result of high dimension ratio between widths and heights of these waveguides

9.3. Optical Losses Measurement

As can be seen from Equations 2-24 and 2-25, the reduction in optical forces that can be induced on the dielectric object is directly proportional to the loss of laser power within the waveguide For this reason it was important to measure the losses of the optical power available on the waveguide output

The optical losses can be subdivided into three major groups propagation losses (incurred by the light propagating through the waveguide), coupling losses (those related to the transfer of the light between the optical fibre and the waveguide input) and finally output losses at the interface between the waveguide and the output medium [62,109-111]

Propagation losses usually occur as a result of the imperfections in the waveguide geometry and the type and quality of the material used to form a waveguide Three types of propagation losses that can be identified based on their source of origin scattering losses, absorption losses and radiation losses

Scattering losses can be subdivided into volume scattering and surface scattering Volume scattering is directly related to the imperfections in the material such as contaminants and crystal defects and nonuniformity of the refractive index Surface scattering losses occur because of waveguide sidewall roughness at the interface between the core and the cladding of a waveguide (in our case between the waveguiding layer and the protective or buffer layer)

The origin of radiation losses is the emission of photons into the media surrounding a waveguide, which cease to be guided These types of losses are of particular concern

when the waveguide is curved In that case the evanescent field on one side of the waveguide extends further into the surrounding material increasing the probability of the photons being radiated away from the propagating mode Since lower order modes have much less energy confined in the evanescent field than higher order modes, these lower order modes experience much lower radiation losses

The final contribution to the propagation losses is made by absorption losses, which are directly related to the material composition and thus its intrinsic ability of transforming the light power into heat power

The overall propagation loss in buried waveguides is usually measured in decibels per centimeter (10 dB/cm represents a decrease of power by an order of magnitude per 1 cm of waveguide length) It can be determined by measuring the ratio between input and output optical power through straight waveguides of different lengths

The second type of loss (coupling losses) is related to the light intensity loss that occurs in the connection between the waveguide and the optical fibre It is affected by intrinsic and extrinsic factors Intrinsic coupling losses are caused by inherent fibre (waveguide) characteristics such as core and cladding diameter mismatch, numerical aperture (NA) mismatch, and refractive index profile difference between a fibre and a waveguide Extrinsic coupling losses are caused by fibre-waveguide jointing techniques such as lateral misalignment, angular misalignment, fibre-waveguide separation, and poor fibre or waveguide endface preparation The coupling loss is measured in decibels as the loss of optical power between the fibre and the waveguide

The third type of loss (output losses) is in principle similar in the origin to the coupling loss and is a result of the backreflection of the light caused by the mismatch of the refractive indices of the waveguide and the output medium

For the purpose of estimating optical forces, the power loss of the light travelling through the ridge waveguides made from the developed sol-gel material was measured using the cut-back technique utilising the optical setup presented in Figure 9-3

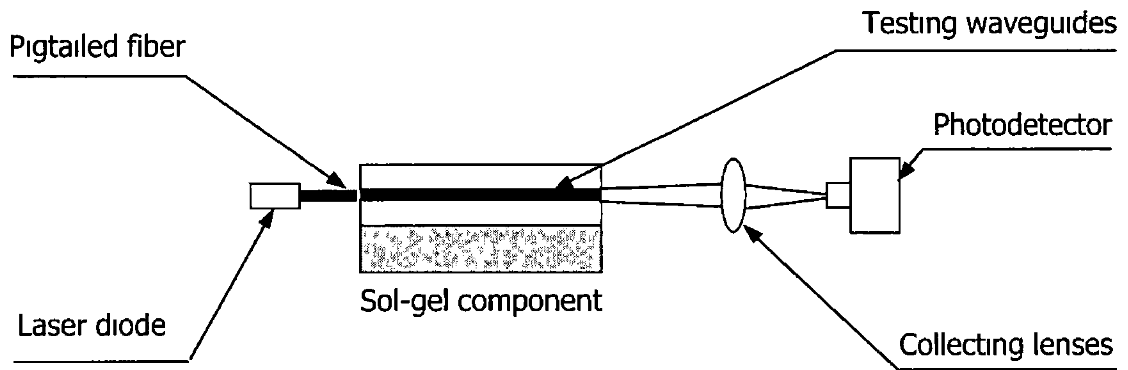

Figure 9-3 Cut-back method optical setup

The cut-back technique allows the measurement of both the coupling and propagation losses by comparing changes in the optical power at the waveguide output with the same initial coupled power for different waveguide lengths

The initial measurement involved launching laser diode light into the waveguide through the pigtailed optical fibre The initial wafer sample was 35 mm long and covered with several nominally identical channel waveguides The test waveguides used in the measurements were straight ridges They were also part of the same wafers from which the final devices were extracted, which means that they were exposed to the plasma environment in an identical fashion to the final devices

The coupling surfaces were cleaved along the wafer crystallographic planes and the optical power at the waveguide output was measured using a Thorl Labs DET410 photodectector The change in the intensity after each reduction in length was transformed into the decibel form using the equation

Equation 9-1

$$\alpha = \frac{10\log(P_0 / P_1)}{x_1 - x_0}$$

where

P_0 - optical intensity output before waveguide length reduction

P_1 - optical intensity output after waveguide length reduction

x_0 - initial length of the sample

x_l - length of the sample after reduction

By averaging each value over more than six measurements per waveguide length, the propagation losses were extrapolated by determining the slope of the input-to-output power ratio vs waveguide length plot (Figure 9-4) The results were also adjusted to provide the information about the average coupling losses inherent in the system The adjustment was performed by measuring the direct output intensity of the laser diode and adding this value to the results, which produced the shifting factor in the best fit line equation

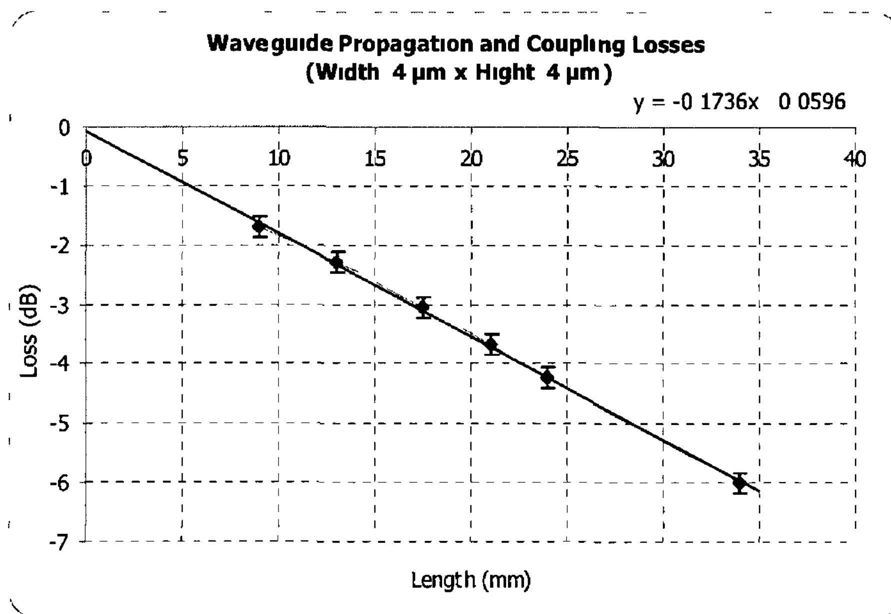

Figure 9-4 Waveguide propagation and coupling losses

The best-fit line slope indicates losses of 1 736 dB/cm and coupling losses of 0 06 dB The origin of the losses is probably due to imperfections in waveguide shape and low confinement of the fundamental mode due to the low refractive index difference between the waveguiding layer and the buffer, protective layers It is thought that the absorption losses for the optical wavelength (662 nm) used are negligible This was confirmed by obtaining UV-visible absorption spectra as shown in Figure 9-5

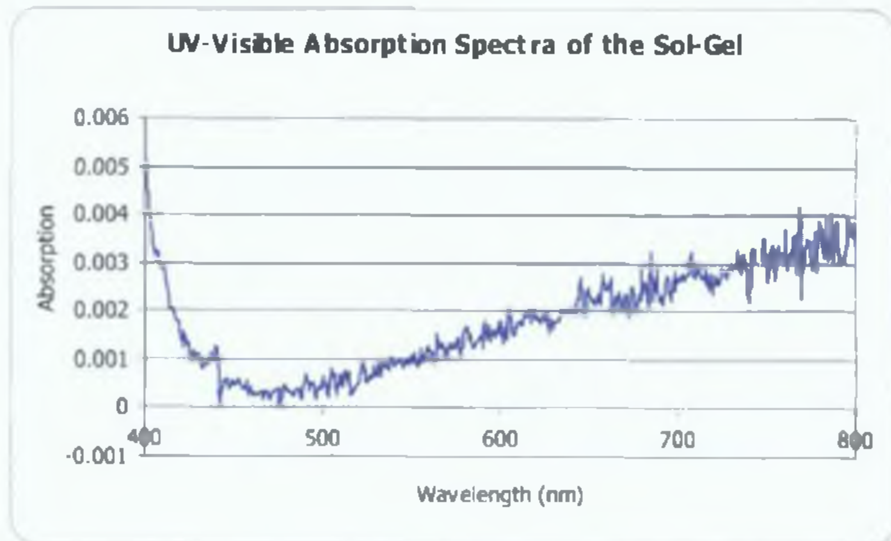

Figure 9-5 UV-visible absorption spectra of the LTM sol-gel material

The coupling losses for the 4 µm waveguide presented are considered marginal and this is probably due to the precise alignment and accurate match between sizes of the fibre core and the waveguide.

The overall experimental results gave an indication of the expected value of the optical power of the light ultimately available at the waveguide output and thus allowed the calculation of the real forces that could be produced by the LTM.

9.4. Result of Force Calculations

The section presents predictions of the optical forces acting on the microsphere obtained using Equations 2-24 and 2-25 for different trapping configurations. These estimations combine previously calculated trapping efficiencies for selected waveguide sizes, experimentally obtained waveguide losses and available laser diode power. In addition an attempt has been made to calculate the external forces that might act on the microsphere inside the trap chamber.

The overall external force acting on the microsphere inside the water solution near the chamber sidewalls comprises: combined buoyancy and gravity forces (F_{gb}), van der Waals forces (F_{vdw}) and electrostatic forces related to the charge (F_{el}) (Equation 9-2) [112].

$$F_{ext} \quad F_{gb} \quad F_{vdwr} \quad F_{el}$$ *Equation 9-2*

The combines buoyancy and gravity force is given by the Archimedes law

$$F_{gb} \quad g(\rho_1 \quad \rho_2)V$$ *Equation 9-3*

where ρ_1 and ρ_2 are densities of the microsphere and the solution respectively

Another component of the total external force is a van der Waals force, which is related to the intermolecular forces arising due to the probabilistic fluctuation of electron density around a molecule The van der Waals forces can be quantitatively estimated using Equation 9-4 [113]

$$F_{vdwr} \quad \left(\frac{\delta}{\delta \quad \sigma/2}\right)^2 \frac{2Hr_0}{3\delta^2(\delta \quad 2r_0)^2}$$ *Equation 9-4*

where

- σ surface roughness
- δ distance between microsphere boundary and the surface
- H Hamaker constant
- r_0 microsphere radius

The Hamaker constant was estimated to form the Hamaker constant of individual materials (polystyrene, water and silicon), which were engaged in the interaction [114,115,116] A value of 1 3e-20 J was obtained following the procedure described by Bergendahl and Grasso [114]

The electrostatic force, which arises between static (non-moving) charges is given by [117]

$$F_{el} \quad 2\pi\varepsilon\varepsilon_0 r_0^2 V^2 \left(\frac{1}{2(\delta \quad r_0)^2}\right)$$ *Equation 9-5*

where

- ε relative permittivity of water
- ε_0 permittivity of free space
- r_0 microsphere radius
- δ distance between microsphere boundary and the surface
- V electrostatic potential given by

$$V \quad \frac{Q}{4\pi\varepsilon\varepsilon_0 r_0}$$

and Q is the overall additional charge stored by the microsphere

A unique property of the electrostatic force is that it can be either attractive or repulsive, which depends on the type of the interacting charges being accumulated in the material The ability of the material to accumulate certain types of charges is called the material triboelectricity and it is related to the material affinity for giving up negatively charged electrons In our case the interaction occurs between polystyrene and silicon, which both have negative triboelectricity [118,119,120], which means that the overall accumulated charge should be negative and induces a repulsive electrostatic force (for this reason a minus sign for the electrostatic force was assigned in the scalar Equation 9-2)

It is not certain how the fabrication process and the presence of the electromagnetic field, when the sphere interacts with the laser beam, influence the direction and the quantity of charge accumulated in both materials However, based on the work of Gady at al [117] the charge accumulated in the microsphere in the presence of a water solution was estimated as 700e This value was used to calculate the electrostatic force between the microsphere and the silicon wafer

The numerical value of the external forces (F_{ext}) was based on the set of constant parameters resented in Table 9-1

Parameter		Value	Unit
g	earth gravitational constant	9 81	m/s^2
Υ_p	density of polystyrene	1050	kg/m^3
Υ_w	density of water	1000	kg/m^3
ς	LTM surface roughness	7 00E-08	m
H	Hamaker constant	1 13E-20	J
H	relative permittivity of water	80 3	
e	electron charge	1 60E-19	J
H	permittivity of free space	8 85E-12	$C^2J^{1}m^{1}$
Q	number of negative charges	7 00E+02	
Γ	distance between centre of the sphere and the LTM floor	7 00E-06	m

Table 9-1 Constant parameters used in external forces calculations

Thus following Equations 9-2 to 9-6, the value of the external forces was calculated and summarized in Table 9-2

Calculated external forces (F_{ext})					
F_{bg}	combined buoyancy and gravity force	-7 3304E-16	-6 368E-15	-2 4512E-14	N
F_{vdwr}	van der Waals forces	-6 70E-18	-3 34E-17	-7 98E-17	N
F_{el}	electrostatic force	7 18E-15	7 18E-15	7 18E-15	N
Total external forces		6 44E-15	7 80E-16	-1 74E-14	N

Table 9-2 Calculated external forces acting on the polystyrene microsphere

By putting optimised trapping efficiencies (Table 9-3) into Equations 2-24 and 2-25 and using measured values of waveguide losses, the numerical values of total optical forces were calculated Also, the initial optical power of the available laser diode of 1 5e-02 W and water refractive index of 1 33 were fitted in the calculations (Table 9-3)

Variable		Values			Units
r_0	particle radius	1 4185E-06	0 000002916	4 57E-06	m
w	waveguide size	2	4	8	µm
s	trap housing size (separation distance)	40	80	160	µm
L_p	waveguide propagation losses (excl coupling)	-1 8	-1 8	-1 8	dB/cm
L_c	coupling losses	-0 1	-0 1	-0 1	dB
l_w	single waveguide length	3	3	3	cm
P_{eff}	effective power on the waveguide output	4 23E-03	4 23E-03	4 23E-03	W
Q_{zt}	axial trapping efficiency	0 002	0 01	0 0025	
Q_{xt}	transverse trapping efficiency	0 25	0 14	0 19	
pc	relative power difference between P_1 and P_2	50 0%	50 0%	50 0%	
Calculated optical forces					
F_{zt}	effective axial trapping force	1 88E-14	9 38E-14	2 34E-14	N
F_{xt}	effective transverse trapping force	9 38E-12	5 25E-12	7 13E-12	N

Table 9-3 Calculated optical forces and a typical set of variables used in calculations

The comparison of the external forces with optical forces revealed that the optical forces are much bigger than any component of the total external force The effective transverse trapping force, which prevents a sphere from falling down and holds it at a set distance from the LTM floor was in the worst-case two orders of magnitude higher than the total external force

In fact, both the van der Waals force and the electrostatic force decrease sharply with distance between the interacting mediums and they are in general negligibly small compared to the combined buoyancy and gravity forces At this distance the only force that could have any impact on the trapped object is the combined buoyancy and gravity force, which rise quickly as the radius of the microsphere increases

9.5. Conclusion

The obtained experimental results proved that the fabricated waveguides had single mode properties and confirmed that this important condition for creating a stable trap was met

It was also shown that the optical forces produced by the LTM would be large enough to match all the external forces acting on polystyrene beads of various sizes This should allow the device to achieve full functionality within specified trapping parameters and external conditions

For LTM prototype testing, the power of the laser diodes was chosen to maximise the available forces and increase the probability of trapping occurring However, it has to be noted that in a real application, higher power lasers typically result in a higher possibility of inducing damage to living objects and this is not always desirable

Finally, this chapter outlined experiments and calculations that concluded the last step of the LTM development before the fabricated device was put into the test as presented in the following chapter

10. Laser Trapping Observation

10.1. Introduction (Experimental Setup)

Following the procedure described in Chapter 5 the LTM prototype was fabricated and prepared for testing as presented in Figure 10-1

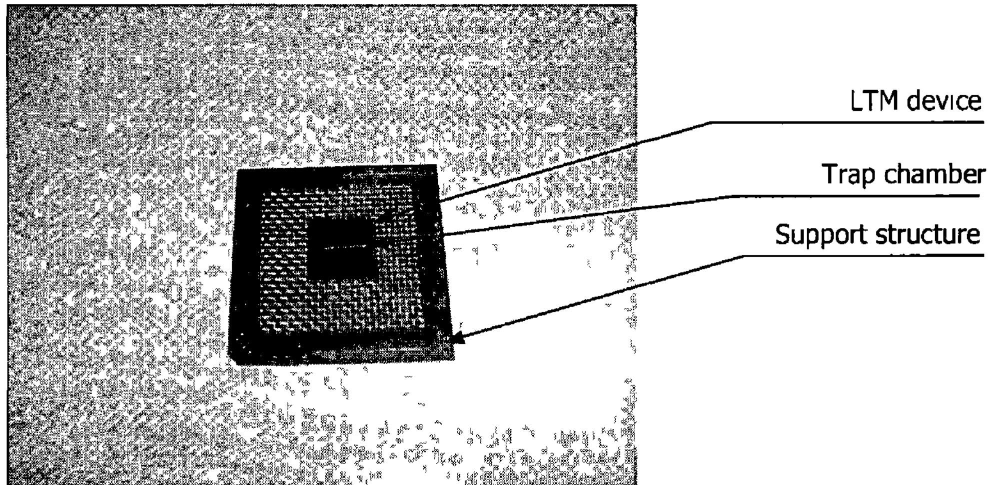

Figure 10-1 The LTM testing pad

The LTM testing was carried out using a custom designed Elliot Scientific optical setup (Figure 10-2)

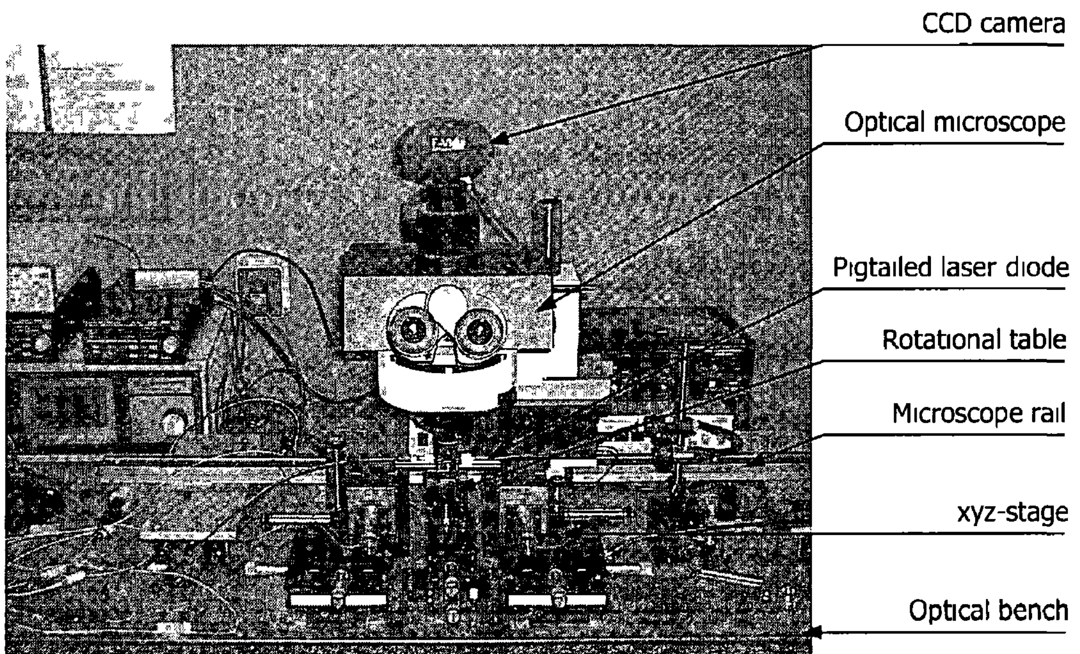

Figure 10-2 Experimental optical setup

This state-of-the-art system consisted of a floating optical table, two xyz-stages, rotational table, a movable optical microscope with CCD camera, two pigtailed laser-diodes and multiple controllers for operating various parts of the setup The xyz-stages allowed precise positioning of the pigtailed optical fibres using either classical micrometer gauges or electronically controlled piezoelectric actuators for more accurate alignment of the fibres

The optical microscope was mounted over the top of the round table using a specially designed hook The hook was situated on the xy-stage, which allowed accurate positioning of the microscope over a short distance Finally the xy-stage rested on a rail, which was used for rough manipulation of the microscope position over a longer distance

10.2. Testing Procedure

The laser diodes were mounted on top of the xyz-stages with their output ends facing each other (Figure 10-3) The LTM testing pad was placed on top of the rotational table and clamped

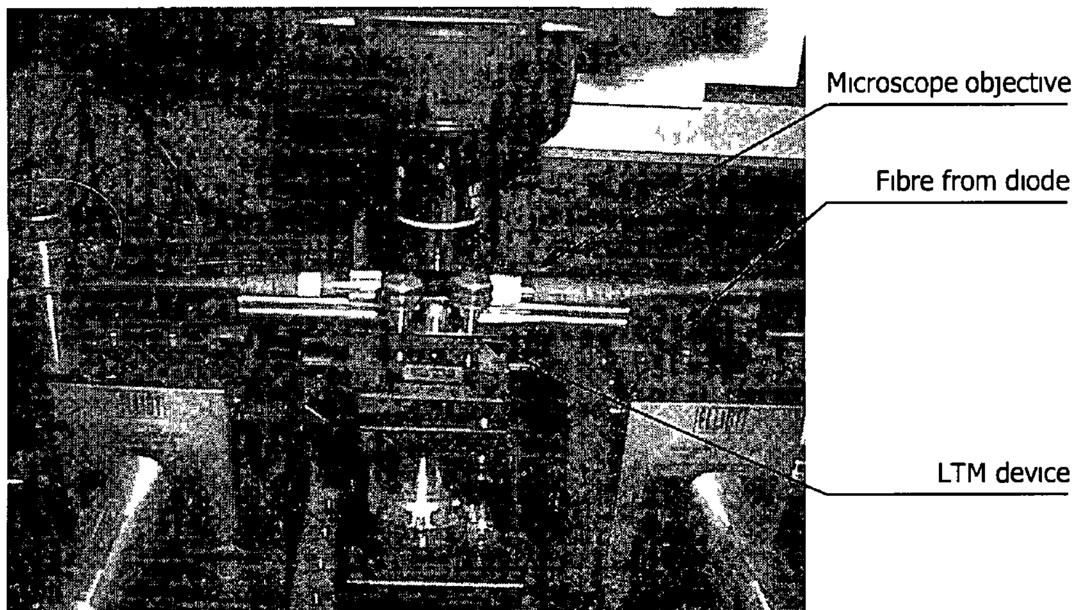

Figure 10-3 Laser diodes alignment

The identical power output was established from both laser diodes and their outputs were precisely aligned with the LTM waveguides, coupling the light into waveguides

from both sides of the device The long-travel feature of the microscope facilitated this task Once the alignment was finished the distinctive scattering from the waveguide core and the waveguide output inside the trap chamber was observed (Figure 10-4)

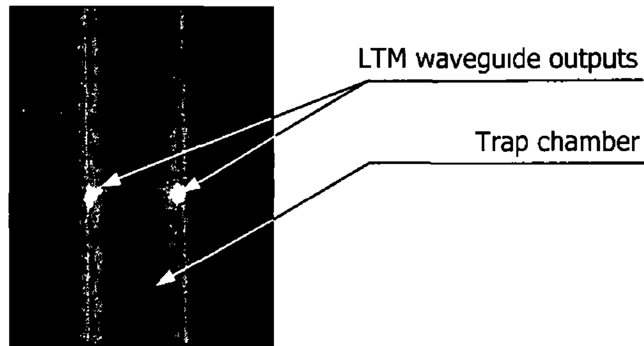

Figure 10-4 LTM device

The microscope was then removed and a small quantity of the water solution containing the microspheres was dispensed into the particle chamber using a micropipette Then the microscope was then moved back to the original position and the trapping was observed The scattering pattern of the trapped particle can be seen It is indicated by the distinctive scattered light, which can be observed on the CCD camera installed on the microscope as presented in Figure 10-5

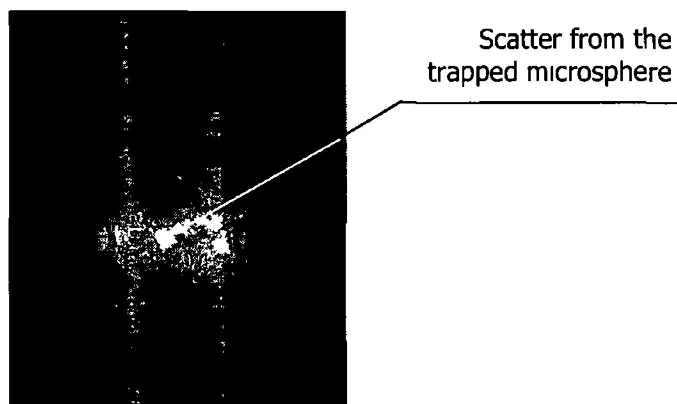

Figure 10-5 Trapped microsphere using LTM

In order to test the working principle of the device the optical power of one of the beams was reduced and a change in the microsphere position could be observed (Figure 10-6 a-l)

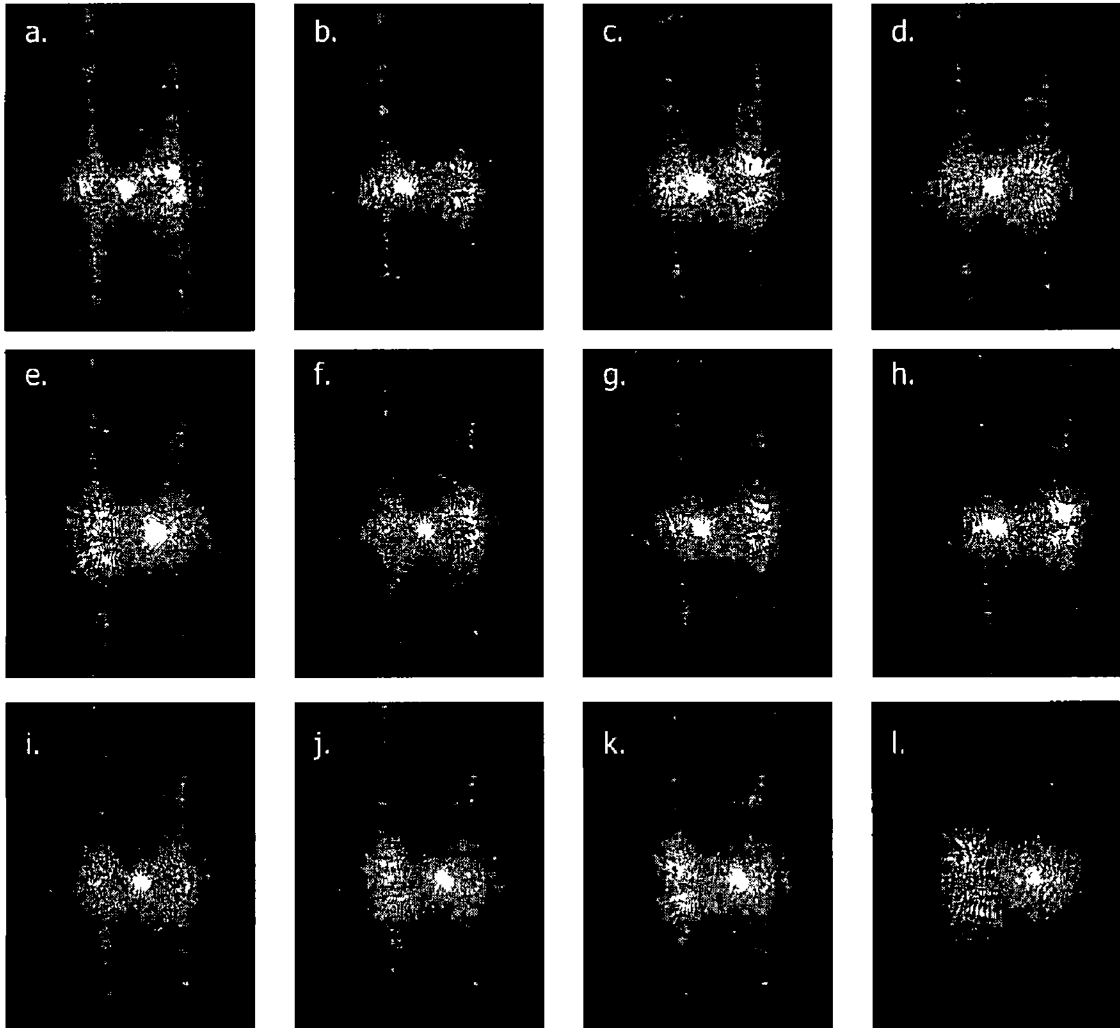

Figure 10-6 Optical manipulation using LTM device (beam waist separation s=70 µm, waveguide width=4 µm, microsphere radius r_0=2 916 µm)

Figure 10-6a shows a trapped microsphere in the neutral position in the middle of the trap chamber and represents the state when two counter-propagating beams carry identical optical power Then power of the left beam was reduced and the expected movement of the microsphere towards the weaker output beam occurred (Figure 10-6b)

Then the equality of beam powers was restored and the sphere returned to the centre position inside the trap chamber (Figure 10-6c-d) Once the sphere returned to the original position power of the right beam was reduced and the sphere moved towards the right side of the chamber (Figure 10-6c-d) The same procedure was repeated again as presented in (Figure 10-6f-l)

The trapping was observed for various waveguides size between 2 µm and 10 µm and for multiple chamber diameters between 70 µm and 210 µm Figure 10-7 shows the optical trapping in different trapping conditions

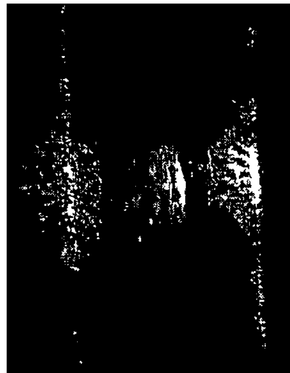

Figure 10-7 Optical trapping (beam waist separation s=160 µm, waveguide width= 10 µm, microsphere radius r_0=4 57 µm)

Experiments also provided a rare opportunity to confirm the validity of the ray optics model Following Flynn at all [17], Figure 10-8 a presents a ray optics model for rays' reflection and refraction inside the spherical dielectric object for a lightly focused laser beam

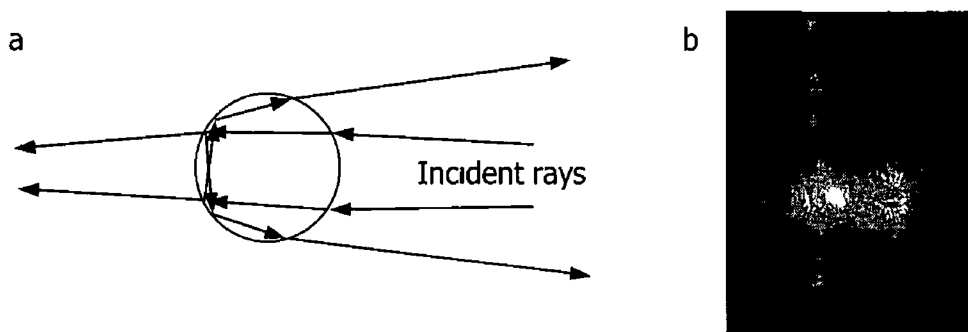

Figure 10-8 Rays refraction and reflection on the spherical dielectric object a theoretical model, b experimental result

Similar ray paths of rays were observed during experimentation as presented in Figure 10-6b and 10-8b Since in this case the higher intensity light propagates from the right towards the left side of the trap chamber it becomes simultaneously focused and reflected by the microsphere creating one bright spot on the left wall of the chamber and two bright spots on the right wall

11. Conclusions and Suggestions for Further Work

Adding to the recent trend towards miniaturisation and integration of optical devices, a working prototype of a unique dual-beam optical trapping platform was presented. The optical trapping capability of the device was successfully demonstrated using polystyrene microspheres, complementing previously published work on optical trapping and its biological applications.

The achieved success resulted from conceptual and experimental work conducted on the various techniques and technologies implemented in the device. The multidisciplinary research required a high level of expertise in optical trapping and a specialised knowledge of material and plasma science, photolithography, material deposition techniques and waveguiding theory. In addition the use of many highly sophisticated scientific tools, such as an optical interferometer and prism couplers for refractive index and thickness measurements, had to be mastered.

The project initiated new research fields that will present numerous opportunities and challenges for possible further investigations. These include:

- Utilisation of higher order optical modes for creating several equilibrium points between two waveguides

  The characteristics of optical waveguides can be redesigned to allow propagation of higher order optical modes. This should produce multiple stable trapping equilibriums making multiple trapping possible. A similar effect can be achieved by taking advantage of the interference phenomena which occurs between two coherent beams between two samples

- Implementation of the multi-beam trap allowing 2D manipulation

  A complementary set of the counter-propagating beams perpendicular to the existing ones can be created to improve trap stability and allow 2D spatial manipulation of the object. In addition the integration of optical switches within the platform will allow reduction of the required laser diode inputs.

- Examination of biological species such as proteins, antigens, hemoglobin etc using the trapping technique and studies of the influence of laser power on their molecular structures

- Substitution of the silicon substrate with a transparent one will allow observation of the trapped object from beneath without restricting user access to the trapping chamber

  The major consideration for the selection of a viable transparent substrate will be high surface uniformity comparable to that achieved by using silicon wafers Transparency to LTM operational wavelengths is another key consideration

- Implementation of the scattering detection system

  Wide multimode waveguides can be utilised as scattering detection systems, collecting and transmitting information about the intensity and directionality of the scattered light from the object These data can be further interpreted to obtain information about object properties such as shape dimensions, and refractive index

- Implementation of microfluidic channels

  A microfluidic channel can be incorporated into the device and the optical forces can be utilised for sorting particles travelling through the channel Particles of certain size, dimension, and refractive index can be separated from the others by designing optical traps that respond to particular physical parameters of the object

- The process engineering of the LTM, including photolithography, RIE etching and materials, can be further optimised, which will result in improved quality of the LTM components such as waveguides, trap housing and material layers

- Detailed investigation of the polarisation rotation effect

Further examination of the theoretical model used in this work could present another major challenge in the future The development of a numerical approximation that

could calculate the dual-beam trapping forces when multimode waveguides are considered, or when the spherical objects are replaced with objects of other shapes, is an example of one such challenge

- The compatibility with optical tweezer systems might be investigated by redesigning the chamber illumination system and tweezer optics to utilise both system advantages for specific biotechnological applications

This list, although extensive, does not exhaust all possible modifications that might be incorporated into the LTM system Many other system improvements can be developed, limited only by personal imagination This feature has vast range of LTM applications in the biology and biotechnology sectors and it may soon make the device an indispensable tool in many biological applications

A further consideration to be addressed is the possible tailoring of the device functional parameters to various specific applications This will require establishing close cooperation with those directly engaged in using the device on a daily basis Their opinions and suggestions should be taken into consideration before any device modification will take place This practice is desirable both from a scientific and a commercial point of view, as it will permit a clearer understanding of which system parameters can be successfully modified and which are the most crucial for the particular application

Finally the commercial potential should be explored by developing potential markets, the needs and wants of which can be satisfied by the qualities offered by the LTM The ultimate success of the lab-on-a-chip LTM device will be achieved, once its various practical applications are transformed into a prosperous and successful enterprise

12. References

1 E Sidick, S Collins, A Knoesen, "Trapping forces in a multiple-beam fiber-optic trap", Applied Optics, Vol 36, No 25, pp 6423-6433, 1997

2 A Ashkin, "Optical trapping and manipulation of neutral particles using lasers", Proc Natl Acad Sci USA, Vol 94, pp 4853-4860, 1997

3 R K Soong, G D Bachand, H P Neves, A G Olkhovets,, H G Creighead, C D Montemagno, "Powering an Inorganic Nanodevice with a Biomolecular Motor", Science, Vol 290, November 2000

4 K D Bonin and B Kourmanov, "Light torque nanocontrol, nanomotors and nanorockers", Optics Express, Vol 10, No 19, pp 984-989, 2002

5 T R Strick, V Croquette and D Bensimon, "Single-molecule analysis of DNA uncoiling by a type II topoisomerase", Nature, Vol 404, pp 901-904, 2000

6 Ch L Kuyper, D T Chiu, "Optical Trapping A Versatile Technique for Biomanipulation", Focal Point, Volume 56, Number 11, pp 300A-312A, 2002

7 Gijs J L Wuite, R J Davenport, A Rappaport, and C Bustamante, "An Integrated Laser Trap/Flow Control Video Microscope for the Sudy of Single Biomolecules", Biophysical Journal, Volume 79, pp 1155-1167, 2000

8 S M Block, "Optical tweezers A new tool for biophysics", Non-invasive Technique in Cell Biology, Wiley-Liss Inc , New York, pp 375-402, 1990

9 Amit D Mehta, Katherine A Pullen, James A Spudich, "Single Molecule Biochemistry Using Optical Tweezers " FEBS Letters 430, pp 23-27, 1997

10 H M Haruff, J Munakata-Marr and D W M Marr, "Directed Bacterial Surface Attachment via Optical Trapping", Colloids and Surfaces B Biointerfaces, 27 (2-3), pp 189-195, 2002

11. Fallman E, Schedin S, Jass J, Andersson M, Uhlin BE, Axner O, "Optical tweezers based force measurement system for quantitating binding interactions: system design and application for the study of bacterial adhesion", Biosens Bioelectron.,19(11):1429-37, 2004

12. Amit D. Mehta, Matthias Rief, James A. Spudich, David A. Smith, Robert M. Simmons, "Single-Molecule Biomechanics with Optical Methods", *Science*, Vol 283, Issue 5408, pp. 1689-1695, 1999

13. R. Gauthier, A. Frangioudakis; "Optical levitation particle delivery system for a dual beam fiber optic trap"; Applied Optics, Vol. 39, No. 1, pp.26-33, 2000

14. A. Ashkin; Acceleration and trapping of particles by radiation pressure"; Phys. Rev. Lett., Vol. 24, No. 4, pp. 156-159, 1970

15. A. Constable, Jinha Kim, J. Mervis, F. Zarinetchi, M. Prentiss; "Demostration of a fiber-optical light-force trap"; Optics Letters, Vol. 18, No. 21, pp. 1867-1869, 1993

16. A. Ashkin, J.M. Dziedzic; "Observation of Radiation-Pressure Trapping of Particles by Alternating Light Beams"; Phys. Rev. Lett., Vol. 54, No. 12, pp. 1245-1248, 1985

17. Richard A. Flynn, Bing Shao, Mirianas Chachisvilis, Mihrimah Ozkan and Sadik C. Esener, "Counter-propagating optical trapping system for size and refractive index measurement of microparticles ", Biosensors and Bioelectronics, In Press, Corrected Proof, Available online 22 April 2005

18. J. Guck, R. Ananthakrishnan, C.C. Cunningham, & J. Käs, Stretching biological cells with light, *J. Phys. Cond. Matter*, 14(19): 4843, 2002

19. S. Collins, R. Baskin D. Howitt; "Microinstrument gradient-force optical trap"; Applied Optics, Vol. 38, No. 28, pp.6068-6074, 1999

20. E. R. Lyons, G. J. Sonek; "Confinement and bistability in a tapered hemispherically lensed optical fiber trap"; Appl. Phys. Lett. Vol. 66, No. 13, pp. 1584-1586, 1995

21 Steven Chu, J E Bjorkholm, A Ashkin, A Cable, "Experimental Observation of optically Trapped Atoms" ", Phys Rev Lett , Vol 57, No 3, pp 314-317, 1986

22 N Kitamura and F Kitagawa, "Optical Trapping-Chemical Analysis of Single Microparticles in Solution", *J Photochem Photobiol C Photochemical Reviews*, vol 4, No 3, pp 227-247, 2003

23 Svoboda K , Block S M , "Biological applications of optical forces " Annual Rev Biophys Biomol Struct 23, pp 247-85, 1994

24 Neuman C , and Block S "Optical trapping Review of Scientific Instruments", Vol 75, pp 2787-2808, 2004

25 Lang M J , and Block S M , "LBOT-1 Laser-based optical tweezers" Am J Phys 71 201, 2003

26 R Lugowski, B Kolodziejczyk, Y Kawata, "Application of laser-trapping technique for measuring the three-dimensional distribution of viscosity", Optics Communications, Vol 202, pp 1-8, 2002

27 Stephen P Smith, Sameer R Bhalotra, etc , "Inexpensive optical tweezers for undergraduate laboratories", Am J Phys , Vol 67(1), pp 26-35,1999

28 R Gussgard, T Lindimo, "Calculation of the trapping force in a strongly focused laser beam", J Opt Soc Am B, Vol 9, No 10, 1992

29 K Dholakia, G Spalding and M MacDonald, "Optical tweezers the next generation", Physics World, pp 31-35, October 2002

30 C Jensen-McMullin, E R Lyons, Y Jiang, H P Lee, "Optical trapping Excitation and detection of polystyrene beads in a fiber-based sislicon V-groove system", Proceedings of SPIA Vol 4253, pp 125-131, 2001

31. K.F. Ren, G. Greha, G. Gouesbet, "Prediction of reverse radiation pressure by generalized Lorenz-Mie theory", Applied Optics, Vol. 35, No. 15, pp. 2702-2710, 1996

32. Y. Harada, T. Asakura, "Radiation forces on a dielectric sphere in the Rayleigh scattering regime", Optics Communications, Vol. 124, pp. 529-541, 1996

33. T.A. Nieminen, H. Rubinsztein-Dunlop, N.R. Hackenberg, A.I. Bishop; "Numerical modelling of optical trapping", Optics Communications, Vol. 142, pp. 468-471; 2001

34. Tom C. Bakker, Gerlo Hesselink, Bart G. de Grooth and Jan Greve; "Experimental and Theoretical Investigations on the Validity of the Geometrical Optics Model for Calculating the Stability of Optical Traps"; Cytometry, Vol 12, pp. 479-485, 1991

35. K.F. Ren, G. Greha, G. Gouesbet; "Radiation Pressure Forces exerted on a particle arbitrarily located in a Gaussian beam by using the generalized Lorenz-Mie theory, and associated resonance effects"; Optics Communications, Vol. 108, pp. 343-354; 1994

36. W.H. Wright, G.J. Sonek, and M.W. Berns, "Parametric Study of the forces on microspheres held by optical tweezers", Applied Optics, Vol. 33, No. 9, pp. 1735-1748, 1994 (forces calculation for tweezers)

37. K. Svoboda and S. M. Block, "Optical trapping of metallic Rayleigh particles", Optics Letters, Vol. 19, No. 13, pp. 930-932, 1994

38. K. Visscher, G.J. Brakenhoff, "Theoretical study of optically induced forces on spherical particles in a single beam trap II: Mie scatterers", Optik, 90 No. 2, pp. 57-60, 1992

39. Born, Wolf, "Principles of optics: electromagnetic theory of propagation, interference" - 6th ed. - Oxford; New York, Pergamon Press, 1980

40 T A Nieminen, H Rubinsztein-Dunlop, and N R Heckenberg, "Calculation and optical measurement of laser trapping forces on non-spherical particles", J Quantitative Spectroscopy and Radiative Transfer, No 70, pp. 627-637, 2001

41 R C Gauthier, M Ashman and Ch P Grover, "Experimental confirmation of the optical-trapping properties of cylindrical objects", Applied Optics, Vol 38, No 22, pp 4861-4869, 1999

42 Jochen Guck, Revathi Ananthakrishnan, Hamid Mahmood, Tess J Moon, C Casey Cunningham, and Josef Kas, "The Optical Stretcher A Novel Laser Tool to Micromanipulate Cells", Biophys J , p 767-784, Vol 81, No 2, 2001

43 Mihrimah Ozkan, Mark Wang, Cengiz Ozkan, Richard Flynn, Aaron Birbeck and Sadik Esener, "Optical manipulation of objects an biological cells in microfluidic devices", Biomedical Devices 5 1, pp 61-67, 2003

44 Mikhail A Proskurnin, Vera B Ivleva, Nataliya Yu Ragozina, and Elena K Ivanova, "The use of Triton X-100 in Thermal lensing of aqueous Solutions", Analytical Sciences, Vol 16, pp 397-401, 2000

45 L Paterson, M P MacDonald, J Arlt, W Sibbett, P E Bryant, K Dholakia, "Controlled Rotation of Optically Trapped Microscopic Particles", Science, Vol 292, pp 912-914, 2001

46 R Gauthier, M Ashman, "Simulated behaviour of single and multiple spheres in the trap region of focused laser beams", Appl Opt , Vol 37, pp 6421-6431, 1998

47 Shigeki Koyanaka, Shigehisa Endoh, "Three dimensional analysis of the movement of various micros-sized particles under laser radiation pressure", Powder Technology, Vol 116, pp 13-22, 2001

48 M E J Friese, T A Nieminen, N R Heckenberg and H Rubinsztein-Dunlop, "Optical alignment and spinning of laser-trapped microscopic particles", Letters to Nature, Vol 394, pp 348-350, 1998

49 Svoboda, K and Block, S M Biological applications of optical forces Ann Rev Biophys Biomol Struct 23 247-285 (1994)

50 Konig, K , H Liang, M W Berns and B J Tromberg Cell damage in near-infrared multimode optical traps as a result of multiphoton absorption Optics Lett 21 1090-1092, 1996

51 Guenther Leitz, Erik Fallman, Simon Tuck, and Ove Axner, Stress Response in Caenorhabditis elegans Caused by Optical Tweezers Wavelength, Power, and Time Dependence, Biophysical Journal, pp 2224-2231, Vol 82, No 4, April 2002

52 Konig, K , Y Tadir, P Patrizio, M W Berns and B J Tromberg Effects of ultraviolet exposure and near infrared laser tweezers on human spermatozoa Human Reproduct 11 2162-2164, 1996

53 Peter M Cellers, J Conta, "Measurement of localized heating in the focus of an optical trap", Applied Optics, Vol 39, No 19, July 2000

54 G J Sonek, Y Liu, R H Iturriaga, In situ microparticle analysis of marine phytoplankton cells with infrared laser-based optical tweezers, Applied Optics LP, vol 34, Issue 33, p 7731, 1995

55 S Motakef, J M Boulton, R L Roncone, G Neilson, G Teowee and D R Uhlmann "Optical Loss Study of MPEOU-Based Polyceram Planar Waveguides" Applied Optics, 34, pp 721-728, 1995

56 O Shapira, A F Abouraddy, J D Joannopoulos, Y Fink, "Complete modal decomposition for optical waveguides Complete modal decomposition for optical waveguides," Physical Review Letters 94, 14, 143902/1-4, 2005

57 Allan W Snyder and John D Love, " Optical waveguide theory", Chapman and Hall, 1983

58. D. Bosc; N. Devoldere, M. Bonnel, J. L. Favennec, D. Pavy, "Hybrid silica-polymer structure for integrated optical waveguides with new potentialities", Materials Science and Engineering, B, 57, pp. 155-160, 1999

59. X. Orignac, R.M. Almeida, "Silica-based sol-gel optical waveguides on silicon", IEE Proc. Optoelectr., 143, pp 287-292, 1996

60. S. Jeong, W. Jang, and J. Moon, "Fabrication of Photo-Patternable Inorganic – Organic Hybrid Film by Spin-Coating", Thin Solid Films, 466 [1 -2] 204 –208, 2004

61. F. Horowitz, E. J. C. Dawnay, M. A. Fardad, M. Green, E. M. Yeatman, "Towards better control of sol-gel film processing for optical device applications" J. Nonlinear Opt. Phys. Mat. 6, 1-18 (1997)

62. R. M. Almeida, "Sol-gel planar waveguides for integrated optics", J. Non-Cryst. Sol., Vol. 259, pp. 176–181, 1999.

63. Marc J. Madou, "Fundamentals of microfabrication" Boca Raton, Fla., London, CRC Press, 1997

64. H. Krug, F. Tiefensee, P. W. Oliveira, H. Schmidt, "Organic-inorganic composite materials: optical properties of laser-patterned protective-coated waveguides", Proc. SPIE, Vol. 1758, pp. 448-455, Sol-Gel Optics II, 1992

65. K. R. Kribich, H. Barry, R. Copperwhite, B. Kolodziejczyk, K. O'Dwyer, J. M. Sabattié, B. D. MacCraith., Thermo-optic switches using sol-gel processed hybrid materials, Proc. SPIE Vol. 5451, p. 518-528, 'Integrated Optics and Photonic Integrated Circuits' (Giancarlo C. Righini, Seppo Honkanen; Eds.), 2004.

66. K. R. Kribich, R. Copperwhite, H. Barry, B. Kolodziejczyk, J. M.. Sabattié, K. O'Dwyer, B. D. MacCraith "Novel Chemical Sensor/Biosensor Platform based on Optical Multimode Interference (MMI) Couplers", Sensors and Actuators B: Chemical, Issn : 0925-4005 Vol. 107, Iss. 1, pp. 188-192, 2005

67. Coudray, P.; Chisham, J.; Malek-Tabrizi, A.; C.-Y, Li; Andrews, M. P.; Peyghambarian, N.; Najafi, S. I.," : Ultraviolet light imprinted sol-gel silica glass waveguide devices on silicon", Optics Communications, Vol 128, Issue 1-3, pp. 19-22, 1996

68. Coudray, P.; Etienne, Y.; Porque, J. P. ; Moreau,; Najafi, S. I., "Integrated optical devices achieved by sol-gel process", SPIE Journal, Vol. 3278, pp 252-258, 1998

69. H. Jiang, X.-C. Yuan, Z. Yun, Y. C. Chan, Y. L. Lam, "Fabrication of microlens in photosensitive hybrid solgel films using a gray scale mask," Materials Sci. Eng. C 16, 99–102 (2001).

70. M. Kawachi, "Recent progress in silica-based planar lightwave circuits on silicon," IEE Proc. Optoelectron, Vol. 143, No. 5, pp. 257-262, 1996

71. R. Houbertz, G. Domann, C. Cronauer, A. Schmitt, H. Martin, J.-U. Park, L. Fröhlich, R. Buestrich, M. Popall, U. Streppel, P. Dannberg, C. Wächter and A. Bräuer, "Inorganic-organic hybrid materials for application in optical devices," Thin Solid Films 422, 194-200 (2003)

72. Almeida, R.M., "Sol-gel silica films on silicon substrates"; International Journal of Optoelectronics; Vol. 9; Nr. 2; pp. 135-142, 1994

73. Karl-Heinz Haas Hybrid Inorganic-Organic Polymers Based on Organically Modified Si-Alkoxides, Advanced Engineering Materials, 2, No. 9, pp. 571-582, 2000

74. M.Kusevic, M. Hiltunen, "Development of Polymeric Materials for Waveguide Components", SPIE´s International Symposium Photonics West 2002, San Jose, USA.

75. Jean-Marc Sabattie, Brian D. MacCraith, Karen Mongey, Jerome Charmet, and Kieran O'Dwyer, "Planar optical integrated circuits based on UV-patternable sol-gel technology", Proc. SPIE Vol. 4876,p. 295-303, Opto-Ireland 2002: Optics and Photonics Technologies and Applications; Thomas J. Glynn; Ed.

76. G. Taguchi, Rheological study of the sol-gel transition in silica alkoxides. J Colloid Interface Sci 249:209–216, 1991

77. M. Oubaha, R.K. Kribich, R. Copperwhite, K. O'Dwyer, P. Etienne, B. D. MacCraith and.Y. Moreau, "New organic-inorganic sol-gel material with high transparency at 1.55 µm", *Optics communications*, In Press (2005).

78. M. Oubaha, R. Copperwhite, B. Murphy, B. Kolodziejczyk, H. Barry, K. O'Dwyer and B.D. MacCraith, "Development of novel photo-patternable organo-mineral hybrid films from the sol-gel condensation of alkoxysilanes", Thin Solid Films, to be published

79. Etienne, P.; Coudray, P.; Moreau, Y.; Porque, J., "Photocurable sol-gel coatings: Channel waveguides for use at 1.55 mu|, Journal of Sol-Gel Science and Technology, Vol. 13, Issue 1-3, pp. 523-527, 1998

80. Coudray, P.; Chisham, J.; Andrews, M. P.; Najafi, S. I., "Ultraviolet light imprinted sol-gel silica glass low-loss waveguides for use at 1.55 mu m", Optical Engineering, Vol. 36, Issue 4, pp. 1234-1240, 1997

81. Porque, J.; Coudray, P.; Moreau, Y.; Etienne, P., "Propagation in sol-gel channel waveguides: numerical and experimental approaches", Optical Engineering, Vol. 37, Issue 4, pp. 1105-1110, 1998

82. M. Amir Fardad et al., "Solvent-assisted lithographic process using photosensitive sol-gel derived glass for depositing ridge waveguides on silicon", US Patent, No. 6,054,253, Apr. 2000

83. Xin M. Du, Tahar Touam, L.Degachi, J.L. Guilbault, Mark P. Andrews, S. Iraj Najafi, "Sol-gel waveguide fabrication parameters: an experimental investigation", Opt. Eng., 37(4), pp. 1101-1104, 1998

84. O-H Park, JI Jung, and B-S Bae, "Photoinduced condensation of sol-gel hybrid glass films doped with benzildimethylketal," J. Mater. Res. 16, 2143-2148, 2001

85 X Zhang, H Lu, A M Soutar and X Zeng, "Thick UV-patternable hybrid sol-gel films prepared by spin coating", *Journal of Materials Chemistry*, Vol 14, pp 357-361, 2003

86 M A Fardad, et al , "Fabrication of ridge waveguides A new sol-gel route," J Appl Opt, 37, No 12, pp 2429-2434, 1998

87 Horowitz F , Michels A , Yeatman E M "Optical viscometry of spinning sol coatings" J Sol-Gel Sci Tech 13, pp 707-712, 1998

88 Alissa M Fitzgerald, "Contact mask design principles", presented at Stanford Nanofabrication Facility Open House, 21 April 2004

89 P Coudray, P Etienne, Y Moreau, J Porque, S I najafi Sol-gel channel waveguide on silicon fast direct imprinting and low cost fabrication" Optics Communications 143 (1997) pp 199-202

90 Fiona H Scholes, Scott A Furman, Deborah Lau, Chris J Rossouw, Tim J Davis, "Fabrication of photo-patterned microstructures in an organic-inorganic hybrid material incorporating silver nanoparticles" Journal of Non-Crystalline Solids, 347, pp 93-99, 2004

91 S M Sze, VLSI Technology, McGraw-Hill, ISBN 0-07-062686-3, 1983

92 Larry F Thompson, Murrae J Bowden, C Grant Wilson, Introduction to Microlithography, American Chemical Society, Washington, 1983

93 Michael A Lieberman, Allan J Lichtenberg, "Principles of Plasma Discharges and Materials Processing", John Wiley & Sons, 1994

94 GS Oehrlein and JF Rembetski, "Plasma-based dry etching techniques in silicon integrated circuit technology", IBM J Res Devel 36, 140, 1992

95 Bauerfeldt Glauco F , Arbilla Graciela, "Kinetic analysis of the chemical processes in the decomposition of gaseous dielectrics by a non-

equilibrium plasma - part 1: CF4 and CF4/O2", Journal of the Brazilian Chemical Society, Vol 11 Issue 2, pp. 121-128, 2000

96. Daniel L. Flamm, "Mechanisms of silicon etching in fluorine- and chlorine-containing Plasmas", Pure & Appl. Chem., 62(9), 1709, 1990

97. Kirt R. Williams and Richard S. Muller, "Etch Rates for Micromachining Processing," Journal of Microelectromechanical Systems, vol. 5, no. 4, pp. 256-269, 1996

98. Kirt R. Williams, Kishan Gupta, and Matthew Wasilik, "Etch Rates for Micromachining Processing—Part II," Journal of Microelectromechanical Systems, vol. 12, no. 6, pp. 761-778, 2003

99. R. d'Agostino, "Plasma etching of Si and SiO_2 in $SF_6 - O_2$ mixtures", J. Appl. Phys. 52(10), January 1981

100. H. G. Lergon, M. Venugopalan, and K. G. Müller, "Mass Spectrometer – Wall Probe Diagnostic of Ar Discharges Cotaining SF_6 and/or O_2: Reactive Ions Etching Plasmas", Plasma Chemistry and Plasma Processing, Vol. 4, No. 2, 1984

101. A Picard et al. Plasma diagnostics of a SF6 radiofrequency discharge used for the etching of silicon, J. Phys. D: Appl. Phys., 19, pp. 991-1005, 1986

102. A. A. Ayón, R. L. Bayt and K. S. Breuer, "Deep reactive ion etching: a promising technology for micro- and nanosatellites", Smart Mater. Struct., 10 (2001), pp. 1135-1144

103. S. Tanaka, K. Rajanna, T. Abe, M. Esashi, "Deep reactive ion etching of silicon carbide", Journal of Vacuum Science & Technology B: Microelectronics and Nanometer Structures 19(6):2173 –2176, 2001.

104. R. He and C.-J. Kim ""Post-Deposition Porous Etching of Polysilicon: Fabrication and Characterization of Free-Standing Structures", Proc. ASME Int. Mechanical Engineering Congress and Exposition, Anaheim, CA, CD Vol. 2, IMECE2004-62198, Nov. 2004

105 E Kukharenka, M Kraft, "Realisation of electroplating moulds with thick positive SPR220-7 photoresist", Journal of Materials science Materials in Electronics, 14, pp 319-322, 2003

106 R d'Agostino, "Plasma Deposition, Treatment, and Etching of Polymers", Academic Press, Inc , 1990

107 A Sankaran and M J Kushner " Etching of Porous and Solid SiO2 in Ar/c-C4F8, O2/c-C4F8 and Ar/O2/c-C4F8 Plasmas ", J Appl Phys 97, 023307 (2005)

108 X Li, L Ling, X F Hua, M Fukasawa, G S Oehrlein, M Brela, H M Anderson, "Effects of Ar and O2 additives on SiO2 etching in C4F8-based plasmas", J Vac Sci Technol A 21 (2003) 284

109 J Wilson, J F B Hawkes "Optoelectronics, an introduction", Prentice Hall international series in optoelectronics, 2nd edition, ISBN 0-13-638461-7, 1988

110 E G Neumann, "Single-Mode Fibers Fundamentals", Springer-Verlag series in optical sciences, ISBN 3-540-18745-6, 1988

111 S Motakef, J M Boulton and D R Uhlmann "Organic-Inorganic Optical Materials" Optics Letters 19, pp 1125-1127, 1994

112 Q Zhou, P Kallio, F Arai, T Fukuda and H N Koivo, "A Model for Operating Spherical Micro Objects" Proceedings of the 1999 International Symposium on Micromechatronics and Human Science, MHS'99, pp 79 - 85, November 24-26, 1999

113 Chang, B , Zhou, Q , Koivo, H N , "Experimental Study of Microforces in a Controlled Environment", Proceedings of 2nd VDE World Microtechnologies Congress, MICRO tec 2003, Munich, Germany, pp 89-94, October 13-15, 2003

114 J Bergendahl, D Grasso, "Predıctıon of Colloıd Detachment ın a Model Porous Medıa Thermodynamıcs," Amerıcan Instıtute of Chemıcal Engıneers Journal, 45, 475-484, 1999

115 J Vısser, " Adhesıon of Colloıdal Partıcles" ın Surface and Colloıd Scıence, vol 8, edıted by E Matıȷevı, Wıley-Interscıence, New York, pp 3-84, 1976

116 J Vısser, "On Hamaker Constants -- a Comparıson between Hamaker Constants and Lıfschıtz-van der Waals Constants", Advan Colloıd Interface Scı, 3, 331-363 (1972) -- a thorough dıscussıon of varıous routes to obtaınıng Hamaker constants

117 B Gady, D Schleef, R Reıfenberger, D Rımaı, and L P DeMeȷo, "Identıfıcatıon of electrostatıc and van der Waals ınteractıon forces between a mıcrometer-sıze sphere and a flat substrate", Physıcal Revıew B-Condensed Matter, vol 53, no 12, pp 8065-70, 1996

118 D D Ward, "Electrostatıc dıscharge", IEE Semınar on EMC Desıgn, pp 4/1-4/8, 1999

119 Varun Saxena, "Polystyrene Mıcropartıcles as Handles for Optıcal Manıpulatıon of CATH a Cells", SURJ, 2, 2003

120 "Self-Assembly of Coated Colloıdal Partıcles for Optıcal Applıcatıons", LLE Revıew, Volume 97, 2003

13. Appendix

The appendix section includes details of LTM fabrication process as presented in Tables 13-1 to 13-4

Buffer and Protective Layers		
Material type		
Name	BL Standard	
ZrO_2 Content	2	%
Photoinitiator type and content (Irgacure 819)	1.8	%
Aging time	48	h
Wafer pretreatment		
Drying wafer to promote adhesion in (T=150°C)	30	min
Wafer cooling to ambient temperature (T=24°C)	1	min
Spincoating		
Filtration of sol-gel (filter pore size 0.2um)		
Stabilization of IPA environment in the spincoater	3	min
Dispension of 2.1 ml of sol-gel using pipette (center of the wafer)		
TIME1	7	s
ACCELERATION1	220	RPM/s
SPEED1	500	RPM
TIME2	35	s
ACCELERATION2	110	RPM/s
SPEED2	1200	RPM
Prebaking		
Hot plate (T=120°C)	15	min
Wafer cooling to ambient temperature (T=24°C)	1	min
UV exposure		
Mask alligner type	Carl Suss MA56	
Wavelength Spectra (I-line)	365	nm
Optical power	10	mW/cm2
Contact mode separation	92/08	
Time	210	s
Postbaking		
Hot Plate (T=120°C)	2	h

Table 13-1 Buffer and protective layers deposition process parameters

Waveguiding Layer		
Material type		
Name	GL Standard	
ZrO_2 Content	4	%
Photoinitiator type and content (Irgacure 819)	1.8	%
Aging time	48	h
Wafer pretreatment		
Drying wafer to promote adhesion in (T=150°C)	30	min
Wafer cooling to ambient temperature (T=24°C)	1	min
Spincoating		
Filtration of sol-gel (filter pore size 0.2um)		
Stabilization of IPA environment in the spincoater	3	min
Dispension of 2.1 ml of sol-gel using pipette (center of the wafer)		
TIME1	7	s
ACCELERATION1	220	RPM/s
SPEED1	500	RPM
TIME2	35	s
ACCELERATION2	110	RPM/s
SPEED2	1300	RPM
Prebaking		
Hot plate (T=120°C)	15	min
Wafer cooling to ambient temperature (T=24°C)	1	min
UV exposure		
Mask alligner type	Carl Suss MA56	
Wavelength Spectra (I-line)	365	nm
Optical power	10	mW/cm2
Contact mode separation	92/08	
Time	210	s
Developing		
Rinse with IPA (spincoater at 500 RPM)	~3	min
Rinse with DI water in the final stage		
Postbaking		
Hot Plate (T=120°C)	2	h

Table 13-2 Waveguiding layer deposition process parameters

Photoresist Layer		
Material type		
Name	SPR220-7	
Wafer pretreatment		
Drying wafer to promote adhesion in (T=150°C)	30	min
Wafer cooling to ambient temperature (T=24°C)	1	min
Spincoating		
No IPA environment		
Dispension of 4.5 ml of the material using pipette (center of the wafer)		
TIME1	120	s
ACCELERATION1	110	RPM/s
SPEED1	350	RPM
TIME2	25	s
ACCELERATION2	110	RPM/s
SPEED2	1000	RPM
Prebaking		
Hot plate (T=90°C)	100	s
Hot plate (T=115°C)	100	s
Exposure delay	24	h
UV exposure		
Mask alligner type	Carl Suss MA56	
Wavelength Spectra (I-line)	365	nm
Optical power	10	mW/cm2
Contact mode separation	92/08	
Time	90	s
Developing		
Rinse with MF-26A (spincoater at 500 RPM)	~4	min
Rinse with DI water in the final stage		
Postbaking		
Oven (T=90°C)	30	min

Table 13-3 Photoresist layer deposition process parameters

Reactive Ion Etching Process		
Plasma etcher type	Oxford Instr. RIE 80Plus	
Sample preparation		
Application of the buffering paste to the botom of the wafer		
RIE Plasma Conditions		
SF_6 flow	80	sccm
O_2 flow	0	sccm

Table 13-4 Reactive Ion Etching process parameters